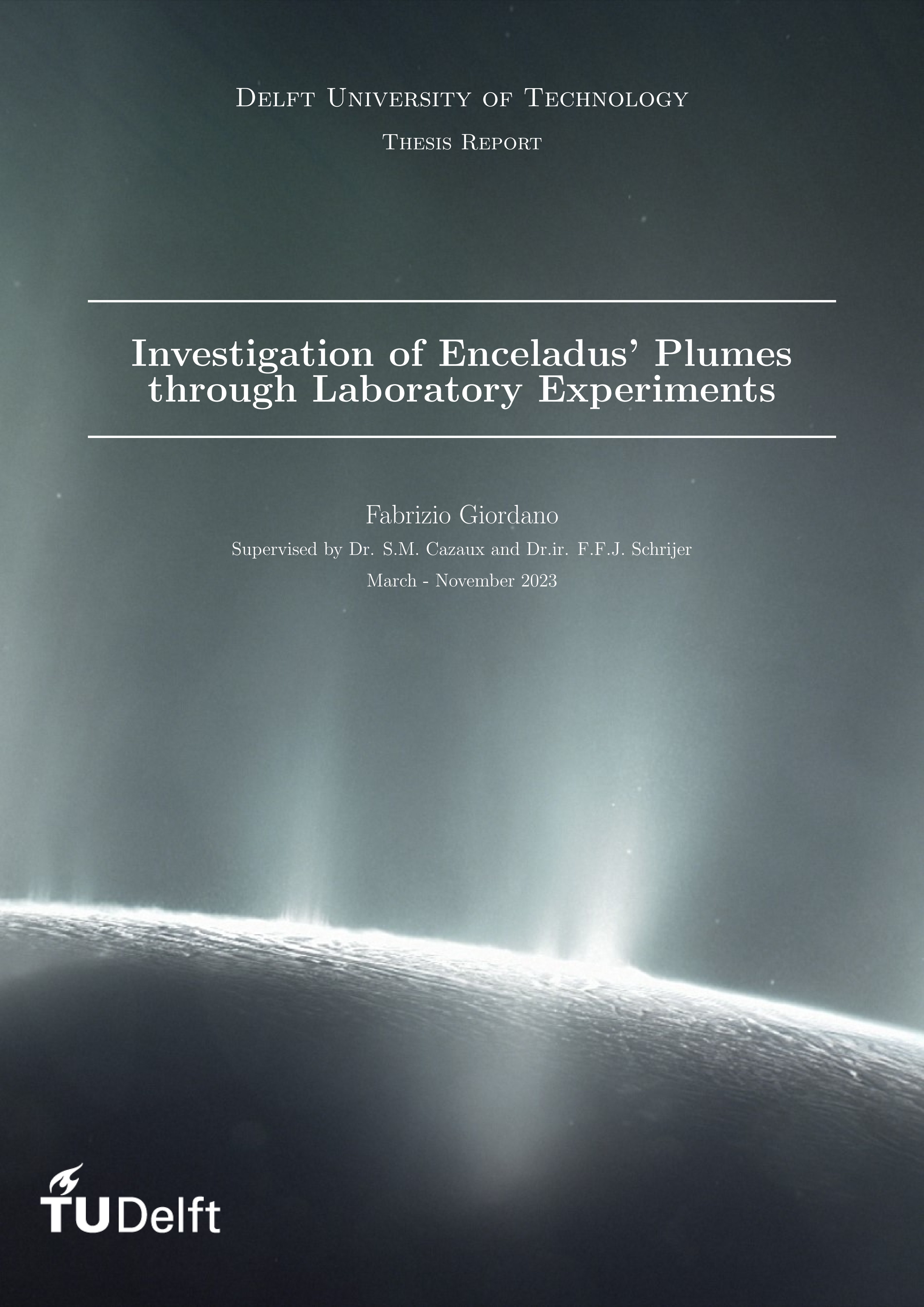

Delft University of Technology

Thesis Report

Investigation of Enceladus' Plumes through Laboratory Experiments

Fabrizio Giordano

Supervised by Dr. S.M. Cazaux and Dr.ir. F.F.J. Schrijer

March - November 2023

Thesis Report

Investigation of Enceladus' Plumes through Laboratory Experiments

by

Fabrizio Giordano

to obtain the degree of Master of Science
at Delft University of Technology

Student Number	5612055
Institution	Delft University of Technology
Supervisors	Dr. S.M. Cazaux & Dr.ir. F.F.J. Schrijer
Project Duration	1 March 2023 - 10 November 2023

Cover Image: NASA

Preface

As I conclude my thesis project, and along with it my MSc degree, I would like to express my sincere gratitude to my dedicated supervisors, Stéphanie Cazaux and Ferry Schrijer, for their support and invaluable guidance over the past year. I would also like to thank Stavros, who originally started this project on plume experiments, designed the experimental setup I utilized and provided valuable feedback throughout my project. A thank also to Thom, for his assistance with laboratory instrumentation during the initial stages of my project, to Freek, for helping me finding a freezer and moving it next to the vacuum chamber, and to Marnix, for the 3D print of the Pitot tube support. Furthermore, I extend my sincere thanks to Yaël, whose availability and insightful discussions greatly contributed to the interpretation of my results.

During my thesis project, I had the pleasure of spending a lot of time with my friends from study room 2.44. I will always remember the moments we shared during lunch breaks or in front of a cup of tea, helping each other and joking to relieve the stress. Among them, a thank goes to Jan for providing me with the 3D printed models.

I wish to extend my gratitude to my parents, who placed their trust in me and supported my decision to study at TU Delft, despite the challenges of living apart. Finally, a special thank goes to my girlfriend for her incredible support during the last 2 years, her enduring love despite the distance between us, and her boundless joy that brightens my days immeasurably.

Fabrizio Giordano
Delft, 26 October 2023

Contents

List of Figures

List of Tables

Nomenclature

Abbreviations

CIRS	Composite Infrared Spectrometer
HTFD	Hypersonic Tunnel Facility Delft
INMS	Ion and Neutral Mass Spectrometer
ISS	Imaging Science Subsystem
PIV	Particle Image Velocimetry
PLA	Polylactic acid
PP	Polypropylene
STP	South Polar Terrain
TC	Thermocouple
UVIS	Ultraviolet Imaging Spectrograph
VIMS	Visible and Infrared Mapping Spectrometer

Constants

σ	Stefan-Boltzmann coefficient
k_B	Boltzmann constant
$\mathcal{M}$	Molar mass
R	Universal gas constant
R_{sp}	Specific gas constant ($R/\mathcal{M}$)

Symbols

γ	Specific heat ratio
Δh	Specific enthalpy difference
ε	Emissivity
μ	Dynamic viscosity
ρ	Mass density per unit volume
σ	Standard deviation
A	Surface area
$\mathcal{A}$	Antoine equation coefficient
$\mathcal{B}$	Antoine equation coefficient
$\mathcal{C}$	Antoine equation coefficient
c_s	Sound speed
c_p	Specific heat (constant pressure)
c_v	Specific heat (constant volume)
d	Diameter
f	Solid fraction
h	Specific enthalpy
h_{conv}	Convective heat coefficient
I/V	Ice-vapour ratio
k	Thermal conductivity
L	Length
L_v	Latent heat of vaporisation
M	Mach number
$\dot{m}$	Mass flow rate
n	Column density
N^*	Effective sample size
Nu	Nusselt number
p	Pressure
p_0	Total pressure
p_{eq}	Equilibrium pressure
$p_{s.v.}$	Saturated vapour pressure
$\mathcal{P}$	Power
Pr	Prandtl number
$\dot{Q}$	Heat transfer rate (Power)
Re	Reynolds number
S	Supersaturation
T	Temperature
T_0	Total temperature
V	Velocity

1
Introduction

The Cassini spacecraft transformed our understanding of the habitability of the Solar System. Despite Saturn's distance from the Sun, Cassini's observations unveiled an unexpectedly active Enceladus (Porco et al., 2006; Spencer et al., 2006). This small moon, influenced by tidal forces, maintains a surprisingly warm interior, creating a liquid ocean beneath its icy shell (Roberts et al., 2008; Spencer et al., 2009; Choblet et al., 2017). Water vaporizes from this ocean and travels through cracks in the ice, erupting onto the moon's surface in powerful jets known as *plumes* (Porco et al., 2006; Ingersoll et al., 2011; Nakajima et al., 2016a).

Cassini's instruments detected salts and complex organic molecules in the plumes (J. H. Waite et al., 2006; Postberg et al., 2009; Postberg et al., 2018; Khawaja et al., 2019), raising intriguing questions about the potential for extraterrestrial life within Enceladus. Furthermore, the plume velocities were found to reach supersonic speeds (Hansen et al., 2006; Tian et al., 2007; Hansen et al., 2008; Smith et al., 2010; Dong et al., 2011; Hansen et al., 2011; Yeoh et al., 2017; B. D. Teolis et al., 2017; Portyankina et al., 2022), suggesting the presence of fissures that act as de Laval nozzles (Schmidt et al., 2008; Yeoh et al., 2015). Nonetheless, existing models have predominantly employed straight, uniform cross-sectional channel geometries to account for the observed mass flow rates (Nakajima et al., 2016a).

With the conclusion of Cassini's "Grand Finale" in 2017, the recently launched JUpiter ICy moons Explorer (*JUICE*) mission, and the possibility of upcoming missions exploring the Saturnian system, there is a growing interest in gaining further insights into these icy worlds. Consequently, this research project adopts an experimental approach to study icy moon plumes, building upon the work of Sklavenitis (2022) and Verhoeff (2023). The primary goal of this thesis project is to enhance our understanding of the interactions between Enceladus' ocean, icy crust, and plumes.

The project establishes an experimental methodology for investigating icy moon plumes. The experimental setup incorporates a water reservoir simulating the subsurface ocean and a channel mimicking a crack in the icy crust. Various sensors have been employed to measure the temperature and pressure of the water vapour flow within the channel. The primary research question is:

What is the influence of phase change and heat exchanges with the channel walls on the velocity of the plumes?

More specific research questions that will be addressed in this context include:

1. *What is the impact of wall temperature on the flow temperature and velocity?*
2. *Is nucleation achieved in a straight channel?*
3. *Can supersonic velocities, similar to those observed by Cassini, be reached without the aid of a de Laval nozzle?*

Addressing these questions is essential for understanding the connections between channel wall temperature and plume properties, shedding light on the physical attributes of Enceladus' subsurface ocean and icy crust.

The thesis report is structured as follows. Chapter 2 provides a literature overview of the existing knowledge about the moon Enceladus, its unique attributes, geophysical properties, and the scientific revelations on the plumes provided by missions like Cassini. Chapter 3 introduces the fundamental physical processes and principles essential to understanding the experimental results in the context of studying the icy moons. Chapter 4 includes the journal article, presenting the main experimental results and a comprehensive discussion on the implication of these outcomes on the characteristics of Enceladus' plumes. The conclusions are stated in Chapter 5, where the research questions are addressed. The final chapter is followed by appendices containing supplementary information and methods used during the research and a bibliography of cited sources.

2

The Plumes of Enceladus

Enceladus, the sixth-largest moon of Saturn, has caught the interest of the scientific community for its unique features. It is an icy moon with an icy surface composed of almost pure water (Porco et al., 2006) and is the body with the highest albedo in the solar system (Verbiscer et al., 2007). The heterogeneous crater density on its surface suggests formation ages from a few hundred of thousands of years to 4 *Gyrs* ago (Porco et al., 2006). A series of ridges and valleys have been observed in the south polar region (Figure 2.1), indicating an active geology. Cryovolcanic activity has been observed over this region: material from the moon's interior is ejected through jets, called *plumes* (Porco et al., 2006). These are mainly composed of water vapour and icy particles. However, small amounts of other gases and a 0.5-2% salinity inside some ice grains have been detected, indicating their potential origin in an ocean beneath the moon's surface (J. H. Waite et al., 2006; Postberg et al., 2011).

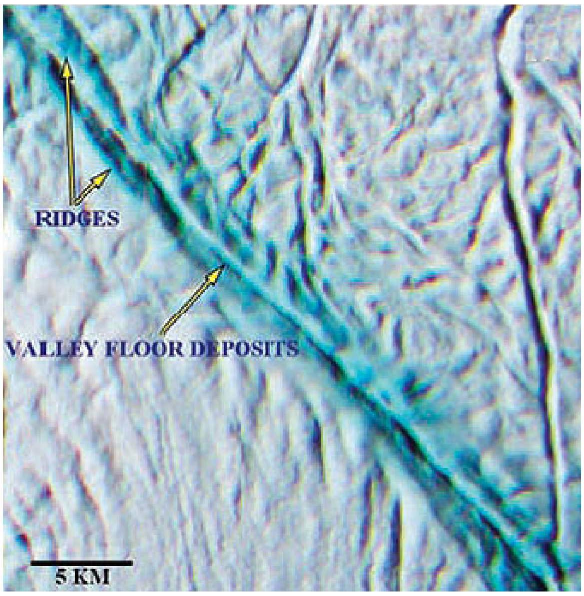

Figure 2.1: ISS false-colour image showing one of the tiger stripes located on the south polar region of Enceladus. The valley and the 2 ridges confining are darker, indicating coarse-grained ice. Resolution: 70 m/pixel (Porco et al., 2006).

This chapter focuses on Enceladus' plume activity. In Section 2.1, we present key findings from the Cassini-Huygens mission, emphasizing velocity, emission rates, and solid fraction as essential parameters for our research goal. Section 2.2 explores theoretical models explaining Enceladus' cryovolcanic activity and related thermodynamics, especially in the moon's surface crevasses where plumes are thought to originate. Lastly, Section 2.3 covers experimental setups used in other studies to investigate plume activity.

2.1 Plume Observations with the Cassini Spacecraft

The Cassini spacecraft arrived in the proximity of the Saturnian system in July 2004 and operated for more than 13 years, until September 2017, flying by 22 times around Enceladus (Krupp et al., 2018) and collecting a wealth of observations. Cryovolcanic activity has been observed over the South Polar Terrain (*SPT*) both directly and indirectly.

In-situ density measurements, observed with the Ion and Neutral Mass Spectrometer (*INMS*), and images of plumes in the visible radiation (see Figure 2.2), captured with the Imaging Science Subsystem (*ISS*), indicate that water vapour jets are likely outgassing from the cracks on the *SPT* (J. H. Waite et al., 2006), especially from 4 parallel fissures informally named *Tiger Stripes*.

Composite Infrared Spectrometer (*CIRS*) observations further support the hypothesis of jet sources localized over the *SPT*. Figure 2.3 shows an example of anomalously large surface brightness temperature in correspondence of the *Tiger Stripes*. Surface temperatures above 145±14 K have been estimated by Spencer et al. (2006) and up to 180-210 K by Spencer et al. (2013) and Tenishev et al. (2014), suggesting the presence of geological and cryovolcanic activity. Using these *CIRS* observations, a total power output around 5.8±1.9 *GW* has been estimated by (Spencer et al., 2006), later updated to 15.8±3.1 *GW* by (Howett et al., 2011). According to Choblet et al. (2017), only liquid water pumped through a porous core by tidal forces could explain these high values of heat flux, further supporting the theory of Enceladus as a differentiated body, with a subsurface ocean a few kilometres deep from which plume material originates (Spencer et al., 2009; Beuthe et al., 2016).

Visible and Infrared Mapping Spectrometer (*VIMS*) observations, shown in Figure 2.4, highlight regions covered by crystalline ice in correspondence of the *tiger stripes* and plains between these 4 cracks dominated by amorphous ice (Robidel et al., 2020). As explained by (Newman et al., 2008), crystalline ice has a regular molecular structure and is formed at temperatures above 130 K. Amorphous ice, instead, does not have an organized molecular structure and is formed at lower temperatures through a process called *flash-freezing*. An increase in temperature turns amorphous ice into crystalline ice, while crystalline ice can turn into amorphous ice at low temperatures (below 70-80 K) when exposed to UV radiation or bombarded by high-energy particles. The difference in ice type observed over the SPT could be caused by the cryovolcanic activity: high surface temperatures, closer to the tiger stripes, would allow the formation and deposition of crystalline, while flash freezing of water vapour at higher altitudes could form amorphous ice, which deposits onto the plains between the tiger stripes (Newman et al., 2008; Robidel et al., 2020).

Ultraviolet Imaging Spectrograph (*UVIS*) observations during stellar occultations have been widely used to infer several plume characteristics. The ultraviolet radiation emitted by a star and crossing the plumes is captured and the intensity of the spectrum is compared with the spectrum outside occultation. The gas in the plumes can absorb some of this radiation. From the absorption features in the spectrum, the composition of the plumes has been inferred (J. H. Waite et al., 2006), resulting

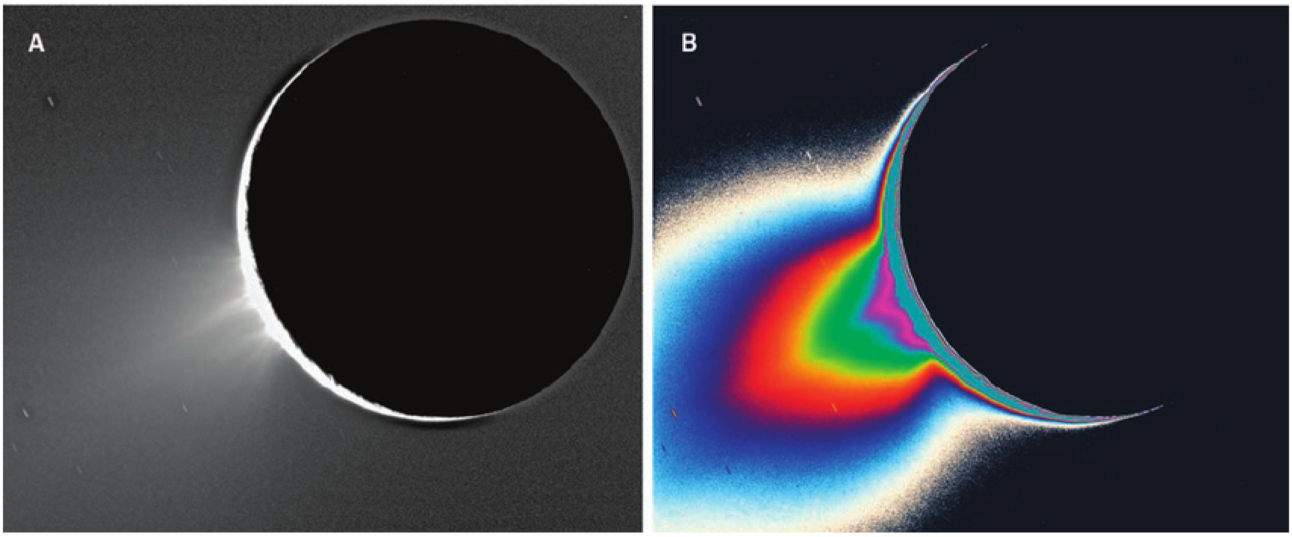

Figure 2.2: *ISS* image of Enceladus near surface plumes, taken with a phase angle of 161.4°. The south pole points towards the lower left corner of the picture. The colour-coded version on the right shows the large extent of plume material above the *SPT*. The radiation is forward-scattered by fine icy particles restrained in the vapour jets (Porco et al., 2006).

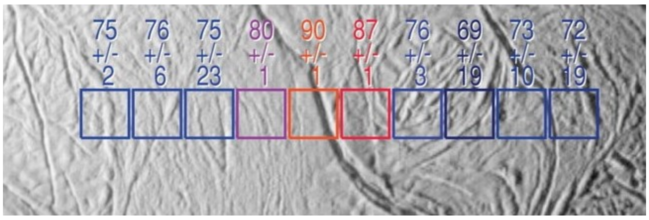

Figure 2.3: Example of Cassini *CIRS* data plotted over the moon topography derived from simultaneous *ISS* images. Above each box is indicated the average brightness temperature (with uncertainty) over that location. The field of view size is 6.0 *km* (Spencer et al., 2006).

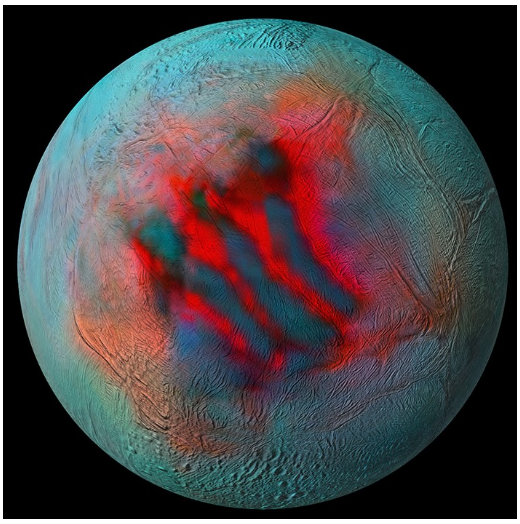

Figure 2.4: Infrared mosaic of the south hemisphere of Enceladus, created using multiple images from the Cassini Visible and Infrared Mapping Spectrometer (*VIMS*). Red areas in correspondence of the tiger stripes indicate high ice crystallinity, while the dark blue plains between them are dominated by amorphous ice, as found by (Robidel et al., 2020). Image credit: *NASA/JPL-Caltech/University of Arizona/LPG/CNRS/University of Nantes/Space Science Institute*.

in a large water vapour component with traces of other species such as CO_2, CH_4, and N_2. From the intensity difference between the occulted and non-occulted spectrum, (Hansen et al., 2006) was able to infer the column density and emission rate of some jets, above 150 kg/s. The plume velocity was assumed equal to the thermal velocity at the surface, which for a temperature of 180 K is approximately 450 m/s, computed with Equation 2.1. Hansen et al. (2008) and Hansen et al. (2011) found higher velocities by observing the angular distribution of the plume gas, assuming that the particles spread laterally with thermal velocity. The inferred Mach number ranged between 1.5 and 8, corresponding to 675-3600 m/s for a thermal velocity of 450 m/s, and emission rates around 180-250 kg/s (Hansen et al., 2017; Hansen et al., 2020). Tian et al. (2007), Smith et al. (2010), Yeoh et al. (2017) and Portyankina et al. (2022) used Monte Carlo simulations, fitting *UVIS* and *INMS* density observations, and estimated venting velocities between 300 m/s and 1,800 m/s and emission rates up to 1000 kg/s. Other authors used analytical models to estimate the same parameters and obtained similar results (Dong et al., 2011; Tenishev et al., 2014; B. D. Teolis et al., 2017; Fu et al., 2021).

$$v_{th} = \sqrt{\frac{8k_BT}{m\pi}} \tag{2.1}$$

Solid fraction is the fraction of icy particles over the total mass ejected by the plumes. Kieffer et al. (2006) combined *ISS* and *UVIS* observations to estimate the icy particles and gas density respectively, finding an ice-vapour ratio (I/V) around 0.2. Ingersoll et al. (2011) investigated other *ISS* datasets with the use of scattering models simulating different particle distributions and sizes, obtaining an I/V between 0.35 and 0.7. However, Gao et al. (2016) found that the ratio would drop to 0.07±0.01 if the icy grains were not spherical particles but irregular aggregates.

2.2 Theoretical Plume Models

The most accredited theory attributes the source of plumes to vaporized water from a subsurface boiling ocean, rather than sublimation. Porco et al. (2006) formulated what we now call the "Cold Faithful" theory: tidal stresses open the cracks in the surface and the subsurface ocean, exposed to the low pressure of outer space, reaches triple point. The resulting violent boiling of water expels vapour and frozen water droplets through the crevasses, ultimately venting them at the moon's surface. In the following sections, we present some theories explaining the long-term sustainability of this system and models describing the flow characteristics within the walls of the crevasses.

2.2.1 Long-Term Sustainability of the Plume System

Enceladus has been continuously erupting throughout the Cassini mission and we have evidence that this activity has been sustained for a much longer period (Postberg et al., 2009; Hansen et al., 2011;

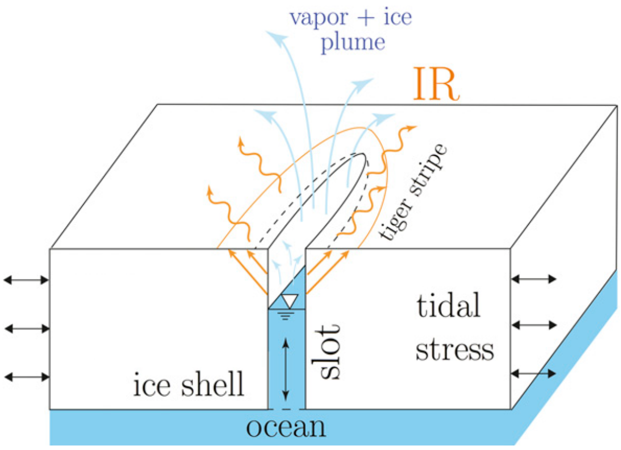

Figure 2.5: Schematic of the "Turbulent Dissipation" model of one tiger stripe fracture over the SPT of Enceladus. The water level in the crevasse (blue) rises when tidal stress (double-headed arrows) compresses the ice crust and decreases when the crack is re-opened. Water vapour in the plume (light blue arrows) is ejected into space or accreted onto the crack walls by condensation, releasing heat to the ice crust. The heat is transported to the surface by conduction and radiated as infrared (IR) radiation (orange arrows). Image retrieved from Kite et al. (2016).

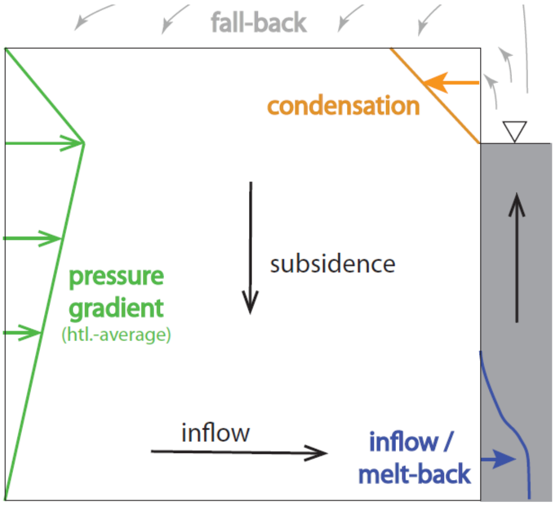

Figure 2.6: Illustration of the tectonics in the ice shell of Enceladus near the tiger stripes. Grey area: ocean water filling the crevasse. White area: ice shell. The pressure gradient inside the ice shell (green) causes an inflow of ice (blue) at the bottom of the ice layer, where temperatures are higher and ice is softer. The channel area becomes smaller and turbulent dissipation increases, causing melt-back of ice. Subsidence balances the ice melting with new, colder ice. Ice originating from wall condensation (orange) and fall-back of plume material (light grey) replenishes the ice crust.Image retrieved from Kite et al. (2016).

Dong et al., 2011; Porco et al., 2014; Spitale et al., 2015). Nevertheless, several elements would lead us to think the opposite. First, the evaporation of water from the subsurface ocean removes heat from the subsurface ocean itself, causing water to freeze. Moreover, water vapour can condense onto the walls of the crevasses, solidifying and potentially clogging the fissures in a very short period. To explain this long-term activity, Kite et al. (2016) proposed the "Turbulent Dissipation" model. Fissures are modelled as parallel rectangular slots, subject to tidal forces that open and close them, as sketched in Figure 2.5. Figure 2.6 shows a schematic of the tectonic in the ice shell close to the crevasses. The processes involved are the following:

a. *Inflow/Necking* - At the base of the ice crust temperatures are higher and ice is softer. Therefore, pressure forces in the ice shell cause inflow of ice, reducing the area of the channel;

b. *Melt-back* - Tidal stress opens or closes the fissures, allowing water to flush back into the ocean in the former case, or refill them in the latter. This process generates turbulence in the water and causes the mixing of water. Cooled water sinks and is replaced by warmer water from below, which melts ice and prevents necking.

c. *Subsidence* - The mass of ice at the base of the ice crust is restored by colder ice, sinking from higher layers in the crust. This ice originates from fall-back material and condensation onto the walls.

The combination of these processes prevents clogging of the fractures and explains the high surface temperatures on the *SPT*: evaporation removes heat from the ocean, which is returned to the ice crust by condensation, conveyed to the moon's surface through conduction and radiated away, as illustrated in Figure 2.5.

2.2.2 Crevasse Geometry

According to the results of numerical simulations performed by Kite et al. (2016), the plumes are sustained only if their stress-free half-width is around 1 ± 0.5 m. Smaller and larger widths would not allow enough heat transfer and turbulent dissipation to contrast wall accretion. Cracks smaller than 0.5 m would close and cracks larger than 2.5 m would narrow. Nakajima et al. (2016a) found a similar value of crack width to prevent the liquid water interface from freezing. In a following publication, Ingersoll et al. (2016b) added that there is no need for a large vapour chamber as a plume source to avoid water freezing. Moreover, larger widths are allowed for higher water salinity.

To obtain the observed emission rates, a crack with a uniform width of 0.05-0.075 m is required, according to Nakajima et al. (2016a). A tapering crack larger than 1 m at the bottom and 0.05-0.075 m wide at the vent or a tortuous crack with an average width of 1 m would be possible alternative configurations. These would prevent high values of emission rate by increasing the water vapour flux condensed onto the walls. In the computations, a crack depth of 1.7 km and ice shell thickness of 20 km were assumed.

To address the inconsistencies between the slow speeds of particles in the plumes, estimated around 60 m/s by Porco et al. (2006), and the extremely fast expulsion of vapour seen in section 2.1, Schmidt et al. (2008) developed another plume model, referred to as "Modern Plume Theory". According to this model, the velocity difference between the grains and vapour is attributed to the grains frequently colliding with the icy walls, causing their velocity to be reduced. Therefore, the model suggests that the cracks are tortuous to generate these collisions.

2.2.3 Thermodynamic Conditions of the Plume Flow in the Crevasses

Schmidt et al. (2008) suggested that the channels in the icy crust act like de Laval nozzles, resulting in supersonic acceleration of the gas flow. This process involves significant changes in temperature and pressure, leading to the rapid condensation of vapour into icy particles. The same author highlights the role of collisions of ice particles with the crevasse walls to explain the different velocities between gas and solid phases in the plumes.

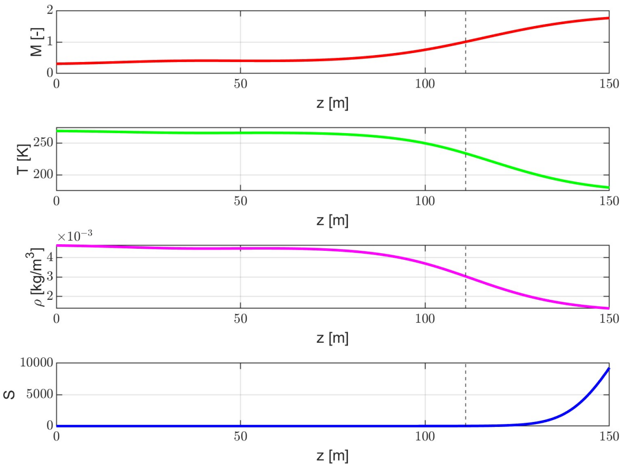

Figure 2.7: Solutions of the isentropic model, assuming a perfect gas flowing in a de Laval nozzle with vent-to-throat area ratio $A_{exit}/A_{th} \simeq 1.42$. The length of the nozzle is indicated on the horizontal axis. The dashed grey line at ∼110 m indicates the throat location. From the top to the bottom: Mach number M; temperature T; density ρ; saturation degree S. Image retrieved from Hijden (submitted).

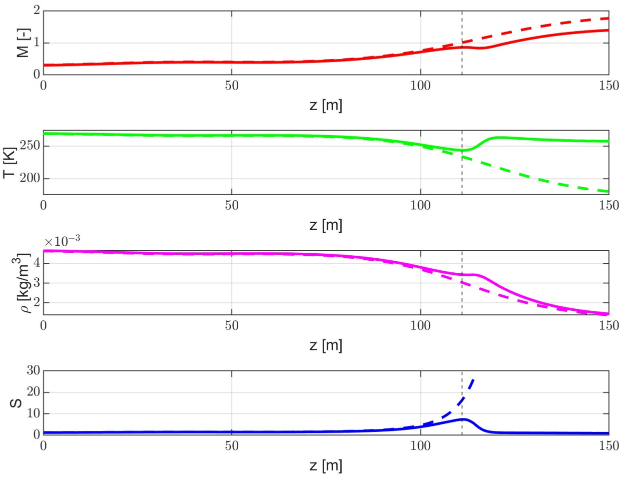

Figure 2.8: Solutions of the plume model with nucleation, grain growth, sublimation and accretion onto the crevasse walls, named as *Multi-Phase Model* (solid lines), compared to the isentropic model solutions (dashed lines). The same nozzle geometry as in Figure 2.7 has been used. Image retrieved from Hijden (submitted).

Assuming an isentropic flow of pure water vapour, Yeoh et al. (2015) constrained the geometry of the channel, resulting in a 0.46 m throat diameter and 1 m vent diameter to obtain a Mach number of 3. Hijden (submitted) computed the Mach number, temperature, and pressure profiles of this model, shown in Figure 2.7. The Mach number increases, reaching 1 at the throat, and 1.76 at the vent. Having assumed an isentropic flow, the expansion of the gas is adiabatic, leading to a decrease in density and temperature. At these vent temperature and pressure conditions, a phase change from gas to solid is highly likely. As mentioned before, water vapour can condense to form icy particles in the flow in a process called *nucleation*. Moreover, this model neglects to consider heat exchanges with the walls, viscous effects and turbulence (Yeoh et al., 2015).

Nucleation, grain growth, sublimation and accretion onto the crevasse walls have been accounted for in the model developed by Hijden (submitted). The results of this model are displayed in Figure 2.8. The author attributes the increase in pressure/density and temperature to nucleation and condensation, releasing heat to the flow. These processes are triggered by the increase in saturation degree (S) defined as the ratio between the pressure of the flow (p) over the saturated vapour pressure (p_{eq}), dependent on the flow temperature.

2.3 Plume Experiments

Previous studies used experiments to simulate the plume flow and assess the validity of theoretical models. In this section, we describe the laboratory configurations tested by various researchers and summarise the key findings yielded by their investigations.

2.3.1 Plexiglass Model

Sklavenitis (2022) simulated the liquid water reservoir lying under the ice crust of Enceladus with a liquid water reservoir. By placing the reservoir in a vacuum chamber, he was able to achieve the water triple point condition. As sketched in Figure 2.9, the water vapour was forced to flow through a de Laval nozzle made out of plexiglass, along which temperature and pressure were measured. Heating foils were used to prevent freezing of the water in the reservoir, cooled by the evaporation process.

Sklavenitis (2022) found a discrepancy between observed and theoretical mass flow rate, attributed to friction, condensation or other heat exchanges with the experimental setup, therefore concluding that the flow was not isentropic. Moreover, the *Particle Image Velocimetry* (PIV) technique has failed to detect icy particles in the flow, indicating a flow far from saturation conditions.

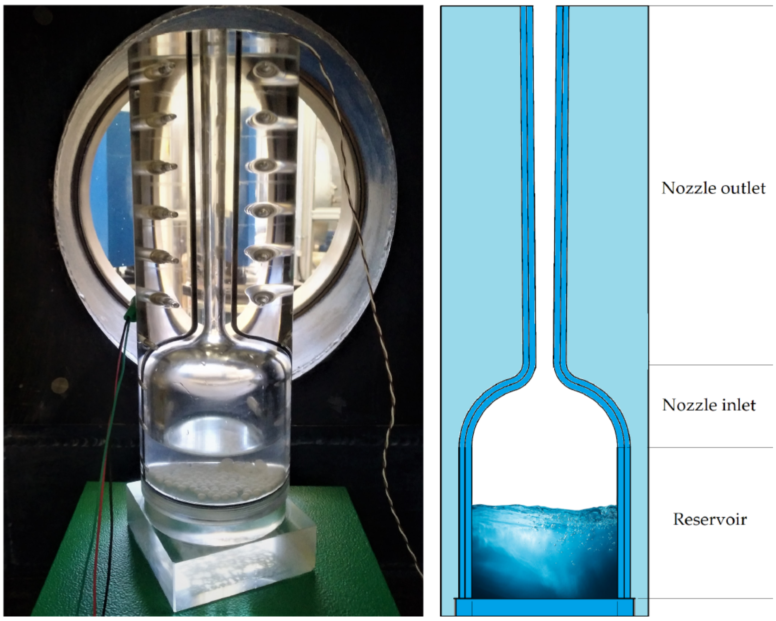

Figure 2.9: Plume model made out of plexiglass. On the left: photograph of the manufactured model, located inside the vacuum chamber of the Hypersonic Tunnel Facility Delft (HTFD). Pressure and temperature sensors are positioned along the nozzle. On the right: cross-section view of the model. The water in the reservoir vaporises, and the gas travels through the nozzle. Image retrieved from Sklavenitis (2022).

2.3.2 Ice Model

A laboratory setup made out of ice allowed us to better simulate the temperature conditions of the ice shell of Enceladus (Becx, 2019). However, the complexity of manufacturing the model and its quick melting at room temperature have irreparably hampered the experiments and the interpretation of acquired data.

2.3.3 Plastic Models

Several channel geometries have been tested by Verhoeff (2023). The models were 3D printed and made out of polylactic acid (PLA) or polypropylene (PP). The different vent-to-throat area ratios generated differences in pressure and temperatures along the nozzle according to the theory. The same author also investigated the influence of different pressure levels in the reservoir on the flow conditions. However, the temperature profiles, similar to the one found by Sklavenitis (2022), did not indicate a flow behaviour comparable to that inside the crevasses of Enceladus.

Several issues are still up for debate. What makes a laboratory model representative of the real-case plumes and how can we compare the two systems? What is the contribution of heat exchange between model and flow and how is the model temperature affecting the flow? How can we reliably assess the flow velocity? Is a convergent-divergent channel necessary to reach supersonic velocities at the vent?

3

Physical Principles of the Plume Experiments

This chapter serves as an introductory overview of the fundamental physical parameters, processes and principles that have played an important role in our plume experiments, as detailed in this report. In Section 3.1, we provide an overview of the phase change processes relevant to the plumes. In Section 3.2, we examine the heat transfer mechanisms considered in this study. Finally, section 3.3 offers an explanation of the fundamental theory essential for comprehending the flow expansion within a channel and determining its key attributes.

3.1 Water Phase Diagram

The theory of plumes as eruptions of water vapour and ice grains originating from a subsurface ocean is widely accepted and supported by observations of solid fraction (Porco et al., 2006; Ingersoll et al., 2011) and icy grain composition (Postberg et al., 2009). The surface layer of water in the ocean is likely at a temperature of 273 K due to its direct contact with the ice shell. The presence of cracks in the crust connects the ocean's surface to outer space, resulting in a decrease in pressure. As depicted in the water phase diagram in Figure 3.1, when the pressure drops below 612 Pa, liquid water undergoes boiling and evaporation, transforming into water vapour. This temperature and pressure condition where solid, liquid and gas phases coexist is referred to as *triple point*. The vapour and icy particles formed then follow the natural pressure gradient within the crevasse and are carried away towards outer space.

The following paragraphs summarize the characteristics of the phase transitions involved in the plume's mechanisms, making reference to the phase diagram in Figure 3.1.

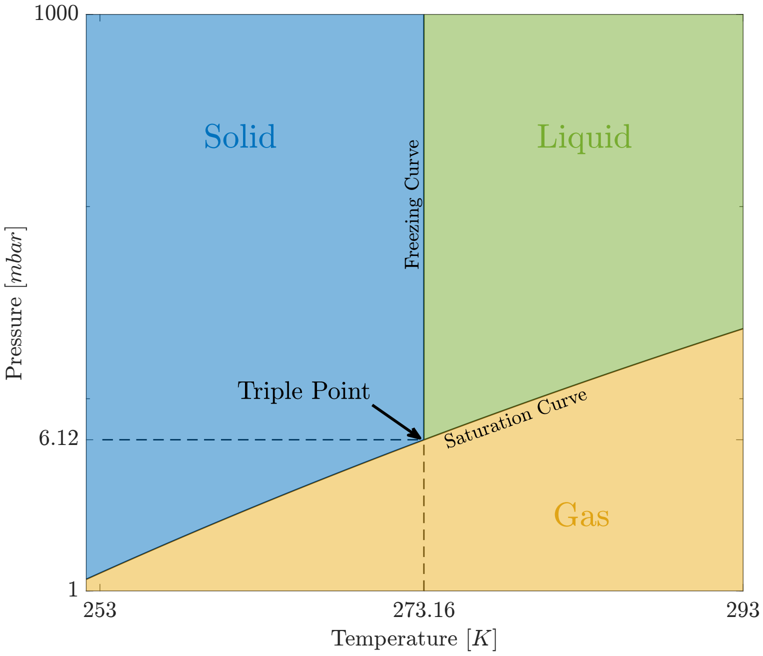

Figure 3.1: Phase diagram of water, with pressure in logarithmic scale on the vertical axis. The ocean table is assumed to be at the triple point condition, where the temperature is around 273.16 K, pressure at 612 Pa and the three phases - solid, liquid and gas - coexist. Freezing curve defines the transition between liquid and solid phase. The gas saturation curve indicates the pressure-temperatures conditions for which gas transitions to liquid phase (condensation) or solid phase (nucleation/deposition). Image created in *MATLAB*.

3.1.1 Vaporization

Vaporization is the change of phase from liquid to gas, occurring when the attractive intermolecular forces binding the liquid water molecules to each other are overcome. Breaking these bonds requires energy, often in the form of heat. Hence, vaporization is an endothermic process.

Vapor Pressure The vapour pressure p_v is the pressure exerted by the vapour molecules of a substance. If the gas is composed of only one substance, the total ambient pressure of the gas (p_{amb}) will be equal to the vapour pressure of that substance. Otherwise, the total pressure is equal to the sum of the partial pressures of each gas component.

Saturated Vapor Pressure The saturated vapor pressure $p_{s.v.}$ is the vapor pressure when the vapor is saturated. In these conditions, the flux of molecules evaporating is equal to the flux of molecules turning into the liquid state. Due to this equilibrium, $p_{s.v.}$ is also referred to as the equilibrium pressure (p_{eq}). Above this level of pressure, condensation dominates in the gas. Being a function of temperature, the saturated vapour pressure is the maximum vapour pressure achievable at a certain temperature. Its value corresponds to the boiling curve in the water phase diagram in Figure 3.1 and is calculated with the *Antoine equation*, reported in Equation 3.1. In this equation, T is the temperature, and A, B, and C are constants characteristic of the substance in question (Antoine, 1888).

$$\log p_{s.v.} = \mathcal{A} - \frac{\mathcal{B}}{\mathcal{C} + T} \tag{3.1}$$

Enthalpy of Vaporization The amount of heat that needs to be supplied to turn into gas one unit of mass of liquid water without changing its temperature (isothermally) at an external pressure equal to the saturated vapour pressure of the liquid is called *enthalpy of vaporization* (L_v), or *latent heat of vaporization*. This value depends on the liquid water temperature, as shown in Figure 3.2: the higher the temperature of the liquid, the higher the energy state of the system and, thus, the lower the energy needed to loosen the intermolecular bonds (Kikoin et al., 1978; Matveev, 1985).

Evaporation and Boiling Evaporation and boiling are two processes through which a liquid can vaporize. *Evaporation* is the vaporization of water particles at the surface of the liquid, which for the plumes corresponds to the water table inside the crevasses. This process occurs when the vapour pressure is lower than the saturated water pressure (Equation 3.2). On the other side, *boiling* is the vaporization of water particles inside the liquid. In order for boiling to occur, the ambient pressure must be lower than the saturated vapour pressure (Equation 3.3).

$$p_v < p_{s.v.} \tag{3.2}$$

$$p_{amb} < p_{s.v.} \tag{3.3}$$

As mentioned above, the ambient pressure p_{amb} is equal to the vapour pressure p_v if water is the only component of the gas phase. Otherwise, p_v is lower than p_{amb}. Therefore, evaporation can occur without boiling, since Equation 3.2 can be true without Equation 3.3. In this case, we would have the following pressures:

$$p_v < p_{s.v.} < p_{amb} \tag{3.4}$$

However, it is not possible to have boiling without evaporation (i.e. $p_{amb} < p_v = p_{s.v.}$), since Equation 3.3 is true only if also Equation 3.2 is true (Kikoin et al., 1978).

3.1.2 Sublimation

When Enceladus cryovolcanic activity was first discovered, one of the major theories for plume origin involved the sublimation of ice from the tiger stripes (Porco et al., 2006). At the surface of the moon, the pressure is expected to be in the order of few Pa, therefore, at sufficiently high ice temperatures

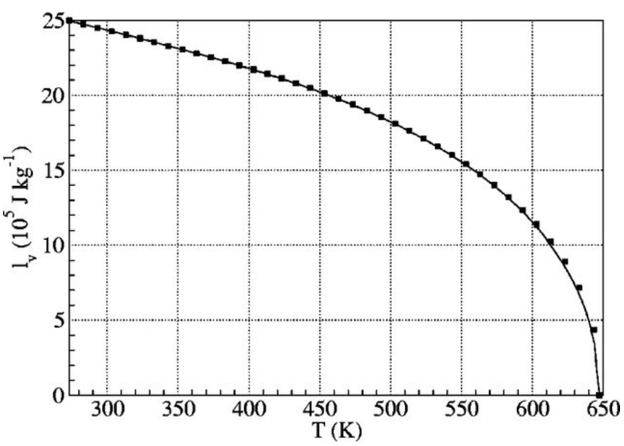

Figure 3.2: Latent heat of vaporization of water as a function of water temperature, indicating the amount of heat subtracted by the process for each kg of water evaporated. The temperature ranges between the triple point condition (273 K), and the critical point (650 K), where water can be in the liquid state (see Figure 3.1). Image retrieved from Pellicer et al. (2002).

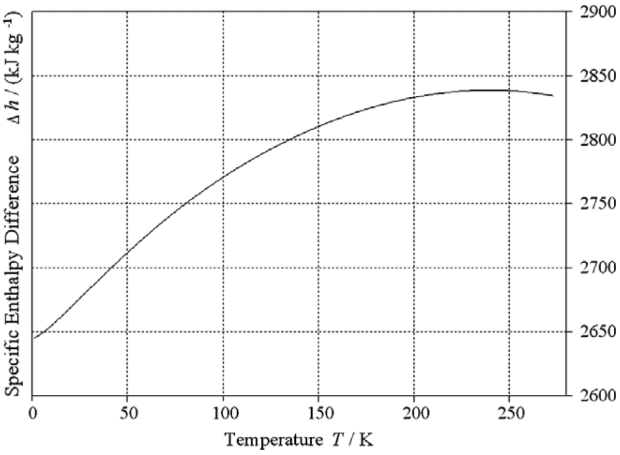

Figure 3.3: Latent heat of sublimation of water ice as a function of temperature, indicating the amount of heat absorbed by the process for each kg of water ice sublimated. The temperature ranges between 0 K and triple point condition (273 K), where water can be in the solid state (see Figure 3.1). Image retrieved from Feistel et al. (2007).

(see Figure 3.1), solid water can transit to the gaseous phase. The sublimation rate is proportional to the temperature of the ice walls T_{wall} (Minissale et al., 2022):

$$\dot{m}_{subl} \propto e^{-1/T_{wall}} \tag{3.5}$$

The latent heat of sublimation, determining the amount of heat subtracted from the walls for each *kg* of ice sublimated, is represented in Figure 3.3.

3.1.3 Condensation, Deposition and Nucleation

Water transiting from vapour to liquid state is said to condensate, while from vapour to solid state is said to deposit. These processes are exothermic. The heat exchanged during these processes is equal to their counterparts, evaporation and sublimation respectively, but with opposite signs. Vapour can form ice grains within the gas flow. This process is called *nucleation*. Since the ice particles embedded in the flow are likely composed of approximately 20-30 water molecules, too few to be treated as crystalline structures, nucleation is considered a gas-liquid transition (condensation) (Schmidt et al., 2008). Once ice nuclei are formed inside the plume, water vapour can condensate at their surface and increase their size. Lastly, condensation and deposition can also occur onto the walls of the crevasses, giving rise to the so-called *wall accretion* process (Kite et al., 2016).

Nucleation occurs when the gas pressure p_{gas} is much higher than the equilibrium pressure $p_{eq}^{l.g.}(T_{gas})$ between the gas and liquid phase at gas temperature T_{gas} (Schmidt et al., 2008). Equation 3.6 defines the *saturation degree*, which indicates the proximity of the flow to saturation conditions (Wölk et al., 2002; Schmidt et al., 2008).

$$S = \frac{p_{gas}}{p_{eq}^{l.g.}(T_{gas})} \tag{3.6}$$

The saturation degree can also be expressed as the ratio of densities ($S = \rho_{gas}/\rho_{eq}^{l.g.}(T_{gas})$) under the assumption of a perfect gas ($p = \rho RT$). When S=1, condensation and evaporation are in equilibrium, thus nucleation is inhibited. If the gas pressure reaches values higher than the equilibrium pressure, condensation dominates and nucleation starts (Yeoh et al., 2015; Wölk et al., 2002). When $S < 1$, endothermic processes (i.e. sublimation and vaporization) prevail.

Constant Name	Symbol	Value(s)
Convection heat transfer coefficient	h_{conv}	2.5-25 W/m^2K - *Natural convection in free air* (Kosky et al., 2013) 15-35 W/m^2K - *Water vapor flow* (see experimental results in section B.2)
Stefan-Boltzmann coefficient	σ	5.67×10^{-8} W/m^2K^4
Emissivity	ε	0.9-0.95 - *Plexiglass* (Rühl et al., 2016) 0.92-0.95 - *PLA* (Morgan et al., 2017; Wijnen et al., 2018)

Table 3.1: Constants used in Equation 3.7 and Equation 3.8 to calculate heat transfer through convection and radiation.

3.2 Heat Transfer Processes

Heat can be exchanged through several processes. In this study, *convection* and *thermal radiation* are considered. These are respectively calculated with the following expressions:

$$\dot{Q} = h_{conv} A (T_{wall} - T_{fluid}) \tag{3.7}$$

$$\dot{Q} = \sigma \varepsilon A (T_{wall}^4 - T_{fluid}^4) \tag{3.8}$$

Each variable is described in the following paragraphs. Typical constant values used throughout this study are reported in Table 3.1.

Convection Heat transfer through convection occurs when there is a fluid in motion between locations with different temperatures. Air moves naturally under the effect of buoyancy forces, generated by density differences. We call this process *natural* or *free* convection. Conversely, we call it *forced* convection when an external force acts on a fluid, inducing a flow. Convection depends on the following parameters (see Equation 3.7): the convection heat transfer coefficient (h_{conv}), the area exposed to the fluid (A), and the temperatures of the object and the fluid (T_{wall} and T_{fluid}).

Radiation Thermal radiation is a form of electromagnetic radiation generated by the movement of particles as a result of thermal excitation. As indicated in Equation 3.8, this form of heat transfer depends on the emissivity of the material (ε), the Stefan-Boltzmann constant (σ), the surface of the object emitting and receiving radiation (A), and the temperatures of the object and the fluid (T_{wall} and T_{fluid}).

3.3 One-Dimensional Flow Theory

A gas flow expanding adiabatically within a channel adheres to the principles of mass, momentum and energy conservation, defined in Equation 3.9, where z is the channel central axis.

$$\begin{cases} \dfrac{d}{dz}(\rho V A) = 0 \\ \dfrac{d}{dz}(\rho V^2 A) = -A\dfrac{dp}{dz} \\ \dfrac{d}{dz}\left(h + \dfrac{V^2}{2}\right) = 0 \end{cases} \tag{3.9}$$

For a perfect gas, the enthalpy is equal to $h = c_p T$ and the speed of sound is equal to $\sqrt{\gamma R_{sp} T}$ (Anderson, 2003). Substituting these relations in the energy conservation equation and considering the temperature equal to T_0 when the flow velocity is zero (stagnation conditions), Equation 3.10 is obtained. The Mach number M and the velocity of the flow can be derived from it, as expressed in Equation 3.11 and Equation 3.12 respectively, holding under the assumptions of adiabatic flow and perfect gas.

$$T_0 = T\left(1 + \frac{V^2}{2c_p T}\right) = T\left(1 + \frac{V^2}{2\frac{\gamma}{\gamma-1}R_{sp}T}\right) = T\left(1 + \frac{\gamma-1}{2}M^2\right) \tag{3.10}$$

$$M = \sqrt{\frac{2}{\gamma-1}\left(\frac{T_0}{T} - 1\right)} \tag{3.11}$$

$$V = \sqrt{\frac{2\gamma}{\gamma-1}R_{sp}T_0\left(1 - \frac{T}{T_0}\right)} \tag{3.12}$$

If an isentropic flow is assumed, therefore when the process is considered reversible, the Poisson relations (Equation 3.13) can be applied to Equation 3.11. The Mach number is defined as a function of the flow pressure by Equation 3.14. The Poisson relation for pressure is applied to Equation 3.12 to obtain the velocity as a function of the pressure p (Equation 3.15).

$$\frac{T}{T_0} = \left(\frac{\rho}{\rho_0}\right)^{\gamma-1} = \left(\frac{p}{p_0}\right)^{\frac{\gamma-1}{\gamma}} \tag{3.13}$$

$$M = \sqrt{\frac{2}{\gamma-1}\left[\left(\frac{p_0}{p}\right)^{\frac{\gamma-1}{\gamma}} - 1\right]} \tag{3.14}$$

$$V = \sqrt{\frac{2\gamma}{\gamma-1}R_{sp}T_0\left[1 - \left(\frac{p}{p_0}\right)^{\frac{\gamma-1}{\gamma}}\right]} \tag{3.15}$$

Finally, we derive the mass flow rate by substituting Equation 3.15 into the continuity equation in Equation 3.9. The density ρ is also substituted with the Poisson relations since this variable is complex to measure experimentally.

$$\begin{aligned} \dot{m} = \rho A V &= \rho_0\left(\frac{p}{p_0}\right)^{\frac{1}{\gamma}} A\sqrt{\frac{2\gamma}{\gamma-1}R_{sp}T_0\left[1 - \left(\frac{p}{p_0}\right)^{\frac{\gamma-1}{\gamma}}\right]} \\ &= \frac{p_0 A}{\sqrt{R_{sp}T_0}}\sqrt{\frac{2\gamma}{\gamma-1}\left(\frac{p}{p_0}\right)^{\frac{2}{\gamma}}\left[1 - \left(\frac{p}{p_0}\right)^{\frac{\gamma-1}{\gamma}}\right]} \end{aligned} \tag{3.16}$$

The flow becomes choked when *critical conditions* are verified. Under these conditions, the mass rate reaches its maximum value, attained for a certain $(p/p_0)_{cr}$. This value can be found by setting to zero the derivative of Equation 3.16 with respect to p/p_0. The result is reported in Equation 3.17. Therefore, the mass flow rate for choked flow can be expressed as in Equation 3.18

$$\left(\frac{p}{p_0}\right)_{cr} = \left(\frac{2}{1+\gamma}\right)^{\frac{\gamma}{\gamma-1}} \tag{3.17}$$

$$\dot{m} = \frac{p_0 A}{\sqrt{R_{sp}T_0}}\sqrt{\gamma}\left(\frac{2}{\gamma+1}\right)^{\frac{\gamma+1}{2(\gamma-1)}} \tag{3.18}$$

Throughout this report, we assume reservoir conditions equal to stagnation conditions, given the very low flow velocity in this location. Consequently, we can replace all the subscripts "0" with "res," and when no subscript is explicitly mentioned, it refers to any arbitrary point along the channel.

Despite the experiments performed in this research involve purely constant cross-sectional area channels (constant A), the final discussion includes a comparison with nozzles with a divergent section. A relation between Mach number and the area ratio between vent and throat of the nozzle is provided in Equation 3.19, valid under the assumption of isentropic flow.

$$\frac{A}{A^*} = \frac{1}{M}\left(\frac{2 + (\gamma - 1)M^2}{\gamma + 1}\right)^{\frac{\gamma+1}{2(\gamma-1)}} \tag{3.19}$$

4

Journal Article: Experimentally-simulated Enceladus' plume velocity dependence on the crevasse wall temperature

How Enceladus' plumes depend on the crevasse wall temperature: an experimental perspective

Fabrizio **Giordano**[a,*], Stéphanie M. **Cazaux**[a,b] and Ferry F.J. **Schrijer**[a]

[a] *Faculty of Aerospace Engineering, Delft University of Technology, Delft, The Netherlands*
[b] *Leiden Observatory, Leiden University, P.O. Box 9513, NL 2300 RA Leiden, The Netherlands*

ARTICLE INFO

Keywords:
Enceladus
Plumes
Experiments
Water vapor
Triple point
Heat transfer
Mach number
Nucleation
Solid fraction
Convection
Thermal radiation

ABSTRACT

In this study, plume experiments were conducted to mimic the thermodynamic conditions on Saturn's moon, Enceladus. The icy moon subsurface ocean and cracks in the surface have been simulated by using a liquid water reservoir and a narrow channel, while the low-pressure environment at Enceladus' surface was achieved with a vacuum chamber. We aimed to examine how channel temperature affected the plume's behavior, testing two models with differing wall temperatures: room temperature and near 0°C. The colder model better replicated Enceladus' plumes, producing a saturated flow in which nucleation of icy particles is possible. A conservative 1.5-3% minimum solid fraction is estimated from measurements and modeling. Pitot-tube measurements indicated Mach numbers around 1 and velocities around 400-500 m/s. Flow temperature and velocity are closely correlated with wall temperature, indicating effective heat transfer. With a plume model based on the energy conservation law, we concluded that supersonic plume velocities observed on Enceladus can be achieved through thermal effects within the icy crust's crevasse, without requiring extreme expansion ratios. Additionally, the research provides evidence of the relationship between the crevasse's expansion ratio and the temperatures of flow and crevasse walls.

1. Introduction

Since the Cassini discovery of water vapour and ice particle plumes from the Enceladus' south polar region in 2005 (Porco et al., 2006), multiple studies have been carried out to characterise these ejections originating from elongated crevasses known as the "Tiger Stripes". The most accepted plume formation theory involves liquid water vaporisation (Porco et al., 2006; Postberg et al., 2009; Ingersoll and Ewald, 2011) from a subsurface ocean laying under a 7-40 *km* thick ice shell (Iess et al., 2014; Thomas et al., 2016; Beuthe et al., 2016; Lucchetti et al., 2017). Cassini observations have provided valuable insights into plume characteristics, including vent temperatures between 145 and 210 K (Spencer et al., 2006; Spencer and Nimmo, 2013; Tenishev et al., 2014), supersonic velocities (Hansen et al., 2006; Tian et al., 2007; Hansen et al., 2008; Smith et al., 2010; Dong et al., 2011; Hansen et al., 2011; Perry et al., 2015; Fu et al., 2021; Portyankina et al., 2022) up to Mach 10 (Teolis et al., 2017), and ice-vapour mass ratios between 0.07 and 0.7 (Kieffer et al., 2009; Ingersoll and Ewald, 2011; Gao et al., 2016).

Multiple theoretical models have been proposed to constrain the heat and mass transfer involved in the geological activity of the moon (Matson et al., 2012; Kite and Rubin, 2016), as well as crevasses geometry and conditions of the water vapour flow (Ingersoll and Pankine, 2010; Nakajima and Ingersoll, 2016; Ingersoll and Nakajima, 2016; Hijden, submitted). Crevasse widths ranging between 0.05-0.075 *m* have been estimated by Nakajima and Ingersoll (2016) to explain the mass flow rate observed from Cassini, while widths of 1 *m* are necessary to avoid freezing of the water interface (Ingersoll and Nakajima, 2016). A strong relation between flow temperature crevasse wall temperature was found by Ingersoll and Pankine (2010) and Nakajima and Ingersoll (2016), with differences below 2 K. Different geometries have been studied by *Hijden (submitted)*, pointing out the influence of nucleation onto the flow temperature.

With a series of laboratory experiments, we aim to further investigate the plumes and validate the existing theoretical models. We have developed a plume model consisting of a water reservoir and a channel, respectively emulating the subsurface ocean of Enceladus and a crevasse in the ice crust. The entire experimental setup has been placed in a vacuum chamber to achieve water triple point conditions. In this study, we investigate the influence of the channel wall temperature on the flow characteristics, with a focus on the heat transfer with the flow, the solid fraction and the venting velocity. The article is organised as follows: Section 2 describes the experimental set-up and the methods used to process the laboratory measurements; Section 3 presents the results of the experiments; in Section 4, we discuss the influence of heat transfer processes on the flow conditions and estimate the solid fraction generated through nucleation; Section 5 compares the experimental results with the Cassini observations; finally, Section 6 outlines the conclusions of this research.

2. Experimental Setup and Data Processing

The experiments were conducted using a plexiglass reservoir containing distilled water to mimic the subsurface ocean and a 3D printed PLA (poly-lactic acid) channel to simulate a crevasse in the ice crust of Enceladus. For this study, we considered a uniform cross-sectional area channel, with a length of $(245 \pm 1)\,mm$ and a diameter of

---

*Corresponding author
`f.giordano-1@student.tudelft.nl` (F. Giordano)

$(5.7 \pm 0.1)\,mm$. A sketch of the experimental setup is given in Fig. 1. The model was placed inside a vacuum chamber, evacuated throughout the experiment by two vacuum pumps to achieve pressures below the saturation point of water vapor, causing the water to boil. The vaporised water flowed through a channel, with temperature and pressure being monitored, before being expelled into the vacuum chamber. Furthermore, total pressure measurements were performed at the vent of the channel. The experiment ends when the pumps are stopped and the chamber is re-pressurised. Additional information on the vacuum chamber and measuring equipment is included in Appendix A.

A first series of experiments was conducted with the channel at room temperature, designated as the *warm model*. A subsequent set of experiments was performed with an ice block encased around the outer surface of the channel, cooling the channel walls and sustaining a uniform wall temperature throughout the experiment. This channel configuration is denoted as the *frozen model*. Melting of ice before starting the experiment ensured that the model was at approximately 0°C. However, as the vacuum chamber reached low pressures, sublimation took place, leading to a cooling effect on the ice. Consequently, the observed model temperatures range between 0 and -5°C.

It is worth mentioning that the base of the model, measuring 45 mm in height, has a larger diameter, designed to facilitate a hermetic coupling with the reservoir and prevent water vapour leakage, as depicted in Fig. 1. However, this design choice results in a less effectively cooled first section of the channel, with wall temperatures around 0-2°C, due to the larger distance between ice and the internal channel surface.

Temperature and pressure are measured in the reservoir and along the channel as indicated in Fig. 1. The sensors produce temperature measurements with an uncertainty of 2°C and pressure measurements with an uncertainty of 0.3-0.6 $mbar$. A description of the sensors employed in this study is given in Appendix A. The acquired data are used to derive other flow parameters. The first is the *saturation degree*, providing an indication of how close the flow is to the saturation condition and defined as in Eq. 1. In this equation, p_{flow} is the flow pressure and $p_{eq}(T_{flow})$ is the *equilibrium pressure*, or *saturated vapour pressure*, dependent on the flow temperature and calculated with the Antoine relation[1] in Eq. 2.

$$S = \frac{p_{flow}}{p_{eq}(T_{flow})} \tag{1}$$

$$p_{eq} = 10^{\mathcal{A}-\frac{\mathcal{B}}{C+T_{flow}}} \tag{2}$$

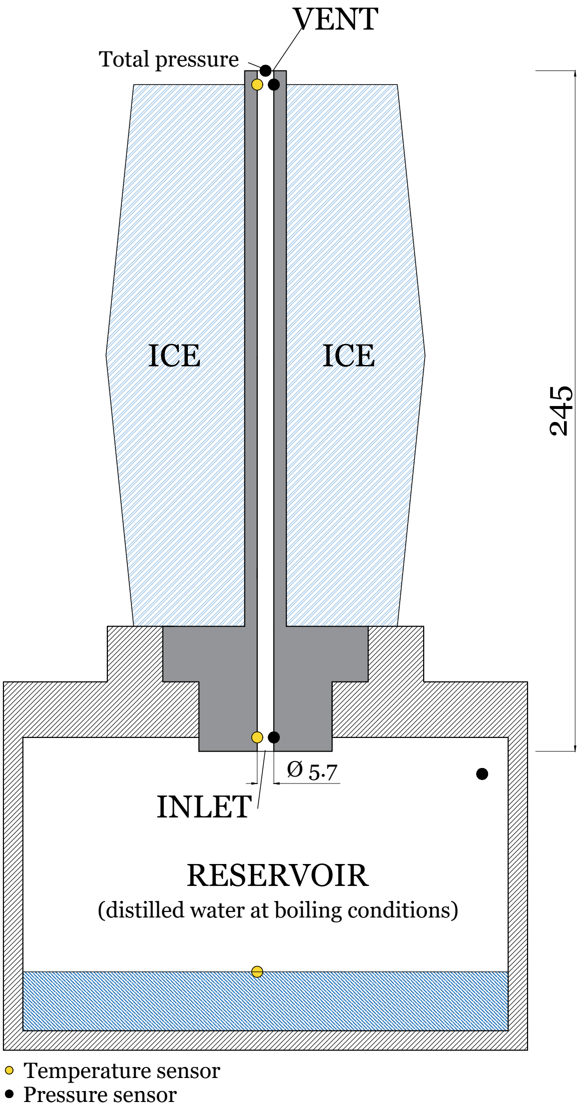

Figure 1: Schematic of the experimental setup: The channel is mounted on top of a plexiglass reservoir containing distilled water. The entire setup is placed in a vacuum chamber. The water begins boiling as the pressure inside the reservoir drops below the saturation pressure of water. Water vapour escapes through the channel, and temperature and pressure are measured with relative sensors, positioned along the channel's length via holes in the channel wall. The *frozen model* also includes a block of ice frozen around the channel to maintain a low wall temperature.

The Mach number (M) is measured at the vent substituting static pressure (p) and total pressure measurements (p_0) in Eq. 3, assuming the flow locally isentropic. If the flow is supersonic, a normal shock wave is formed in front of the Pitot tube. This can be accounted for with the Rayleigh Pitot formula (Anderson Jr, 2003), in Eq. 4. The heat capacity ratio (γ) of water vapour is assumed equal to 4/3.

$$M = \sqrt{\frac{2}{\gamma-1}\cdot\left[\left(\frac{p_0}{p}\right)^{\frac{\gamma-1}{\gamma}}-1\right]} \tag{3}$$

$$\frac{p_0}{p} = \left(\frac{(\gamma+1)^2 M^2}{4\gamma M^2 - 2(\gamma-1)}\right)^{\frac{\gamma}{\gamma-1}} \frac{1-\gamma+2\gamma M^2}{\gamma+1} \tag{4}$$

---

[1] Coefficients $\mathcal{A}$, $\mathcal{B}$ and C have been calculated by the *NIST*, based on the study of Stull (1947): `https://webbook.nist.gov/cgi/cbook.cgi?ID=C7732185&Mask=4&Type=ANTOINE&Plot=on`

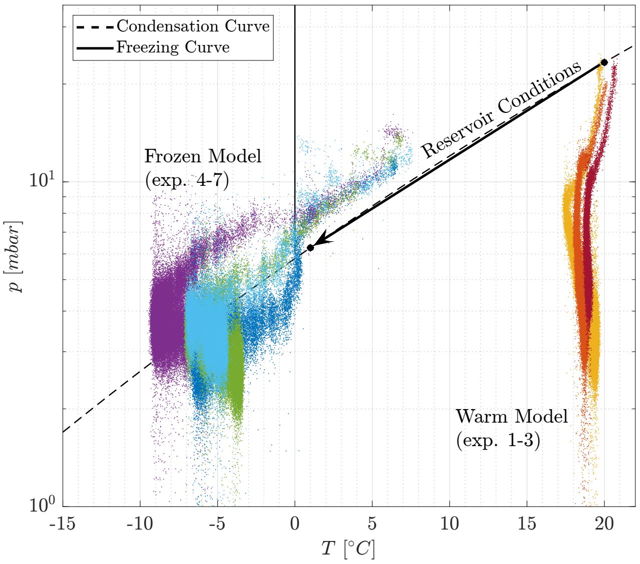

Figure 2: Pressure-temperature conditions of the water vapour flow measured at the vent of 3 warm model experiments (yellow, orange, red) and 4 frozen model experiments (cyan, blue, green, purple). The measurements are acquired from the moment water in the reservoir starts boiling until the flow reaches stable conditions. The black arrow indicates the evolution of reservoir conditions, starting from a temperature between 10 and 20°C and approaching the triple point towards the end of the experiments.

Exp.	Color	T_{wall}	Δt [min]	S	M
1	Yellow	Warm	55	0.15±0.02	0.91±0.12 0.64±0.33
2	Orange	Warm	61	0.17±0.03	-
3	Red	Warm	17	0.21±0.03	-
4	Cyan	Frozen	28	0.81±0.15	1.06±0.17 0.85±0.26
5	Blue	Frozen	40	0.81±0.15	1.17±0.17 0.92±0.26
6	Green	Frozen	47	0.59±0.12	1.13±0.17 0.87±0.31
7	Purple	Frozen	50	0.90±0.17	-

Table 1
Summary of experimental results. Each experiment is associated with a number and a distinct colour on the plot. The duration Δt in minutes and saturation degree S in stable conditions are provided for each experiment. Mach numbers M, maximum and minimum values, are included for experiments where pressure measurements were not compromised.

3. Measurements of Flow Conditions

In this section, we show the results obtained with the warm model and frozen model and describe the differences between them. Flow temperature and pressure are measured along the channel and used to calculate saturation degree (S) and Mach number (M). A summary of the results and uncertainties associated with each experiment is reported in Table 1.

3.1. Temperature-Pressure at the Vent

Fig. 2 illustrates the temperature and pressure data measured during warm and frozen model experiments. The measurements start when the water in the reservoir reaches temperatures between 10 and 20°C and continue until the water temperature has dropped to 0-3°C and the flow has reached stable conditions, therefore when flow temperature and pressure change over time is marginal. The experiment evolves from high to low pressures, starting from pressures above 10 $mbar$ both in the reservoir and in the vacuum chamber when water begins boiling. During the evacuation procedure, the reservoir reaches the triple point condition, while the vacuum chamber stabilizes around 3 $mbar$ within 10 minutes from the beginning of the experiment.

Theoretical models predict a decrease in gas temperature along the channel as a consequence of rapid flow expansion, ultimately reaching saturation conditions (Schmidt et al., 2008; Yeoh et al., 2015; Nakajima and Ingersoll, 2016). While the frozen model yields results consistent with the theory, the flow temperature in the warm model immediately diverges from the saturation curve, maintaining a flow temperature at the vent between 17 and 20°C throughout the experiment. In both scenarios, the flow stabilises at a temperature similar to the wall temperature of the model. Since the wall temperature is the only difference between the 2 models, it must be the primary cause of the difference in these observations.

The venting temperatures of the warm model, higher than the water temperature, suggest a transfer of heat from the warmer walls to the flowing gas. This phenomenon likely involves a significant contribution from convection and thermal radiation, both of which are sensitive to wall temperature.

3.2. Observations of Phase Change

Flow expansion causes the flow temperature (T_{flow}) to decrease, consequently decreasing p_{eq} (see Eq. 2) and increasing S (see Eq. 1). In an isentropic expansion, no heat is exchanged with the walls and no phase change occurs, leading to a very high value of saturation degree ($S \gg 1$). In reality, S values above 1 are not sustainable, since vapour at a pressure above the saturated pressure (p_{eq}) tends to change phase. Therefore, saturation degrees around 1 are expected in the plume models.

Unexpectedly, Fig. 3 shows that the flow in the warm model has a saturation degree well below 1, indicating that the water vapour pressure is lower than p_{eq}. This result suggests that the heat exchanged between flow and wall plays an important role, increasing the flow temperature (T_{flow}) and the saturated vapour pressure (p_{eq}).

On the other hand, Eq. 1 shows that the water vapour flow in the frozen model has a higher saturation level. We can conclude that the colder model temperature allows the flow temperature to decrease during the expansion and causes S to increase. Phase change prevents the flow from becoming super-saturated: when $p_{flow} > p_{eq}$, nucleation occurs,

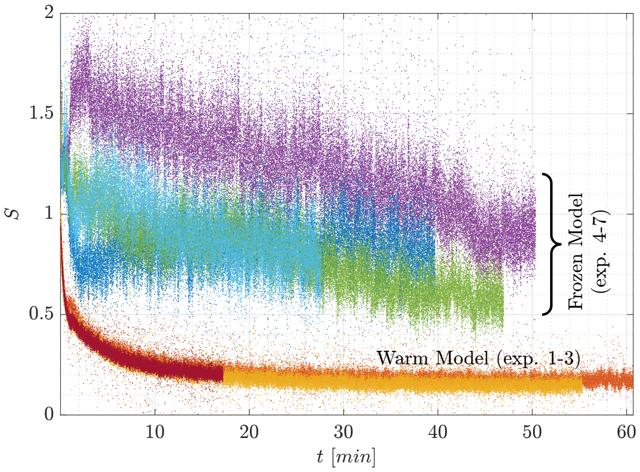

Figure 3: Saturation degree computed with pressure and temperature measurements at the vent of the channel using Eq. 1. for 3 warm model experiments (yellow, orange, red) and 4 frozen model experiments (cyan, blue, green, purple). The colour of each experiment corresponds to the one used in Fig. 2 and is reported in Table 1.

forming ice particles and releasing heat to the flow that increases its temperature. Since Eq. 1 shows values of $S \sim 1$ throughout the first part of the frozen model experiments, nucleation is likely occurring.

Fig. 3 shows a decrease in S with time in the frozen model experiments, reaching values as low as 0.5. This drop suggests a change in the thermal condition of the system. This is likely due to the water temperature decreasing with time. At the end of the experiment, water vapour near the triple point condition ($0°C$ is produced). When expanding, this gas can become colder than the model's temperature, meaning that convection and thermal radiation become significant again, raising the flow temperature. As a result, the equilibrium pressure increases, consequently decreasing the saturation degree, as happened in the warm model.

3.3. Mach Number Measurements

The Mach number of the flow at the vent is determined using Eq. 3 and Eq. 4. The difference between the 2 methods is seen to be less than 2.5%. Given this minimal disparity, Fig. 4 exclusively presents the Mach numbers computed using the isentropic relation. From the analysis are excluded those experiments that reported unreliable pressure measurements, caused by water vapour clogging the high-pressure port of the total pressure probe.

The frozen model exhibits higher Mach numbers compared to the warmer model. In both cases, the flow falls into the transonic regime, suggesting that it experiences choking, even though there is no constriction in the channel. Potential causes of choking are friction and the change in cross-section area from the reservoir to the channel. The heat released to the flow through nucleation or other heat transfer processes can also influence the velocity of the flow through the *Rayleigh effect*. If heat is added to a subsonic flow, the gas is accelerated and, eventually, chokes. However, when heat is introduced to a supersonic flow, it has the opposite effect, slowing down the flow. We call this process *thermal choking*.

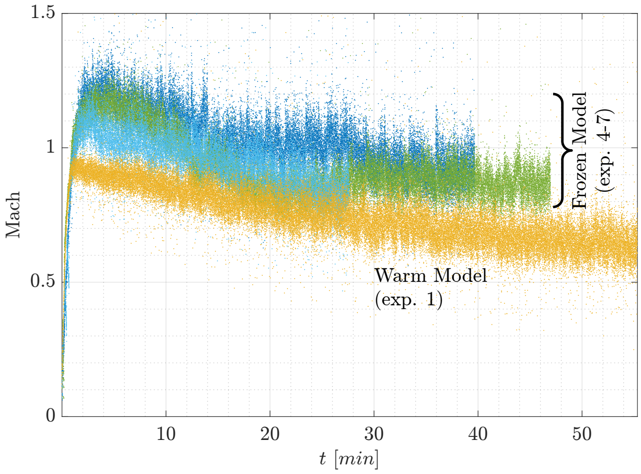

Figure 4: Mach number computed from total and static pressure measurements at the vent of the channel, using the isentropic relation in Eq. 3. Only experiments where pressure measurements were not compromised have been considered: 1 warm model experiment (yellow) and 3 frozen model experiments (cyan, blue, green). The colour of each experiment corresponds to the one used in previous figures and reported in Table 1.

Thermal choking might occur in the warm model. As explained in subsection 3.1, the flow absorbs heat from the warmer walls. This would prevent supersonic velocities, explaining why this model presents Mach numbers always lower than 1, as observed in Fig. 4. A decrease in Mach at the vent with time is also noticed. This is likely due to the decrease in the pressure difference between the reservoir and the chamber. This value is maximum around 1-2 minutes after the water starts boiling, around 8 *mbar*, and decreases to around 4 *mbar* at the end of the experiments.

In the frozen model, heat transfer occurs in the opposite direction in the first minutes of the experiments, from the flow to the model, since $T_{wall} < T_{flow}$. This not only prevents thermal choking, but also introduces the possibility of accelerating the flow to higher velocities, explaining the Mach numbers higher than 1. As the experiments progress, the water temperature in the reservoir decreases and the expanding water vapour temperature achieves a temperature similar to the wall temperature (-5 to $0°C$). This decreases the cooling effects due to the heat transfer with the wall and, consequently, the flow acceleration due to the Rayleigh effect.

4. Heat Exchange between Flow and Models

Results presented in Section 3 are here used to investigate and quantify the influence of heat transfer between the flow and the channel walls. Furthermore, the solid fraction is estimated for frozen model experiments.

4.1. Vent Enthalpy Difference

According to the energy conservation equation in a steady flow, the enthalpy of water vapour in the at the *inlet* of the channel (see Fig. 1) should match the enthalpy at the vent, with additions introduced by heating processes, as expressed in Eq. 5. Using this equation, we calculate the enthalpy excess at the vent (Δh_{vent}) due to heat transfer processes and nucleation throughout the plume experiments.

$$c_{p,inlet}T_{inlet} = c_{p,vent}T_{vent} + \frac{V_{vent}^2}{2} - \Delta h_{vent} \tag{5}$$

In Eq. 5, c_p is the specific heat capacity of water vapour, dependent on the flow temperature at a certain location (i.e. T_{inlet}, T_{vent}). The inlet enthalpy does not include the kinetic energy term, since the velocity in this location is assumed ~0. The velocity at the vent (V_{vent}) is determined multiplying the the Mach number obtained in Section 3.3 by the speed of sound ($c_{s,vent}$=$\sqrt{\gamma R_{sp} T_{vent}}$), where R_{sp}=$R/\mathcal{M}$, and $\mathcal{M}$ represents the molar mass of H_2O.

The results reported in Fig. 5 denote a peak in Δh_{vent} in the first minutes of the experiments. In this phase, the pressure difference between the reservoir and vent is highest, favouring higher vent velocities. The frozen model presents values nearly double those of the warm model, despite its velocity is only slightly higher. This discrepancy suggests the presence of an additional process heating the flow: nucleation. A possible interpretation is that the temperature difference between water vapour flow and the frozen model is highest at the beginning of the experiment, when water is above 10°C. This would result in more effective cooling of the flow due to the larger amount of heat absorbed by the walls, increasing flow saturation S (see Eq. 2 and discussion in Section 3.2).

At the end of the experiments, the flow temperature and pressure were stable over time. In these conditions, Fig. 5 shows Δh_{vent} values similar for both models, suggesting that nucleation in the frozen model decreased considerably and, with it, the cooling effect of the channel walls.

4.2. Heat Exchange between Flow and Model

Values of Δh (J/kg) found in Section 4.1 are here used to estimate the amount of heat absorbed by the flow (W). As expressed in Eq. 6, we consider convection, thermal radiation and nucleation as main contributors to the total enthalpy difference (Δh_{vent}) observed at the vent.

$$\dot{Q}_{tot} = \dot{Q}_{conv} + \dot{Q}_{rad} + \dot{Q}_{nucl} = \dot{m}_{flow}\Delta h_{vent} \tag{6}$$

As discussed in Section 3, phase change can be disregarded in the warm model, given the low saturation degree. Therefore, only convection and thermal radiation are quantified. To solve Eq. 6, an estimate of the mass flow rate is needed. Appendix C provides different methods to obtain this value. Calculations show that $\dot{m}_{flow}$ is likely around 10^{-6}-10^{-5} kg/s under stable conditions. By substituting $\dot{m}_{flow}$ and Δh_{vent} into Eq. 6, we obtain a total power in the range of 3×10^{-2} to 3 W.

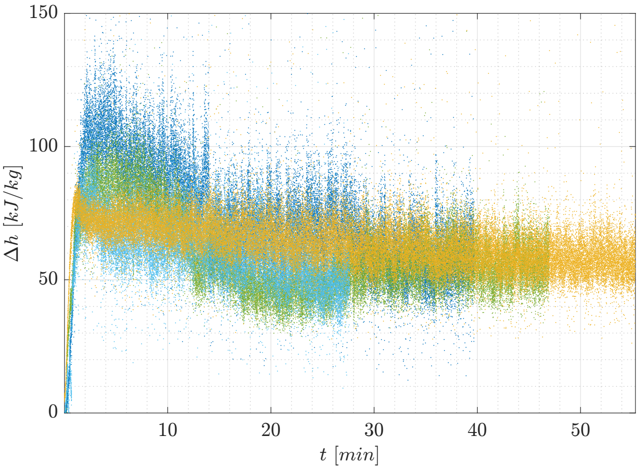

Figure 5: Enthalpy difference between vent and inlet computed with Eq. 5 for 1 warm model experiment (yellow) and 3 frozen model experiments (cyan, blue, green). Velocity at the vent has been derived from the Mach number measurements, multiplied by the speed of sound under the ideal gas assumption. The colour of each experiment corresponds to the one used in previous figures and reported in Table 1.

The average temperature difference $T_{wall} - T_{flow}$ needed to motivate this value of $\dot{Q}_{tot}$ is calculated solving Eq. 7 and Eq. 8. In these equations, h_{conv} is the convective heat transfer coefficient, A is the area of the channel exposed to the flow, and ε is the emissivity of PLA. Calculations of the heat transfer coefficient h_{conv} are shown in Appendix B.

$$\dot{Q}_{conv} = h_{conv}A\left(T_{wall} - T_{flow}\right) \tag{7}$$

$$\dot{Q}_{rad} = \varepsilon\sigma A\left(T_{wall}^4 - T_{flow}^4\right) \tag{8}$$

Values of $|T_{wall} - T_{flow}|$ in the order of 10 K have been found with the calculations shown in Appendix D. This value is not intended to represent the real temperature difference between the wall and the flow, but rather as an average condition of the system. Wall temperature is difficult to measure as it changes considerably not only along the channel, but also inside the wall.

4.3. Solid fraction

While nucleation was considered negligible in the warm model, it can significantly impact the flow inside the frozen model, as evidenced in Section 3.2. This section aims to quantify the solid fraction in the flow of the frozen model produced through nucleation, defined as the mass of ice particles nucleating ($\dot{m}_{nucl}$) over the total mass of the flow ($\dot{m}_{flow}$).

In Eq. 9, we find the formula for calculating the heat released through nucleation, which is directly proportional to $\dot{m}nucl$ and L_v. The latter is either the latent heat of vaporization or sublimation of water, depending on whether the flow temperature is above or below 273.15 K. By definition, $\dot{m}_{nucl}$ is equal to the solid fraction f of the flow times the mass flow rate $\dot{m}_{flow}$. On a first approximation, nucleation is considered the only process contributing to the total Δh.

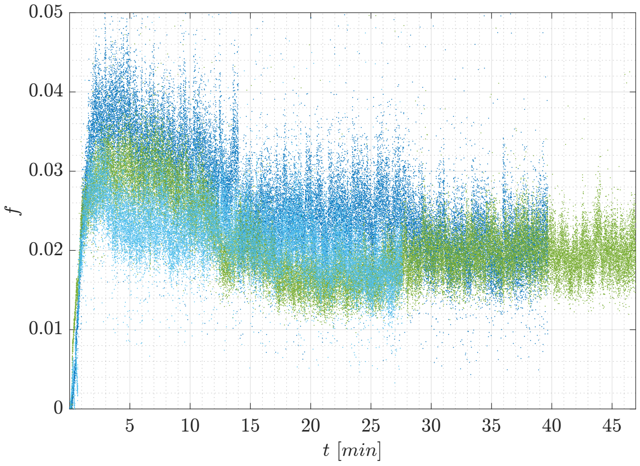

Figure 6: Solid fraction at the vent of the frozen model computed from enthalpy difference at the vent (Δh_{vent}) using Eq. 9. Nucleation is assumed the only process providing heat to the flow, therefore $\Delta h_{vent} = q_{nucl}$. Only frozen model experiments have been considered since the warm model is assumed to have negligible nucleation. The colour of each experiment corresponds to the one used in previous figures and reported in Table 1 (exp. 4: cyan, exp. 5: blue, exp. 6: green).

Therefore, Eq. 6 can be simplified to Eq. 10. The solid fraction is subsequently computed by combining the two expressions of $\dot{Q}_{nucl}$, resulting in Eq. 11.

$$\dot{Q}_{nucl} = \dot{m}_{nucl} L_v = f \dot{m}_{flow} L_v \tag{9}$$

$$\dot{Q}_{nucl} = \dot{m}_{flow} \Delta h_{vent} \tag{10}$$

$$f = \frac{\Delta h_{vent}}{L_v} \tag{11}$$

Values of solid fraction needed to account for the excess enthalpy at the vent observed in Fig. 5 have been plotted for 3 frozen model experiments in Fig. 6, showing f values between 1.5% and 3%, with the highest values observed in the first 10-15 minutes of each experiment. The decrease in solid fraction with time is expected, since the saturation degree S at the vent decreases with time too (Fig. 3).

It is worth noting that including convection and thermal radiation cooling or heating effects would influence these estimates and Eq. 10 would not hold anymore. In the first phase of the frozen model experiments, the flow is cooled by the walls ($T_{wall} < T_{flow}$), with $\dot{Q}_{conv}$ and $\dot{Q}_{rad}$ assume negative values. Therefore, under these conditions, nucleation is underestimated (see Eq. 6) and the results in Fig. 6 can be regarded as conservative estimates representing the minimum solid fraction achieved in our experiments.

5. Comparing experimental results with Cassini observations

In this section, we compare the experimental results with the plume characteristics inferred from Cassini observations and theoretical models found in the literature. The objective is to determine whether lowering the wall temperature would yield a closer representation of the plume characteristics. Specifically, we examine the plume velocity as a control parameter.

5.1. Wall Temperature

The plume flow on Enceladus is expected to have a temperature within 2 K to that of the ice walls (Ingersoll and Pankine, 2010; Nakajima and Ingersoll, 2016). In the warm model experiments, the flow temperature has been estimated to be around 10 K higher than the wall temperature (see Section 4.2 and Appendix D). The high heat addition experienced by the water vapour, attributed to convective and radiative heat transfer with the model walls, increases the flow temperature along the channel. This prevents saturated flow and, consequently, phase change processes, which are considered the main cause of thermal equilibrium between flow and walls according to Nakajima and Ingersoll (2016).

5.2. Solid Fraction

Cassini observations have been used by Kieffer et al. (2009) and Ingersoll and Ewald (2011) to infer the solid fraction of the plumes. An ice-vapour mass ratio between 0.1 and 0.7 has been found by these authors. Our experimental results indicate a lower solid fraction, around 0.03. The reasons for this difference can be attributed mainly to the temperature and length of the channel.

While the experimental model has a temperature of 273 K, the real Enceladean crevasse can reach temperatures below 220 K. As observed in Section 4.3, at the beginning of the experiments there is a larger flow-wall temperature difference, allowing for higher heat absorbed by the walls. As a consequence, the flow becomes supersaturated and nucleation is initiated, increasing the total solid fraction. With lower model temperatures, we expect to observe higher heat absorption and, consequently, higher nucleation rates.

The second aspect to consider is the model's scale. The length of Enceladus crevasses is estimated in the order of kilometres, with widths around 0.1-1 m. In comparison, our model is at least 10 times shorter. A longer channel would have a higher possibility of generating nucleation since the flow could exchange heat with the walls for a longer time.

5.3. Velocity

The velocity measurements taken at the vent of the experimental plume models indicate that the flow is (thermally) choked, with the colder model displaying higher Mach numbers. A possible explanation has been found in the Rayleigh effect, which suggests that the removal of heat can accelerate a supersonic flow. In the following paragraphs, we examine the possibility of reaching velocities comparable to those observed on Enceladus by further cooling the experimental setup.

Using the energy conservation equation in Eq. 5, we have calculated potential flow velocities at the vent, assuming the reservoir to be at triple point conditions and considering various combinations of T_{flow} at the vent and Δh_{vent}. Temperatures between 140 and 300 have been considered,

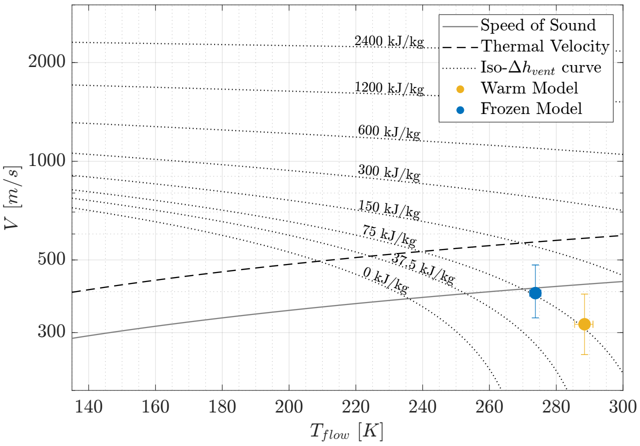

Figure 7: Average flow velocity at the vent in the frozen model (blue) and warm model (yellow). Minimum and maximum values of velocity and wall temperature are indicated with error bars. Indicative velocities for different vent flow temperatures (T_{flow}) have been estimated through the energy conservation equation (Eq. 5) for different values of Δh_{vent} (black dotted lines). These estimations are independent of the channel geometry. The isentropic expansion is characterised by $\Delta h_{vent} = 0$. Speed of sound is calculated as $c_{s,vent} = \sqrt{\gamma R_{sp} T_{vent}}$. Thermal velocity is determined with the formula used by Hansen et al. (2011): $v_{th} = \sqrt{8 R_{sp} T_{vent} / \pi}$.

a range that includes both Cassini observations (Spencer et al., 2006; Spencer and Nimmo, 2013; Tenishev et al., 2014) and experimental measurements of this study. This model, which we refer to as *iso-enthalpy model*, imposes no constraints on the geometry of the channel. The plume velocity estimates with this method are reported in Fig. 7, alongside data points from the warm and frozen model, as well as velocity values obtained from different studies. The black dotted lines indicate the velocities associated with the chosen levels of Δh_{vent}. Experimentally, Δh_{vent} values ranging from 0 to 150 kJ/kg have been observed. The lower limit corresponds to an isentropic expansion.

Fig. 7 shows that lower plume temperatures and higher enthalpy levels can achieve higher flow velocities. This enthalpy addition (Δh_{vent}) can originate from multiple sources, including nucleation, convection, and thermal radiation. Several studies, including those of Kieffer et al. (2009) and Ingersoll and Ewald (2011), have indicated that T_{wall} and T_{flow} are closely correlated, with differences within 2 K. If we apply this assumption to our model, lower wall temperatures result in lower flow temperatures and, consequently, higher flow velocities.

However, velocities obtained with the iso-enthalpy model eventually surpass the thermal velocity (dashed line in Fig. 7) for sufficiently low flow temperatures. The efficiency of the heat exchange with the walls is expected to decrease significantly beyond this threshold since the thermal velocity of the particles and the number of particle collisions with the walls would decrease. Consequently, decreasing T_{flow} below 210 K could become unfeasible by solely reducing the wall temperature.

A yellow-blue gradient line has been plotted on top of the 0 *kJ/kg* (isentropic) curve in Fig. 8, indicating that a divergent section of the channel is required to achieve lower flow temperatures. This channel geometry is characterised by a certain exit-throat area ratio (A_{exit}/A_{th}), known as the expansion ratio. While a flow inside a straight channel (expansion ratio of 1) can achieve a maximum velocity corresponding to the sound speed and minimum temperatures of 235 K, expansion ratios around 1.5-2 would sustain velocities of 600-1000 *m/s* and flow temperatures of 140-180 K.

Fig. 8 shows velocities inferred from Cassini observations by several authors. Estimates obtained from UVIS by Hansen et al. (2008) and INMS observations by Smith et al. (2010) and Dong et al. (2011) are consistent with the estimates of the iso-enthalpy model for Δh_{vent} similar to those observed experimentally. The lower velocities found by Hansen et al. (2006) and Tian et al. (2007) would suggest higher wall temperatures or an under-expanded crevasse (i.e. smaller A_{exit}/A_{th}). However, it should be noted that these studies were published when plumes had just been discovered and few observations were available. Studies by Hansen et al. (2011) and Portyankina et al. (2022) reprocessed these plume observations obtaining higher velocities.

The results from Cassini UVIS observations exceed the energy levels observed in the experiments. Assuming $T_{flow} \approx T_{wall}$, convective and radiative heat transfers with the crevasse walls can be neglected compared to the heat provided by nucleation. With this assumption, an enthalpy addition of 600-1200 *kJ/kg* can source from a solid fraction between 0.35 and 0.7, in agreement with Ingersoll and Ewald (2011). Nevertheless, UVIS plume observations were taken several kilometres above Enceladus' surface, after the plume experienced additional acceleration through free expansion in vacuum (Yeoh et al., 2017). Therefore, estimates obtained from Hansen et al. (2011) and Portyankina et al. (2022) correspond to an upper limit for the plume velocity at the vent.

6. Conclusion

We performed plume experiments simulating the thermodynamic conditions found on Enceladus with a water reservoir for the subsurface ocean, a channel for the crevasses, and a vacuum chamber to recreate the low pressures at the surface of the moon. As the pressure decreases, the water reaches boiling conditions and vaporises. Water vapour accelerates through the channel, where flow temperature and pressure are measured, and is ejected in the vacuum chamber.

Two models with different temperatures have been tested. The measurements revealed that the frozen plume model is better representative of the real Enceladus plumes. In particular:

1. Convective and radiative heat transfer, highly dependent on the model temperature, play a crucial role in

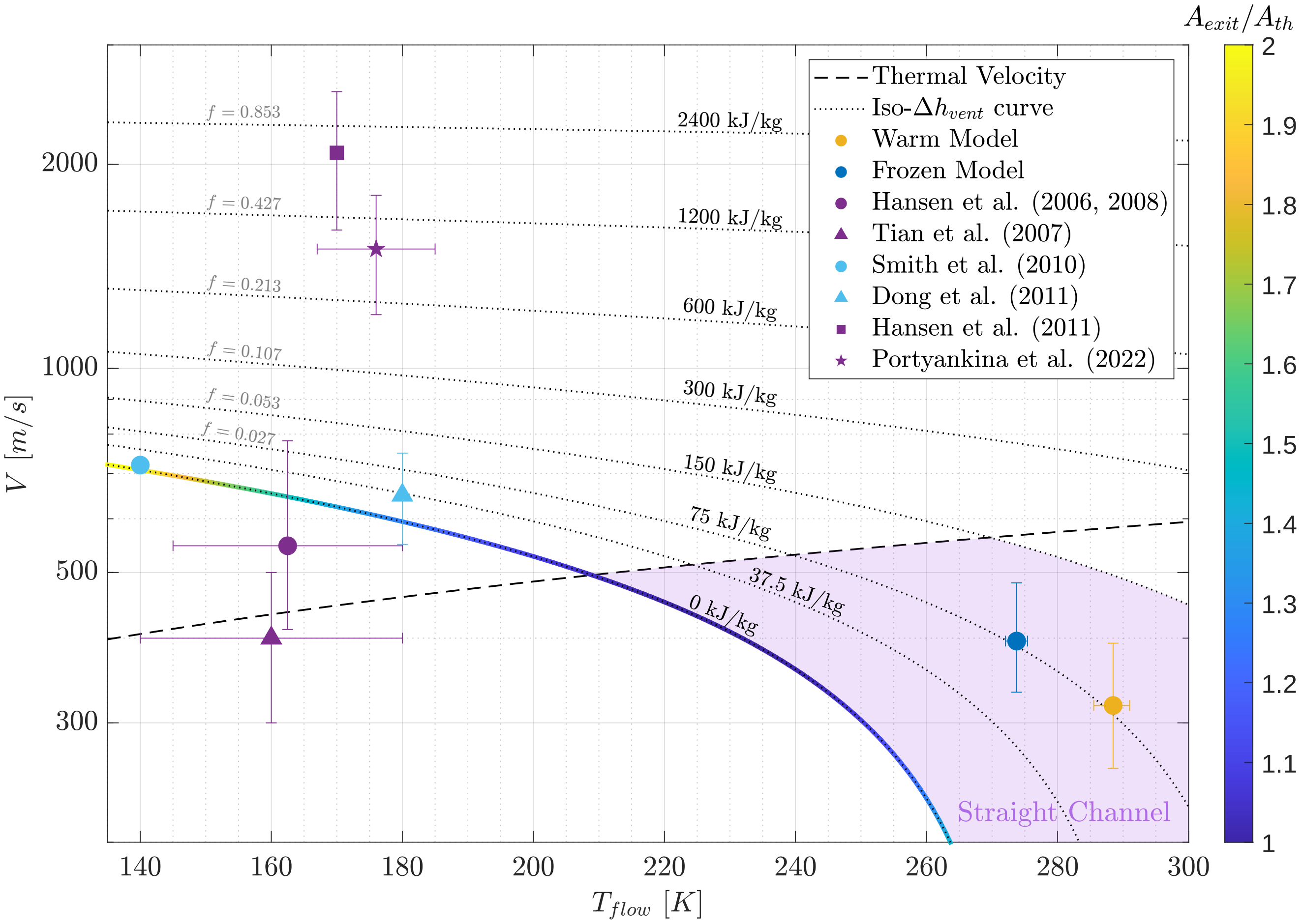

Figure 8: Average flow velocity at the vent in the frozen model (blue) and warm model (yellow). Indicative velocities for different vent flow temperatures have been estimated through the energy conservation equation (Eq. 5) for different values of Δh_{vent} (black dotted lines). These estimations are independent of the channel geometry. The isentropic expansion is characterised by $\Delta h_{vent} = 0$. A blue-yellow gradient line overlaps this iso-enthalpy curve, illustrating the different channel expansion ratios (A_{exit}/A_{th}) necessary to achieve a specific flow velocity and temperature Results from other authors have been reported for comparison: *UVIS* Cassini observations in purple (Hansen et al., 2006; Tian et al., 2007; Hansen et al., 2008, 2011; Portyankina et al., 2022), and *INMS* Cassini observations in cyan (Smith et al., 2010; Dong et al., 2011). Minimum and maximum values of velocity and wall temperature are indicated with error bars. Speed of sound is calculated as $c_{s,vent} = \sqrt{\gamma R_{sp} T_{vent}}$. Thermal velocity is determined with the formula used by Hansen et al. (2011): $v_{th} = \sqrt{8 R_{sp} T_{vent}/\pi}$. The purple-shaded region illustrates the range of flow temperature-velocity conditions achievable within a straight channel geometry. Each iso-enthalpy line is linked to an estimated solid fraction (f) required to generate that specific level of enthalpy excess.

the plume experiments and are the main cause of non-saturated flow in a room temperature model;

2. Saturated flow conditions and visible condensation onto the channel walls of the frozen model have been observed. Nucleation is possible, despite the absence of a geometric throat in the channel, and the solid fraction is estimated around 1.5-3%;
3. The flow within a straight channel (i.e. without throat) can experience choking due to thermal effects (thermal choking). While the flow in the warm model is likely slowed to subsonic velocities by the heat exchange with the wall at high temperatures, the colder model absorbs heat from the flow and allows for higher Mach numbers;
4. A new plume model based on the conservation of energy has been formulated, called *iso-enthalpy model*. Enceladus' crevasses with a straight channel configuration can have velocities above the speed of sound (Mach>1). The minimum flow temperature achievable with this geometrical configuration is around 210-235 K. Assuming that T_{wall} and T_{flow} are strictly coupled, observations of ice temperatures colder than 210 K in correspondence of the tiger stripes imply crevasses with an expansion ratio higher than 1.

Our research highlights the importance of creating models that faithfully replicate the conditions on Enceladus, starting with the model temperature as a key parameter. Future plume experiments should investigate even lower model temperatures and evaluate the impact of channel geometry (i.e. different expansion ratios, throat diameters...) on the flow velocity and temperature. Furthermore, higher accuracy measurement techniques are essential in order to investigate nucleation in the flow, starting from the assessment of the wall temperature and, consequently, heat transfer with the model.

References

Anderson Jr, J.D., 2003. Modern compressible flow.

Beuthe, M., Rivoldini, A., Trinh, A., 2016. Enceladus's and dione's floating ice shells supported by minimum stress isostasy. Geophysical Research Letters 43, 10–088. doi:`https://doi.org/10.1002/2016GL070650`.

Bridgeman, O.C., Aldrich, E.W., 1964. Vapor pressure tables for water. Journal of Heat Transfer 86, 279–286. doi:`https://doi.org/10.1115/1.3687121`.

Crifo, J., 1989. Inferences concerning water vapour viscosity and mean free path at low temperatures. Astronomy and Astrophysics, Vol. 223, NO. OCT (I), P. 365, 1989 223, 365.

David, K., Gorham, J., Kim, S., Miller, P., Minkus, C., 2006. Aeronautical wind tunnels, europe and asia, Library of Congress Washington DC Federal Research Div.

Dong, Y., Hill, T.W., Teolis, B.D., Magee, B.A., Waite, J.H., 2011. The water vapor plumes of enceladus. Journal of Geophysical Research: Space Physics 116. doi:`https://doi.org/10.1029/2011ja016693`.

Fu, M., Gu, H., Cui, J., Xiao, Z., He, F., Wei, Y., Ren, Z., 2021. On the structure of the enceladus plume. Monthly Notices of the Royal Astronomical Society 504, 6216–6222. doi:`10.1093/mnras/stab1265`.

Gao, P., Kopparla, P., Zhang, X., Ingersoll, A.P., 2016. Aggregate particles in the plumes of enceladus. Icarus 264, 227–238. doi:`https://doi.org/10.1016/j.icarus.2015.09.030`.

Hansen, C.J., Esposito, L., Stewart, A.I.F., Colwell, J., Hendrix, A., Pryor, W., Shemansky, D., West, R., 2006. Enceladus' water vapor plume. Science 311, 1422–1425. doi:`https://doi.org/10.1126/science.1121254`.

Hansen, C.J., Esposito, L.W., Stewart, A.I.F., Meinke, B., Wallis, B., Colwell, J.E., Hendrix, A.R., Larsen, K., Pryor, W., Tian, F., 2008. Water vapour jets inside the plume of gas leaving enceladus. Nature 456, 477–479. doi:`https://doi.org/10.1038/nature07542`.

Hansen, C.J., Shemansky, D.E., Esposito, L.W., Stewart, A.I.F., Lewis, B.R., Colwell, J.E., Hendrix, A.R., West, R.A., Waite, J.H., Teolis, B., Magee, B.A., 2011. The composition and structure of the enceladus plume. Geophysical Research Letters 38. doi:`https://doi.org/10.1029/2011gl047415`.

Iess, L., Stevenson, D., Parisi, M., Hemingway, D., Jacobson, R., Lunine, J., Nimmo, F., Armstrong, J., Asmar, S., Ducci, M., et al., 2014. The gravity field and interior structure of enceladus. Science 344, 78–80. doi:`DOI:10.1126/science.1250551`.

Ingersoll, A.P., Ewald, S.P., 2011. Total particulate mass in enceladus plumes and mass of saturn's e ring inferred from cassini ISS images. Icarus 216, 492–506. doi:`https://doi.org/10.1016/j.icarus.2011.09.018`.

Ingersoll, A.P., Nakajima, M., 2016. Controlled boiling on enceladus. 2. model of the liquid-filled cracks. Icarus 272, 319–326. URL: `https://doi.org/10.1016/j.icarus.2015.12.040`, doi:`10.1016/j.icarus.2015.12.040`.

Ingersoll, A.P., Pankine, A.A., 2010. Subsurface heat transfer on enceladus: Conditions under which melting occurs. Icarus 206, 594–607. doi:`https://doi.org/10.1016/j.icarus.2009.09.015`.

Kieffer, S.W., Lu, X., McFarquhar, G., Wohletz, K.H., 2009. A redetermination of the ice/vapor ratio of enceladus' plumes: Implications for sublimation and the lack of a liquid water reservoir. Icarus 203, 238–241. doi:`https://doi.org/10.1016/j.icarus.2009.05.011`.

Kite, E.S., Rubin, A.M., 2016. Sustained eruptions on enceladus explained by turbulent dissipation in tiger stripes. Proceedings of the National Academy of Sciences 113, 3972–3975. doi:`10.1073/pnas.1520507113`.

Kosky, P., Balmer, R., Keat, W., Wise, G., 2013. Chapter 12 - mechanical engineering, in: Kosky, P., Balmer, R., Keat, W., Wise, G. (Eds.), Exploring Engineering (Third Edition). third edition ed.. Academic Press, Boston, pp. 259–281. doi:`https://doi.org/10.1016/B978-0-12-415891-7.00012-1`.

Lucchetti, A., Pozzobon, R., Mazzarini, F., Cremonese, G., Massironi, M., 2017. Brittle ice shell thickness of enceladus from fracture distribution analysis. Icarus 297, 252–264. doi:`https://doi.org/10.1016/j.icarus.2017.07.009`.

Matson, D.L., Castillo-Rogez, J.C., Davies, A.G., Johnson, T.V., 2012. Enceladus: A hypothesis for bringing both heat and chemicals to the surface. Icarus 221, 53–62. doi:`10.1016/j.icarus.2012.05.031`.

Nakajima, M., Ingersoll, A.P., 2016. Controlled boiling on enceladus. 1. model of the vapor-driven jets. Icarus 272, 309–318. doi:`https://doi.org/10.1016/j.icarus.2016.02.027`.

Nusselt, W., 1931. Der wärmeaustausch zwischen wand und wasser im rohr. Forschung auf dem Gebiet des Ingenieurwesens A 2, 309–313.

Perry, M., Teolis, B., Hurley, D., Magee, B., Waite, J., Brockwell, T., Perryman, R., McNutt, R., 2015. Cassini INMS measurements of enceladus plume density. Icarus 257, 139–162. doi:`https://doi.org/10.1016/j.icarus.2015.04.037`.

Porco, C.C., Helfenstein, P., Thomas, P.C., Ingersoll, A.P., Wisdom, J., West, R., Neukum, G., Denk, T., Wagner, R., Roatsch, T., Kieffer, S., Turtle, E., McEwen, A., Johnson, T.V., Rathbun, J., Veverka, J., Wilson, D., Perry, J., Spitale, J., Brahic, A., Burns, J.A., DelGenio, A.D., Dones, L., Murray, C.D., Squyres, S., 2006. Cassini observes the active south pole of enceladus. Science 311, 1393–1401. doi:`https://doi.org/10.1126/science.1123013`.

Portyankina, G., Esposito, L.W., Aye, K.M., Hansen, C.J., Ali, A., 2022. Modeling the complete set of cassini's UVIS occultation observations of enceladus' plume. Icarus 383, 114918. doi:`https://doi.org/10.1016/j.icarus.2022.114918`.

Postberg, F., Kempf, S., Schmidt, J., Brilliantov, N., Beinsen, A., Abel, B., Buck, U., Srama, R., 2009. Sodium salts in e-ring ice grains from an ocean below the surface of enceladus. Nature 459, 1098–1101. doi:`10.1038/nature08046`.

Rapp, B.E., 2017. Chapter 9-fluids. Microfluidics: Modelling, mechanics and mathematics , 263.

Schmidt, J., Brilliantov, N., Spahn, F., Kempf, S., 2008. Slow dust in enceladus' plume from condensation and wall collisions in tiger stripe fractures. Nature 451, 685–688. doi:`10.1038/nature06491`.

Smith, H.T., Johnson, R.E., Perry, M.E., Mitchell, D.G., McNutt, R.L., Young, D.T., 2010. Enceladus plume variability and the neutral gas densities in saturn's magnetosphere. Journal of Geophysical Research: Space Physics 115. doi:`https://doi.org/10.1029/2009ja015184`.

Spencer, J.R., Nimmo, F., 2013. Enceladus: An active ice world in the saturn system. Annual Review of Earth and Planetary Sciences 41, 693–717. doi:`https://doi.org/10.1146/annurev-earth-050212-124025`.

Spencer, J.R., Pearl, J.C., Segura, M., Flasar, F.M., Mamoutkine, A., Romani, P., Buratti, B.J., Hendrix, A.R., Spilker, L.J., Lopes, R.M.C., 2006. Cassini encounters enceladus: Background and the discovery of a south polar hot spot. Science 311, 1401–1405. doi:`https://doi.org/10.1126/science.1121661`.

Stull, D.R., 1947. Vapor pressure of pure substances. organic and inorganic compounds. Industrial & Engineering Chemistry 39, 517–540. doi:`https://doi.org/10.1021/ie50448a022`.

Tenishev, V., Öztürk, D.C.S., Combi, M.R., Rubin, M., Waite, J.H., Perry, M., 2014. Effect of the tiger stripes on the water vapor distribution in enceladus' exosphere. Journal of Geophysical Research: Planets 119, 2658–2667. doi:`https://doi.org/10.1002/2014JE004700`.

Teolis, B.D., Perry, M.E., Hansen, C.J., Waite, J.H., Porco, C.C., Spencer, J.R., Howett, C.J.A., 2017. Enceladus plume structure and time variability: Comparison of cassini observations. Astrobiology 17, 926–940. doi:`https://doi.org/10.1089/ast.2017.1647`.

Thomas, P., Tajeddine, R., Tiscareno, M., Burns, J., Joseph, J., Loredo, T., Helfenstein, P., Porco, C., 2016. Enceladus's measured physical libration requires a global subsurface ocean. Icarus 264, 37–47. doi:`https://doi.org/10.1016/j.icarus.2015.08.037`.

Tian, F., Stewart, A., Toon, O., Larsen, K., Esposito, L., 2007. Monte carlo simulations of the water vapor plumes on enceladus. Icarus 188, 154–161. doi:`https://doi.org/10.1016/j.icarus.2006.11.010`.

Yeoh, S.K., Chapman, T.A., Goldstein, D.B., Varghese, P.L., Trafton, L.M., 2015. On understanding the physics of the enceladus south polar plume via numerical simulation. Icarus 253, 205–222. doi:`10.1016/j.icarus.2015.02.020`.

Yeoh, S.K., Li, Z., Goldstein, D.B., Varghese, P.L., Levin, D.A., Trafton, L.M., 2017. Constraining the enceladus plume using numerical simulation and cassini data. Icarus 281, 357–378. doi:`https://doi.org/10.1016/j.icarus.2016.08.028`.

A. Experimental Equipment

This section describes the laboratory equipment used for the plume experiments: the Vacuum Chamber and Pumps, the thermocouples, and the pressure sensors. Additionally, we provide uncertainties associated with the measuring equipment.

A.1. Vacuum Chamber and Pumps

A section of the *Hypersonic Test Facility Delft (HTFD)* is utilised as vacuum chamber. A schematic of the HTFD is provided by David et al. (2006). The minimum pressure observed in the vacuum chamber is around 1 *mbar*. The vacuum pumps evacuate the chamber throughout the duration of an experiment to guarantee the lowest pressure possible. Because water vapour is continuously ejected into the vacuum chamber, the typical pressure achieved in the vacuum chamber during a plume experiment is (3.5 ± 0.5) *mbar* after 10 minutes from the start of evacuation and does not change significantly with time.

A.2. Temperature Measurements

Temperature measurements were acquired with type-T thermocouples, operating in a temperature range between $-270\ °C$ and $400\ °C$.

Their uncertainty is estimated around $0.11\ °C$ when averaging the measurements over time, and $0.27\ °C$ when considering a single temperature reading.

A.3. Pressure Measurements

The reservoir pressure was determined based on the water temperature at boiling conditions, employing the Antoine equation:

$$\log_{10} p_{res} = \mathcal{A} - \frac{\mathcal{B}}{C + T_{water}} \tag{12}$$

where $\mathcal{A}$, $\mathcal{B}$ and C are gas-related parameters with values of 5.40221, 1838.675, and -31.737 respectively[2].

Differential pressure sensors have been employed to determine the pressure in other locations along the channel. Each sensor comprises a high-pressure port and a low-pressure port and outputs a voltage signal proportional to the pressure difference between the two ports. The maximum pressure difference detectable ranges between 12.5 and 25 *mbar*, with an uncertainty of 0.3-0.6 *mbar*, depending on the specifications of each sensor.

A single differential pressure sensor is used to measure the pressure difference between the reservoir and vacuum chamber and derive the absolute pressure in the latter. Since the low-pressure port of all the differential pressure sensors was exposed to the identical vacuum chamber pressure, it is possible to derive the absolute pressure in each location knowing the vacuum chamber pressure.

B. Convective Heat Transfer Coefficient h_{conv}

When the model is in static conditions, the measured coefficient of convective heat transfer is around 2.5 and 25 (Kosky et al., 2013), with a lower value observed in vacuum conditions. In static conditions, we measure the model temperature with thermocouples inside the channel. Thermal equilibrium is quickly reached between the air inside the channel and the surface of the channel itself.

In the presence of flow in the channel, h_{conv} has been calculated from Eq. 13.

$$h_{conv} = \frac{Nu}{d} k \tag{13}$$

The variables in this equation are:

- the characteristic length of the system, in our model the channel diameter d, equal to 5.7 *mm*;
- the Nusselt number Nu, calculated with Eq. 14, proposed by Nusselt (1931) valid for short tubes wherein the effect of the entrance region is not negligible. This formula is considered suitable within a range of $10<L/d<400$, where L represents the channel length. The model employed in our study has a L/D ratio of approximately 43, aligning with the conditions required by this formula;
- the thermal conductivity of water vapour k, determined with Eq. 15, where c_p is the specific heat capacity of water vapour at constant pressure, dependent on the flow temperature.

Reynolds number Re is calculated with Eq. 16. The density ρ is obtained from the gas perfect equation. The dynamic viscosity μ, determined with Eq. 17, provided by Crifo (1989) for low vapour temperatures, between 50 K and 300 K. The velocity V is obtained from Mach number measurements at the vent and speed of sound estimates. By considering only the velocity at the vent, an error is introduced and h_{conv} is overestimated. The Prandtl number Pr is considered equal to 0.7 for gases (Rapp, 2017).

$$Nu = 0.036 \cdot Re^{0.8} \cdot Pr^{1/3} \cdot \left(\frac{L}{d}\right)^{-0.054} \tag{14}$$

$$k = \frac{c_p \mu}{Pr} \tag{15}$$

$$Re = \frac{\rho L V}{\mu} \tag{16}$$

---

[2] The values of the Antoine equation parameters have been retrieved from the following NIST (National Institute of Standards and Technology) web page, making reference to *Bridgeman and Aldrich 1964*: `https://webbook.nist.gov/cgi/cbook.cgi?ID=C7732185&Mask=4&Type=ANTOINE&Plot=on`

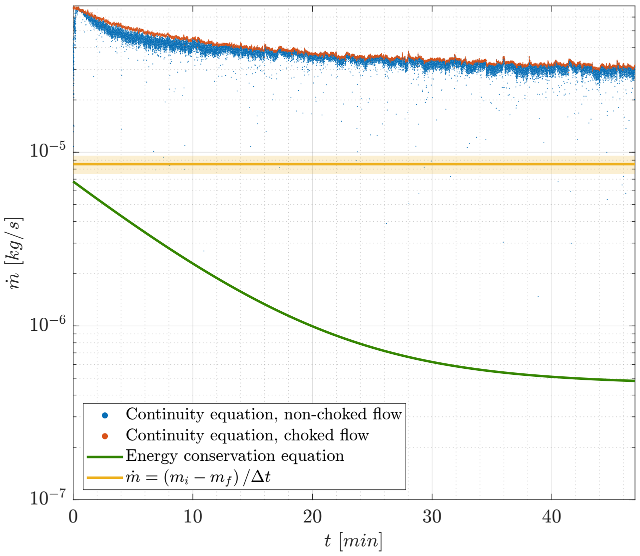

Figure 9: Mass flow rate in a frozen model experiment computed with Eq. 18 (blue), Eq. 19 (orange) and Eq. 20 (green). In yellow are indicated average mass flow rates computed from water mass loss in the reservoir at the end of the experiments. The observations span from the moment water starts boiling ($t = 0$ *min*) to the deactivation of the vacuum pumps ($t \sim 47$ *min*).

$$\mu = 0.925 \times 10^{-5} \left(\frac{T}{300}\right)^{1.1} \tag{17}$$

In the experiments, typical values of Re range around 1500±400 during the initial transitional phase and decrease to 550±400 as the flow approaches a stable state. These Reynolds numbers below 2000 indicate laminar flow. The heat transfer coefficient h_{conv} also decreases throughout the experiment, starting from 25-40 W/m^2K and stabilising at 15-20 W/m^2K, with an uncertainty of 8 W/m^2K.

C. Mass Flow Rate $\dot{m}_{flow}$

In this section, we apply 2 methods to calculate the mass flow rate calculation. The first way to compute $\dot{m}_{flow}$ is with Eq. 18, derived from the continuity equation. However, if the flow is choked, $\dot{m}_{flow}$ becomes independent of the vent conditions. In this case, Eq. 19 is used, dependent on the throat cross-section area A_{th}.

$$\dot{m} = \frac{AP_{res}}{\sqrt{R_{sp}T_{res}}} \sqrt{\frac{2\gamma}{\gamma - 1}\left(\frac{P_{vent}}{P_{res}}\right)^{\frac{2}{\gamma}}\left[1 - \left(\frac{P_{vent}}{P_{res}}\right)^{\frac{\gamma-1}{\gamma}}\right]} \tag{18}$$

$$\dot{m}_{cr} = \frac{A_{th}P_{res}}{\sqrt{R_{sp}T_{res}}}\sqrt{\gamma}\left(\frac{2}{\gamma+1}\right)^{\frac{\gamma+1}{2(\gamma-1)}} \tag{19}$$

The second method for determining the mass flow rate involves the principle of energy conservation, relating the change in water temperature in the reservoir to the energy absorbed by the vaporised water as expressed in Eq. 20.

$$\dot{m}_{flow} = \frac{\mathcal{P}_{\dot{T}}}{\Delta h} \tag{20}$$

The power $\mathcal{P}_{\dot{T}}$ subtracted from the water in the reservoir is calculated as follows:

$$\mathcal{P}_{\dot{T}} = -m_{water}c_p\dot{T} \tag{21}$$

where m_{water} is the mass of water in the reservoir, c_p is its specific heat and $\dot{T}$ is the temperature change rate. The latter is obtained by derivation of the function interpolating water temperature measurements. The initial value of m_{water} is measured before each experiment and is updated over time using Eq. 20.

One example, pertaining to a frozen model experiment, is reported in Fig. 9. Similar outcomes are obtained for warm model experiments, suggesting that $\dot{m}_{flow}$ is not governed by the wall temperature. We observe that non-choked and choked flow assumptions give approximately the same result. This corroborates the hypothesis of choked flow throughout the experiment. An almost constant mass flow rate is achieved towards the end of the experiment, due to the small change of reservoir and vent conditions with time.

To validate these estimates, the mass of water in the reservoir before and after the experiment has been weighted. Starting from an initial volume of 0.5 L, the reservoir lost on average 0.018-0.023 L of water (initial-final mass, $m_i - m_f$) for an average boiling duration of Δt=40 minutes. These measurements translate into an average mass flow rate of 7.5×10^{-6}-10^{-5} kg/s throughout the boiling phase (see Eq. 22).

$$\dot{m}_{flow} = \frac{m_i - m_f}{\Delta t} \tag{22}$$

Condensation was observed on the walls of the reservoir in all experiments, forming large droplets of water. This observation suggests that a portion of the vaporised mass is lost before entering the channel. Consequently, the principles of mass conservation, which underlie Eq. 18 and Eq. 19, no longer hold. The resulting value of $\dot{m}$ is expected to be smaller than what is estimated with these formulas.

Eq. 22 is also expected to overestimate the mass flow rate. First, the rate of evaporation is higher at the beginning of the experiment and reaches the lowest values when the flow achieves stable conditions. Furthermore, the water was weighed both before being placed into the reservoir prior to the experiment and after being removed from the reservoir at the experiment's conclusion. Some small water droplets were lost during these transfers, whether in the original container, within the reservoir, or along the channel. With these considerations, we can conclude that the mass flow rate is likely within $10^{-6} - 10^{-5}$ under stable flow conditions.

D. Wall-Flow Temperature Difference

Knowing the enthalpy excess at the vent (see Fig. 5) and considering convective and radiative heat transfer from the

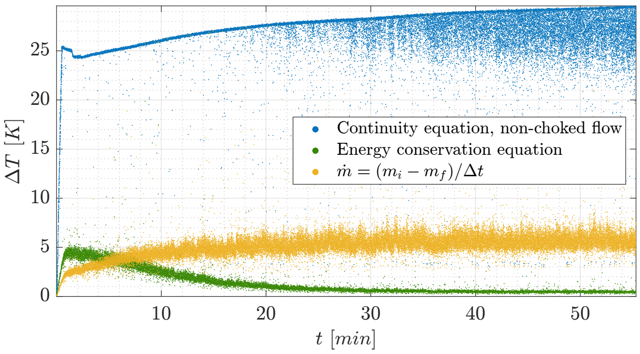

Figure 10: Temperature difference $T_{wall} - T_{flow}$ in the warm model computed from the enthalpy excess measured at the vent and assuming convective and radiative heat transfer with the channel walls as only processes affecting the flow temperature. The calculations have been performed with different mass flow rates, obtained from the continuity equation (Eq. 18, blue), the energy conservation (Eq. 20, green), and average mass loss measured at the end of the experiments (Eq. 22, yellow).

model as only processes affecting the flow temperature of the warm model, we solve Eq. 23 to find T_{wall}.

$$\Delta h_{vent}\dot{m}_{flow} = h_{conv}A\left(T_{wall} - T_{flow}\right) + \\ + \varepsilon\sigma A\left(T^4_{wall} - T^4_{flow}\right) \tag{23}$$

The following values have been assumed:

- $\dot{m}_{flow}$, calculated as detailed in Appendix C with the non-choked flow expression (Eq. 18), with the reservoir energy conservation (Eq. 20) and from observations of initial and final water mass in the reservoir (Eq. 22).
- h_{conv}, computed as in Appendix B, on average around 15-20 W/m^2K;
- A equal to $4.377 \times 10^{-3}\ m^2$ (diameter of 5.7 mm and channel length of 245 mm);
- ε (emissivity of PLA), assumed equal to 0.95;
- T_{flow}, assumed to be the average flow temperature among the four locations along the channel, with the understanding that minor temperature variations do not significantly impact the final outcome of $T_{wall} - T_{flow}$.

In Fig. 10, the solutions to Eq. 23 are presented for three distinct mass flow rates. The disparity between the results is due to the large difference in mass flow rates, with $\dot{m}_{flow}$ lower than 10^{-6} corresponding to $T_{wall} - T_{flow}$ below 1 K at the end of the experiment. On the other side, $\dot{m}_{flow} > 10^{-5}$ would require temperature differences as high as 25 K to motivate the high flow temperatures observed at the vent of the warm model. Since the mass flow rate estimated in Appendix C ranges between 10^{-6} to 10^{-5} kg/s, the temperature difference lays somewhere in between the 2 extremes displayed in Fig. 9, likely in the order of $10°C$.

It's important to note that these results do not directly reflect the actual temperature difference between the flow and the wall. Instead, they serve as an indication of the average temperature difference along the channel required to account for the observed Δh_{vent}. Therefore, the local temperature difference could assume values outside the estimated range.

5

Conclusions and Recommendations

The Cassini spacecraft's observations provided a wealth of data that significantly expanded our comprehension of Enceladus and its geological activity. The moon, though distantly orbiting Saturn, maintains a warm interior, despite its remote location from the Sun, that has given rise to the existence of a liquid ocean beneath its ice shell. Water from this ocean escapes through fractures in the moon's crust, resulting in the emergence of powerful jets known as *plumes*.

The central objective of this thesis project was to enhance our comprehension of the complex interactions between Enceladus' ocean, icy crust and plumes through an experimental approach. A laboratory setup was designed to simulate the conditions of Enceladus' icy moon plumes. This setup consisted of a water reservoir to replicate the subsurface ocean and a channel to mimic cracks in the icy crust. Temperature and pressure sensors were placed within the channel to measure the behaviour of water vapour flow.

The main research question was the following: *What is the influence of phase change and heat exchanges with the channel walls on the velocity of the plumes?* To answer this question, we designed a channel with a uniform cross-section area, excluding the influence of the channel geometry on the flow behaviour. The setup has been tested with 2 different wall temperatures: room temperature (warm model) and near 0°C (frozen model).

5.1 Conclusions

The main sub-questions of this research are here addressed:

1. *What is the impact of wall temperature on the flow temperature and velocity?* Wall temperature significantly impacts flow temperature due to convective and radiative heat transfer processes. In the warm model, a high-temperature flow was observed at the channel exit. In contrast, in the frozen model, the flow underwent cooling as it expanded within the channel, primarily due to reduced heating or, in certain instances, cooling induced by convection and thermal radiation with the walls.

2. *Is nucleation achieved in a straight channel?* A direct consequence of the high flow temperatures in the warm model is the absence of phase change, either through nucleation within the flow or via particle accretion on the channel walls. Conversely, the lower temperatures in the frozen model allowed the flow to approach saturation levels, as observed on Enceladus. During the experiments, the formation of ice clusters was observed on the inner surface of the channel, confirming the occurrence of phase change within the flow.

3. *Can supersonic velocities, similar to those observed by Cassini, be reached without the aid of a de Laval nozzle?* The frozen model consistently achieved higher velocities compared to the warm model, occasionally above the speed of sound, reaching speeds up to 500 m/s (Mach 1.25). In contrast, the warm model expelled water vapour at lower velocities, approximately between 300 and 400 m/s, and remained below Mach 1. This behaviour aligns with the Rayleigh flow theory, where the addition of heat to a supersonic flow results in flow choking, termed *thermal choking*, causing it to decelerate to subsonic speeds. Conversely, when heat is extracted from the flow, acceleration occurs.

Despite both the frozen and warm models achieving velocities consistent with some studies, the thermodynamic conditions within the experimental setup differed from those observed on Enceladus. Notably, the channel wall temperatures in our models ranged from 273-293 K, in contrast to the 140-220 K temperatures on Enceladus. An analysis based on the energy conservation law led to the formulation of a new plume model, referred to as *iso-enthalpy model*.

According to the iso-enthalpy model, the plume velocity can be increased by having a colder wall temperature, without a geometrical constriction choking the flow. However, as we reach a flow temperature around 210-235 K, the thermal velocity becomes smaller than the flow velocity, thus, inhibiting heat transfer with the wall. Therefore, the flow can not be further accelerated by decreasing T_{wall}. In contrast, the flow could potentially raise the temperature of a cooler wall.

The maximum velocity achievable through thermal choking inside a straight channel is estimated around 500-550 m/s (Mach 1.4) for a wall temperature of 210-235 K. Higher flow velocities and, consequently, lower temperatures are possible with a divergent channel section. With an expansion ratio of 1.5-2, we expect a plume to reach velocities up to 600-1000 m/s. These results suggest that warmer wall and flow temperatures are indicative of lower expansion ratios.

5.2 Recommendations for Future Investigations

To advance our comprehension of Enceladus' plumes, it is crucial to both develop a model that faithfully replicates the real conditions on the icy moon and improve the control and measuring equipment employed during the experiments.

- *Wall temperature*: it is advisable to replicate even lower model temperatures, thereby exploring whether the levels of enthalpy addition observed at the vent align with the observed range of 75-150 kJ/kg. Furthermore, the range of temperatures between 210-235 K should be tested to assess whether the flow velocity stabilises around the expected values (500-550 m/s).
- *Channel expansion ratio*: different expansion ratios should be tested to verify whether the same degree of enthalpy addition observed in the straight channel is replicated at the exit in different geometries. Testing several combinations of geometries and wall temperatures and comparing the outcomes with the iso-enthalpy model is advised to evaluate the model's reliability in diverse scenarios.
- *Channel length*: frozen model with longer channels should be tested. This investigation will help determine whether the level of enthalpy addition and alterations in solid fraction exhibit significant variations in response to extended channel length.
- *Initial conditions*: it is recommended to start the experiments with water at 0-3$°C$. The interpretability of the results would be improved, removing the initial dynamic phase where flow characteristics change with time, as well as the variable temperature difference between flow and channel walls.
- *Wall temperature measurement*: measuring the wall temperature during a plume experiment has proved to be challenging, given the temperature gradient along the channel and inside the *PLA* material. Possible methods to measure this variable should be investigated, providing more information on the heat exchanges between flow and walls.
- *Coefficients estimate*: latent heat of vaporization and sublimation (L_v), the specific heat capacity of water vapour (c_p), the thermal conductivity of water vapour (k), and other coefficients dependent on temperature and pressure should be better determined to improve the estimate on Reynolds, Prandtl and Nusselt number and, consequently, on the convective/radiative heat exchange and solid fraction.
- *Absolute pressure measurements*: small biases may have been introduced inferring the reservoir pressure on the water temperature through the Antoine equation. Moreover, there are no in-

dications of the pressure change without water at boiling conditions. Employing an absolute pressure sensor in the experimental setup would reduce these errors and give a more comprehensive understanding of the whole experimental procedure.

A

Laboratory Equipment and Data Processing

This chapter provides an overview of the key laboratory equipment and data processing techniques for our experiments. First, we describe the monitoring equipment, such as thermocouples and pressure sensors. The focus is then shifted to the control equipment. The vacuum chamber and vacuum pumps are essential in creating the necessary experimental conditions, specifically the low-pressure conditions characteristic of Enceladus' surface. Finally, we show the structure used to support the sensor for total pressure measurements.

A.1 Monitoring Equipment

In this section, the critical components of our monitoring equipment are described. Thermocouple measurements are analysed to account for both statistical noise and systematic bias. Following this, we explore the use of pressure sensors to monitor the pressure conditions inside the plume model. A schematic of the experimental setup is presented in Figure A.1 with indicated the locations where the sensors have been placed.

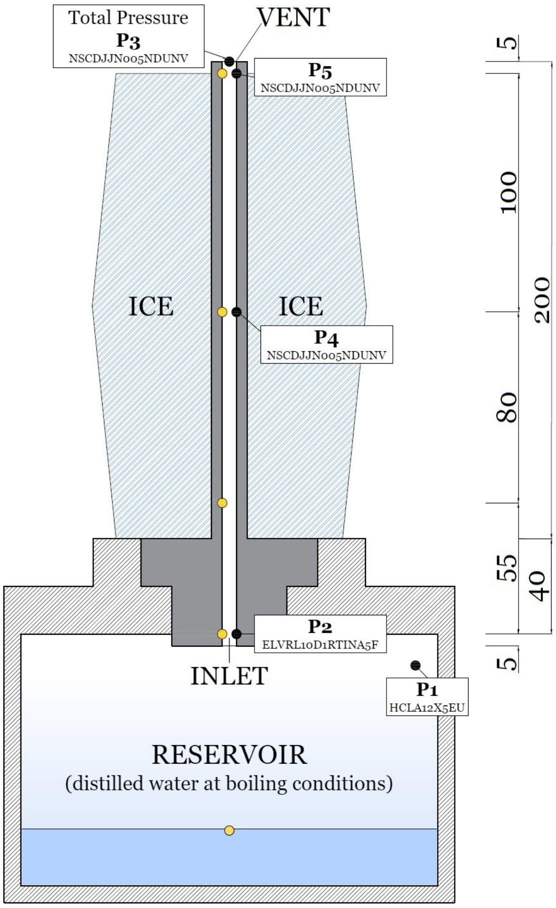

Figure A.1: Sketch of the experimental setup, consisting of a reservoir containing distilled water and a 245 mm channel with constant cross-section area. Thermocouples and pressure sensors location has been indicated with yellow and black dots respectively. The first 5 mm of the channel are defined as "inlet", while the last 5 mm are defined as "vent".

A.1.1 Thermocouples

Five T-type thermocouples were left overnight at approximately the same location in the non-evacuated test section of the vacuum chamber, sealed in order to avoid air currents and allow a uniform temperature distribution. Temperature has been measured in these conditions for 15 minutes, at a measuring rate of 50 Hz. Figure A.2 shows the acquired data points and the linear fit for each thermocouple measurement series.

The uncertainty of a temperature reading can be categorised into two types: the statistical noise, ΔT_{noise}, and the systematic bias, ΔT_{off}. The statistical noise is caused by the acquisition module and electronics. This error is approximated to 3 times the standard deviation of the measurements (σ_T) and is the same for all the thermocouples:

$$\Delta T_{noise} = 3\sigma_T \approx 0.24°C \tag{A.1}$$

The systematic bias, instead, is a constant offset in the measurements, given by the way the thermocou-

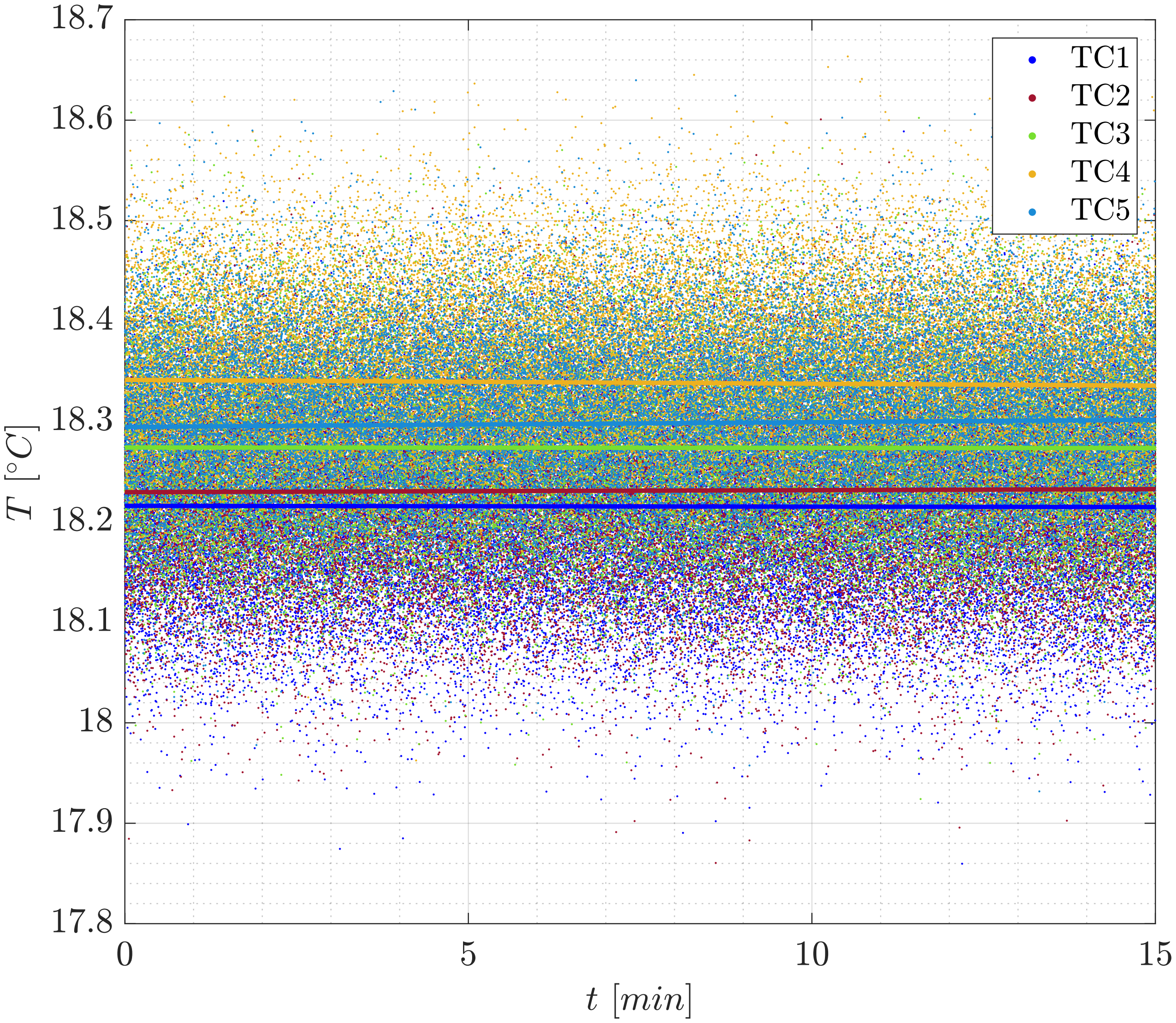

Figure A.2: Readings of five thermocouples (TC1, TC2, TC3, TC4, TC5) simultaneously measuring the temperature at approximately the same location inside the test section. The measuring rate is 50 *Hz*. The linear fits are created with the Least Squares method. Image created in *MATLAB*.

ple is manufactured. Characteristics like wire length, junction conformation and thermal shunting are considered sources of this error[1]. The linear fit in Figure A.2 suggests that the time dependency of the temperature measurements is negligible. Therefore, we consider the mean of the 5 values measured by the thermocouples as the "true" temperature. The associated uncertainty is considered as 3 times the standard deviation, calculated with Equation A.2. However, given the small sample size, the effective sample size (N^*) is used, accounting for the correlation between the series of data points. This value has been calculated with Equation A.3, with r being the 5×5 matrix of correlation coefficients obtained from the $5 \times N_{obs}$ matrix of measurements. The result is computed with Equation A.4, giving an average ΔT_{off} of 0.11°C.

$$\Delta T_{off} = 3\sigma_{true} \tag{A.2}$$

$$N^* = N\frac{1-r}{1+r} \tag{A.3}$$

$$\Delta T_{off} = 3\frac{\sigma_{true}}{\sqrt{N^*}} \approx 0.11°C \tag{A.4}$$

---

[1] For more information on the systematic error, make reference to the following error analysis: `https://www.osti.gov/servlets/purl/12104847`.

Combining the statistical noise and the systematic bias, we obtain an uncertainty around $0.27°C$, computed with Equation A.5. However, it should be noted that ΔT_{noise} can be neglected when averaging measurements taken in a time range much larger than the time step of acquisition.

$$\Delta T = \sqrt{\Delta T_{noise}^2 + \Delta T_{off}^2} \approx 0.27°C \tag{A.5}$$

In summary, the uncertainty on a limited number of temperature readings is considered equal to $0.27°C$, while averaging out the measurements leads to a higher measurement accuracy, with an uncertainty as low as $0.1°C$.

A.1.2 Differential Pressure Sensors

Differential pressure sensors are used to measure the difference in pressure between two ports, with the voltage output being directly proportional to this difference. In the plume experiments, the low-pressure port is exposed to the chamber pressure, while the high-pressure port is connected to the reservoir or the channel where the gas is flowing. To convert the measured voltage output (V_{out}) into differential pressure (P_{diff}), Sklavenitis (2022) used the following formula to convert the measured voltage V_{out} into differential pressure P_{diff}:

$$P_{diff} = P_{diff,max}\,\frac{V_{out} - V_{off}}{V_{max} - V_{off}} \quad [mbar] \tag{A.6}$$

where $P_{diff_{max}}$ is the maximum differential pressure measurable with the sensor, V_{off} is the voltage output when the ports are exposed to the same pressure, and V_{max} is the voltage output when the ports are exposed to the maximum differential pressure measurable with the sensor.

However, for more accurate results, it is important to consider the actual voltage output of the power supply used during the experiments ($V_{supply,real}$), which may differ from the ideal voltage output measured by the manufacturer ($V_{supply,ideal}$). This factor can have an impact on the maximum voltage attainable during an experiment. Accordingly, Verhoeff (2023) introduced the following formula:

$$P_{diff} = P_{diff,max}\,\frac{V_{out} - V_{off}}{V_{max,ideal}\frac{V_{supply,real}}{V_{supply,ideal}} - V_{off}} \quad [mbar] \tag{A.7}$$

Sensors specifications are summarised in Table A.1. While $V_{supply,ideal}$ and $V_{max,ideal}$ are provided for the sensors `HCLA12X5EU` and `ELVRL10D1RTINA5F` ($V_{supply,ideal}$=4.25 V and $V_{max,ideal}$=5 V), they are unknown for `NSCDJJN005NDUNV` sensors. We experimentally compute the value of α, defined as in Equation A.8, for each of these sensors. In order to do so, we induce the same pressure difference in the high-pressure ports of each sensor and record the output voltages. From the `HCLA12X5EU` and `ELVRL10D1RTINA5F` sensors output, we calculate the induced differential pressure using Equation A.7. Substituting this value in Equation A.8, we find the missing ratio for the other 3 sensors, reported in Table A.1.

$$\alpha = \frac{V_{max,ideal}}{V_{supply,ideal}} = \frac{P_{diff,max}\,(V_{out} - V_{off}) + P_{diff}V_{off}}{P_{diff}V_{supply,real}} \tag{A.8}$$

The pressure uncertainty $\sigma_{p,diff}$ is calculated for each sensor. To obtain this value, we propagate the errors on each variable in Equation A.7 with Equation A.9.

$$\sigma_{p,diff} = \sqrt{\left(\frac{\partial P_{diff}}{\partial V_{out}}\sigma_{V,out}\right)^2 + \left(\frac{\partial P_{diff}}{\partial V_{off}}\sigma_{V,off}\right)^2 + \left(\frac{\partial P_{diff}}{\partial V_{supply,real}}\sigma_{V,supply,real}\right)^2} \tag{A.9}$$

$$\frac{\partial P_{diff}}{\partial V_{out}} = P_{diff,max}\frac{1}{\alpha V_{supply,real} - V_{off}} \tag{A.10}$$

$$\frac{\partial P_{diff}}{\partial V_{off}} = P_{diff,max}\frac{V_{out} - \alpha V_{supply,real}}{(\alpha V_{supply,real} - V_{off})^2} \tag{A.11}$$

	Brand	Model name	$P_{diff,max}$	α $[-]$	$\sigma_{P,diff}$	$\sigma^*_{P,diff}$
1	*First Sensor*	`HCLA12X5EU`[2]	12.5 $mbar$	0.85	$\pm$0.3 $mbar$	-
2	*All Sensors*	`ELVRL10D1RTINA5F`[3]	25 $mbar$		$\pm$1 $mbar$	-
3	*Honeywell*	`NSCDJJN005NDUNV`[4]	12.5 $mbar$	0.5071*	$\pm$20 $mbar$	$\pm$0.6* $mbar$
4				0.5082*	$\pm$20 $mbar$	$\pm$0.6* $mbar$
5				0.5088*	$\pm$20 $mbar$	$\pm$0.6* $mbar$

*determined experimentally

Table A.1: Summary of sensors specifications useful for this study. The sensors have been numbered from 1 to 5. The uncertainty $\sigma_{P,diff}$ was determined by error propagation with Equation A.9. A better estimate ($\sigma^*_{P,diff}$) is determined experimentally for the *Honeywell* sensors.

$$\frac{\partial P_{diff}}{\partial V_{supply,real}} = -P_{diff,max} \frac{\alpha \left(V_{out} - V_{off}\right)}{\left(\alpha V_{supply,real} - V_{off}\right)^2} \tag{A.12}$$

According to the datasheets, V_{off} is not constant. It can be shifted due to warm-up during the first hour after being turned on, to gravity depending on the sensor's orientation, and to long-term drift (material degradation). These shifts can be integrated into the calculation of the offset uncertainty. However, we can ignore these contributions by computing the value of V_{off} before each experiment, after letting the sensor warm up for one hour. The output voltage is logged for 1 minute with the sensor at rest. A constant value is fitted by using the method of the Least Squares. The covariance of the obtained constant value is its uncertainty ($\sigma_{V,off}$), typically lower than 1.3×10^{-5} V. The same is done for $V_{supply,real}$, obtaining a value of $\sigma_{V,supply,real}$ around 3×10^{-5} V.

The output voltage uncertainty $\sigma_{V,out}$ is given by the `HCLA12X5EU` and `ELVRL10D1RTINA5F` sensors datasheets, equal in both cases to 0.1 V. The $\sigma_{V,out}$ associated with the `NSCDJJN005NDUNV` sensors, instead, is not given in absolute value, but in relation to the supply voltage: $\sigma_{V,out}/V_{supply,real} = \pm 21$ mV/V. Therefore, for an average supply voltage of 5.18 V, the $\sigma_{V,out}$ of these sensors is approximately 0.1124 V. As indicated in the sensor's datasheet, the typical uncertainty in the output voltage (Vout) resulting from non-linearity and hysteresis is as high as 0.25% of the Full Scale Span of the sensor ($FSS = V_{max} - V_{off}$). This contribution is around 0.01 V for the *First Sensor* and *All Sensors*'s probes and 0.002 V for the *Honeywell*'s sensors. These contributions have been accounted for in $\sigma_{V,out}$.

The result of error propagation is shown in Table A.1. An uncertainty within 0.3 $mbar$ is obtained for the `HCLA12X5EU` sensor. The `ELVRL10D1RTINA5F` sensor has an uncertainty of 1 $mbar$. The `NSCDJJN005NDUNV` sensors produce the highest $\sigma_{p,diff}$, around 20 $mbar$. The elevated inaccuracies in the latter sensors are likely attributed to an inappropriate supply voltage and operational range of pressures. The sensor datasheet indicates a working pressure of 150 H_2O, which converted is around 373 $mbar$, significantly higher than the operational pressure during a plume experiment, in the order of a few $mbar$.

Although the uncertainty calculations initially indicated that the *Honeywell* sensors might not provide useful information in our experimental setup, the measurements demonstrated a higher level of precision. To assess the reliability of these sensors, each sensor was exposed to identical pressure conditions, and their output pressures were compared to the readings from the most accurate sensor (**P1**, see Figure A.1), the `HCLA12X5EU` from *First Sensor*. All sensors consistently measured similar pressures. Notably, the *Honeywell* sensors consistently provided pressure readings within 0.5 $mbar$ of the `HCLA12X5EU` sensor measurements. Consequently, the uncertainty used in this study is determined to be the combination of the reference pressure uncertainty (σ_{P1}=0.3 $mbar$) and the 0.5 $mbar$ derived from this analysis. The result, approximately 0.6 $mbar$, is reported in Table A.1. Given

---

[2] `https://www.first-sensor.com/cms/upload/datasheets/DS_Standard-HCLA_E_11629.pdf` (last visit 21/09/2023)

[3] `https://nl.mouser.com/datasheet/2/18/1/DS-0375_Rev_A-1499152.pdf` (last visit 21/09/2023)

[4] `https://nl.mouser.com/datasheet/2/187/HWSC_S_A0012826331_1-3073283.pdf` (last visit 21/09/2023)

that all experiments were conducted with the same setup over a relatively brief period and followed similar procedures, we make the assumption that the sensor's behaviour remained consistent across all experiments. Consequently, we apply the determined uncertainties to all the collected data.

A.1.3 Absolute Pressure Measurements

The pressure inside the vacuum chamber is generally monitored with the `THERMOVAC TR 211` pressure sensor by *Leybold*, measuring pressures between $5{\times}10^{-4}$ and 1000 *mbar* according to the company's website[5]. The voltage values are converted in pressure with the following equation[6]:

$$P_{ch} = 10^{0.6\cdot V_{vac}-3} \tag{A.13}$$

However, due to a defect in the `THERMOVAC TR 211` pressure sensor, the pressure measurements resulted to be faulty when the pressure inside the chamber was above 3 *mbar*. Eventually, the sensor started malfunctioning at pressures lower than this limit too, leading us to an alternative way of measuring this parameter.

Prior experiments conducted by Sklavenitis (2022) revealed that the reservoir conditions remained relatively stable, closely following the saturation curve during the boiling phase of their experiments (see Figure A.3). This insight guided the selection of the reference pressure employed in this study, which was calculated using the Antoine equation (see Equation 3.1) while water was undergoing the boiling process. Consequently, reliable pressure measurements were attainable only during the period when the water vapour inside the reservoir had reached a saturated state, hence when water was actively boiling. The pressure in the reservoir was assumed equal to the saturated water vapour pressure ($p_{s.v.}$), directly correlated to the water temperature (T_{water}). The values of the Antoine equation parameters A, B and C have been assumed equal to 5.40221, 1838.675 and -31.737 respectively[7], giving $p_{s.v.}$ values in *bar*.

$$\log p_{s.v.} = A - \frac{B}{C+T} \tag{3.1}$$

We compare the pressure-temperature conditions of the flow measured at the vent in the warm model experiments (see Journal Article: Figure 2) with those measured by Sklavenitis (2022) (see Figure A.4). Despite the different channel geometry, our experimental results are in reasonable agreement with the findings of Sklavenitis (2022), meaning that the procedure described above can provide reliable pressure indications.

The uncertainty in the reservoir pressure ($\sigma_{p,res}$), measured in *mbar*, is calculated using Equation A.14. The temperature uncertainty ($\sigma_{T,water}$) is assumed to be $0.27°C$, as discussed in subsection A.1.1. Because the result is dependent on the water temperature (T_{water}), the uncertainty ranges from 0.26 to 0.4 *mbar* at the start of the experiment. As the water approaches its freezing point, this uncertainty decreases to values below 0.15 *mbar*.

$$\begin{aligned}\sigma_{p,res} &= \frac{\partial p_{s.v.}}{\partial T_{water}}\sigma_{T,water} \times 10^3 \\ &= 10^{\left(A-\frac{B}{C+T_{water}}\right)} \log(10)\ \frac{B}{(C+T_{water})^2}\ \sigma_{T,water} \times 10^3\end{aligned} \tag{A.14}$$

---

[5] `https://www.leyboldproducts.nl/en/products/measuring-and-analysis-instruments/pressure-measurement/passive-sensors/thermovac-sensors/1824/thermovac-tr-211?number=15785`, last visit: 31/03/2023.

[6] `http://www.hvg-verwertung.de/ebay/dokumentation/leybold/Messtechnik/TM20_PV20.pdf`, last visit: 03/04/2023.

[7] Retrieved from the NIST (National Institute of Standards and Technology) web page, making reference to Bridgeman et al. (1964).

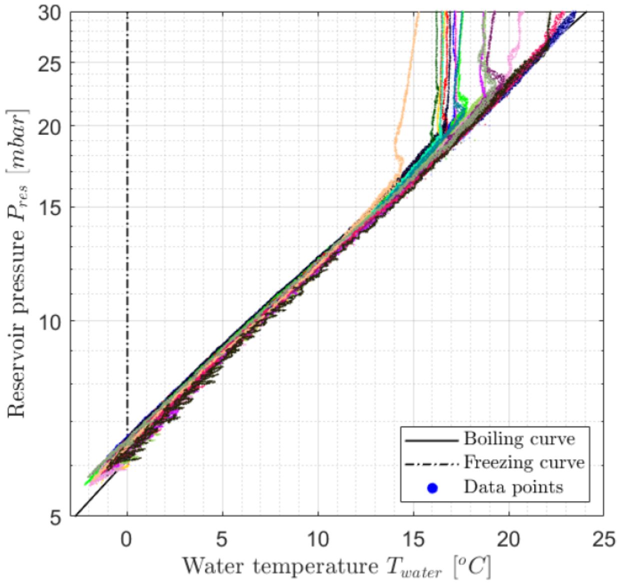

Figure A.3: Pressure-temperature conditions measured in the reservoir for 20 different plume experiments. Image retrieved from Sklavenitis (2022).

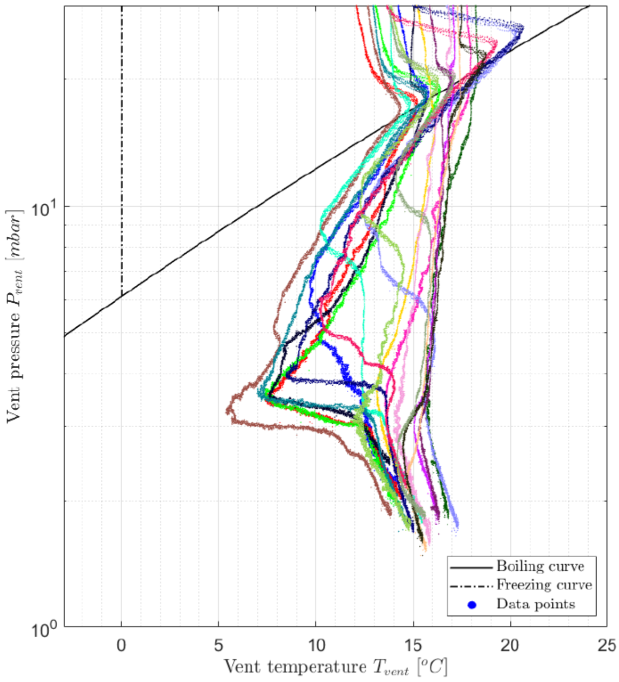

Figure A.4: Pressure-temperature conditions measured at the vent of the channel for 20 different plume experiments. Image retrieved from Sklavenitis (2022).

The pressure acquired using the differential pressure sensors combines the uncertainties associated with the reservoir pressure and those related to the sensors themselves. The vacuum chamber pressure is determined with the first sensor (**P1**), yielding an uncertainty $\sigma_{p,ch}$ below 0.5 $mbar$, calculated with Equation A.15. In the best-case scenario, with $\sigma_{p,res} = 0.15\ mbar$, the $\sigma_{p,ch}$ decreases to approximately 0.35 $mbar$. The low-pressure ports of the other sensors (**P2**, **P3**, **P4** and **P5**), located along the channel as represented in Figure A.1, were exposed to the vacuum chamber environment. Consequently, their total uncertainty ($\sigma_{p,2-5}$) is determined using the uncertainty associated with the vacuum chamber pressure, as shown in Equation A.16, resulting in values around 0.7 $mbar$.

$$\sigma_{p,ch} = \sqrt{\sigma_{p,res}^2 + \sigma_{p,diff,1}^2} \tag{A.15}$$

$$\sigma_{p,2-5} = \sqrt{\sigma_{p,ch}^2 + \sigma_{p,diff,2-5}^2} \tag{A.16}$$

A.2 Control Equipment: Vacuum Chamber and Vacuum Pumps

The test section of the *Hypersonic Test Facility Delft* (HTFD) vacuum chamber has been used to perform the experiments. David et al. (2006) provides descriptions and drawings of the entire HTFD setup.

We measured the temperature in different locations inside the test section of the vacuum chamber, exhibiting a slight increase from the bottom to the top, with a maximum difference measured around 1°C. These higher temperatures are attributed to thermal radiation coming from the chamber windows and heating the gas inside. Warmer air is less dense and tends to rise. This temperature difference is low enough to be neglected as a possible process involved in the experiments.

A typical plume experiment procedure consists of evacuating the vacuum chamber until the water in the reservoir freezes after reaching triple point conditions or, alternatively, when stable flow conditions are observed with time. The vacuum chamber is then re-pressurised. An evacuation/re-pressurisation cycle can be divided into the following phases.

1. **Atmospheric Pressure**: at the beginning of the experiment, the chamber is at atmospheric pressure. Readings from 4 thermocouples are averaged and reported in Figure A.5 (orange data points), showing a temperature between 18°C and 20°C. The pressure measurements were performed when the `THERMOVAC TR 211` pressure sensor was producing faulty measurements at only high pressures, above 3 *mbar*.
2. **Evacuation**: after around 1 minute, the pumps are activated and the evacuation starts. Temperature drops, indicating an expansion of the gas. As the chamber is rapidly evacuated, the remaining gas undergoes a quasi-adiabatic expansion, which lasts for a few tens of seconds. After about 1 minute, the pressure decreases at a slower rate and the gas does not expand adiabatically anymore.
3. **Thermal Adaptation**: as the pumps keep operating, the pressure in the chamber decreases to roughly 1 *mbar*. The temperature increases and typically returns to its original level within 5 to 10 minutes. One of the main reasons for this rise in gas temperature is likely convective and radiative heat transfer with the vacuum chamber walls. Since the latter are at room temperature, they act as a thermostat and provide heat to the test section environment.
4. **Re-pressurisation**: at approximately 52-53 minutes from the start of the experiment, the vacuum pumps are turned off and the chamber is pressurised again to atmospheric pressure. This process creates a flow of air in the chamber. Similar to what happened during the evacuation, the air rapidly flows inside the chamber and undergoes a compression which is quasi-adiabatic in the first few tens of seconds. This leads to a sudden rise in temperatures, on average 30-35°C. Thermal adaptation follows, slowly bringing the gas back to room temperature. In Figure A.5, a minor temperature peak is visible at approximately 58-59 minutes from the start of the experiment, coincident with the conclusion of the re-pressurisation phase. This peak is likely a consequence of uncontrolled airflow into the chamber during the final seconds of re-pressurisation.

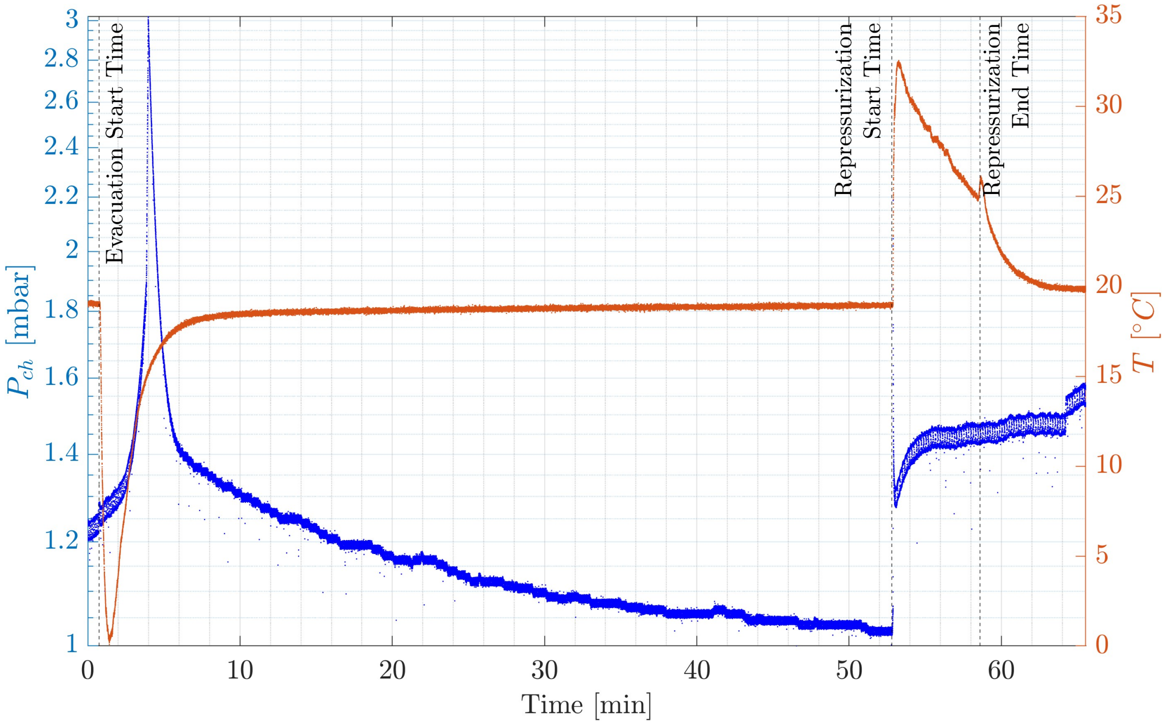

Figure A.5: Pressure, measured with `THERMOVAC TR 211`, and temperature, obtained from averaging 5 T-type thermocouples readings, inside the test section during an evacuation/re-pressurisation cycle. The pressure sensor was producing faulty readings for pressures above 3 *mbar*. Hence, only pressure data between 5 and 52 minutes should be considered. Image created in *MATLAB*.

To test the efficiency of the pumps, we measure the pressure inside the test section during two evacuation/re-pressurisation cycles: the first one with cold pumps, hence as the first cycle of the

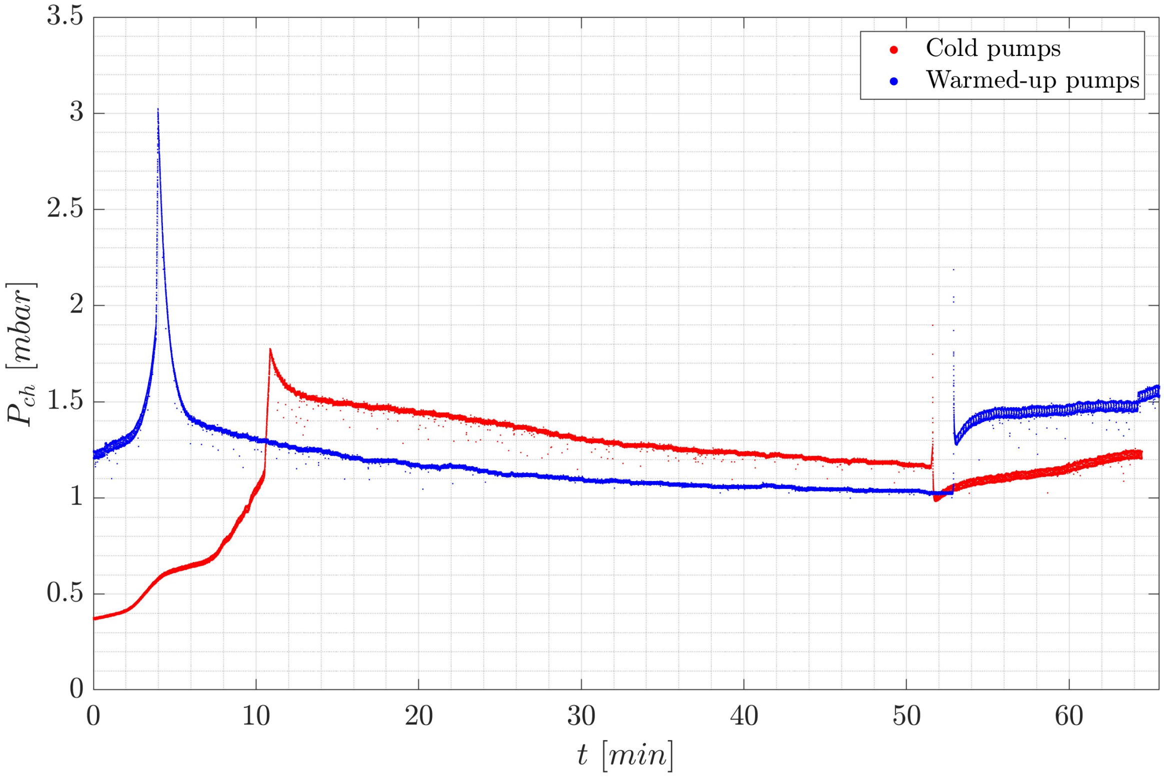

Figure A.6: Readings of `THERMOVAC TR 211` pressure sensor, measuring the pressure inside the vacuum chamber during two evacuation/re-pressurisation cycles: with cold pumps, as the first cycle of the day, and with warmed-up pumps. The pressure sensor was producing faulty readings for pressures above 3 *mbar*. Hence, only pressure data between 12 and 50 minutes for the cold pumps and between 5 and 52 minutes for the warmed-up pumps should be considered. Image created in *MATLAB*.

day; the second one with warmed-up pumps. Figure A.6 shows the differences between the two cycles. Again, only measurements within the indicated time range should be considered. The warmed-up pumps are clearly more efficient, de-pressurising the chamber to 1.2 mbar in about 15-20 minutes, against the 40-50 minutes of the cold pumps, and reaching a lower pressure level.

A.3 Pitot Tube Support

Total pressure measurements were obtained at the channel's vent using a differential pressure sensor, which required proper alignment with the channel's central axis for reliable data collection. To achieve this alignment, the high-pressure port of the sensor was connected to a metal tube supported by a structure located above the plume model.

Figure A.7 shows a picture of the support. It consists of a hollow cylindrical base, which was 3D printed using polylactic acid (*PLA*), and four metal rods supporting two disks. These disks, also 3D printed from the same material, have a 1.8-*mm* diameter hole designed to accommodate the metal tube used for total pressure measurements. This structure ensured precise alignment of the tube with the channel's axis, reducing measurement errors and preventing unintentional movements of the tube during the experiments.

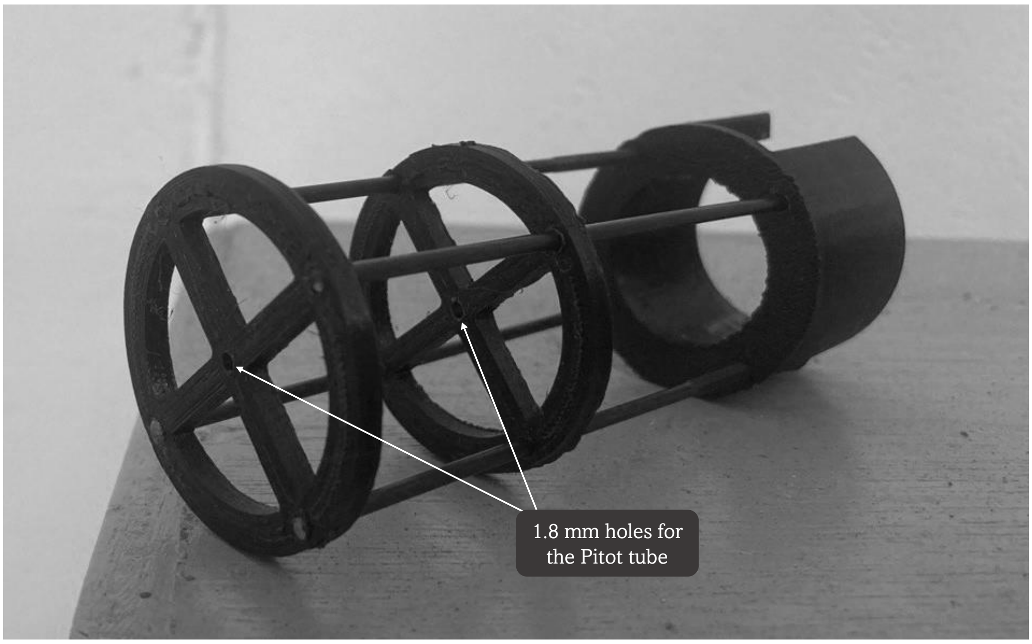

Figure A.7: Picture of the Pitot tube support. The 1.8-mm diameter holes allow a precise alignment of the tube with the axis of the channel, reducing the errors in the measurements and involuntary movements of the tube during the experiments.

B

Verification and Validation

Sklavenitis (2022) and Verhoeff (2023) have determined that the flow within experimental plume models does not adhere to isentropic conditions, with temperature profiles increasing towards the exit of the channel. Moreover, the flow is found to be far from saturation conditions, contrary to the expectations based on the behaviour of Enceladus' plumes. The authors have hypothesised that the reason for this discrepancy could be due to a faulty temperature reading of a water vapour flow, caused by turbulence around the thermocouples tip.

In the upcoming sections, we verify the validity of thermocouple measurements in our plume models. First, we analyse the models in static conditions, meaning when there is no airflow. In section B.1, we observe the effect of a surface with a large temperature difference with the vacuum chamber environment on the thermocouple measurements. Section B.2 provides a comprehensive description of how heat transfer has been computed for natural convection at atmospheric pressure and in vacuum, and for a water vapour flow inside a constant area channel, concluding that convective and radiative heat transfer accounts for most of the heat exchanged in static conditions.

Afterwards, we analyse the models with a gas flow travelling across the channel. The temperature measurements when the thermocouples are exposed to the plume flow and the influence of the wall temperature on the same thermocouple are assessed in section B.3. Comparisons with findings from prior studies are presented in section B.4, showing that temperature measurements are highly dependent on the wall temperature. Moreover, changes in model temperature suggest that heat transfer between flow and model is non-negligible. In section B.5, we provide additional evidence of non-isentropic conditions in the plume models, corroborating the hypothesis of the high influence of heat transfer within the model.

B.1 Temperature dependency on Distance

The temperature has been measured at different distances from an object with temperature $T_{obj} \simeq 5.5°C$ at atmospheric pressure. The data points have been interpolated as in Figure B.1. The presence of the cold object is noticeable within a distance of 5 cm from it. The temperature approaches asymptotically a value around $18.1°C$, which can be considered equal to the air temperature, or environment temperature of the vacuum chamber. These measurements align with the model proposed by Yuningsih et al. (2021), stating that measurements remain nearly constant beyond a distance of 10 cm due to the dominant influence of the surrounding environment. Furthermore, the study indicates that the fourth power of temperatures is inversely proportional to the square of the distance from the heat source, as confirmed by the data presented in Figure B.2.

As a second step, we placed the thermocouples inside the *frozen model*, described in Journal Article: Section 2. The readings did not show a noticeable variation when the tip of the thermocouple was placed at different distances and reported a temperature between -5 and $0°C$. We can conclude that the diameter of the channel is not large enough to generate a temperature gradient in static conditions and the measured temperature corresponds to the model temperature.

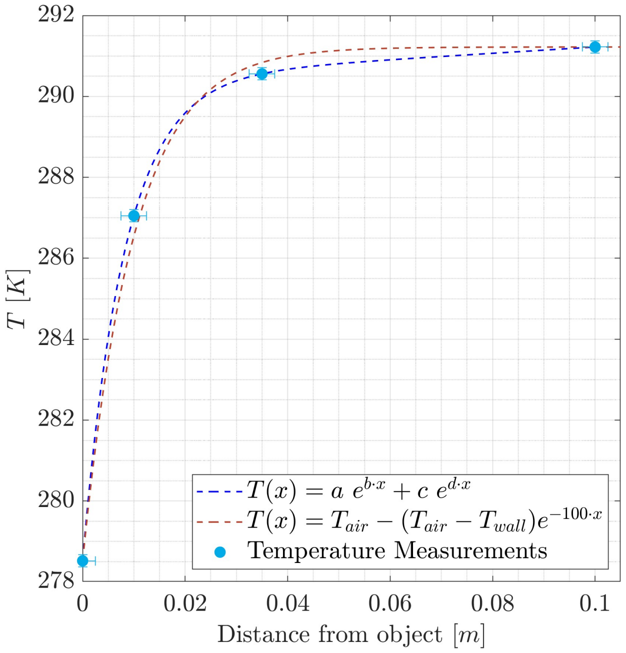

Figure B.1: Temperature variation with distance from an object with temperature around 5.5°C. Temperature has been measured with 4 thermocouples placed at different distances from the object. The 2 interpolating curves have been reported in the legend: temperatures are expressed in kelvin and distances x are expressed in meters. The coefficients a, b, c and d, associated with the double exponential interpolation, are estimated around 290.4, 0.02665, -11.93, and -123.3 respectively. Image created in *MATLAB*.

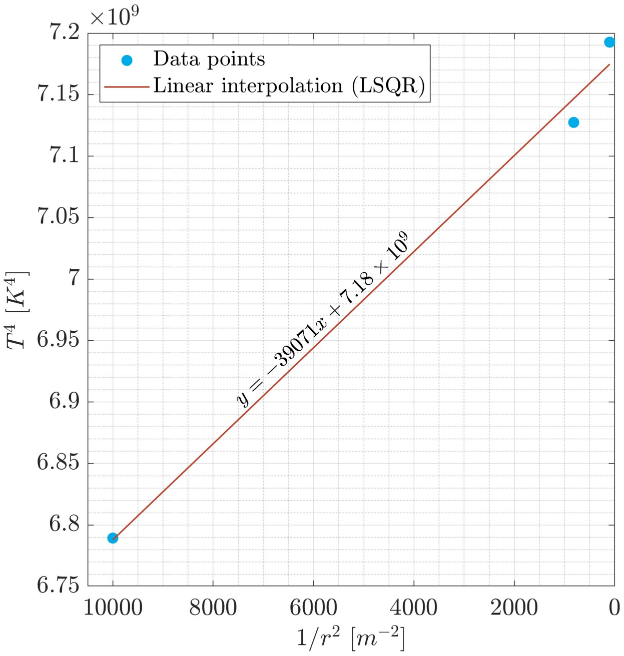

Figure B.2: Linear regression analysis (Least Square Method) on the temperature reading at a distance of 1, 3.5 and 10 *cm*. The fourth power of temperatures ($y = T^4$) is inversely proportional to the square of the distance of that point to the heat source ($x = 1/r^2$). The function of the interpolated line indicates an inclination in the order of 10^4, in agreement with Yuningsih et al. (2021). Image created in *MATLAB*.

B.2 Heat Transfer Coefficients h_{conv}

In the following paragraphs, the heat transfer coefficient has been computed for natural convection at atmospheric pressure (subsection B.2.1) and in vacuum (subsection B.2.2). Finally, we show the h_{conv} computed for a water vapour flow inside a constant area channel (subsection B.2.3).

B.2.1 Estimate of h_{conv} at Atmospheric Pressure

The model was cooled down by a few degrees and placed inside the sealed non-evacuated vacuum chamber. The thermocouples were placed in different locations. To measure the model temperature, 3 thermocouples were placed inside the channel, measuring the temperature of the air inside the channel at 3 different heights. As found in section B.1, a thermocouple a few millimetres away from an object colder than the environment measured a higher temperature compared to T_{obj}. However, if the thermocouple was surrounded by the channel with no airflow, the model and the air in the channel quickly reached thermal equilibrium. Thus, we assume that these measurements correspond to the wall temperature of the model. The remaining 2 thermocouples measured the air temperature inside the chamber at 2 different heights: one at the bottom and one at the top of the vacuum chamber, aligned with the base and the vent of the model respectively.

Figure B.3 shows the average model and air temperature measurements, in cyan and green respectively. The theoretical evolution of the temperature model assuming 2 different values of h_{conv} (see Table 3.1) is indicated with orange lines. Observations and theory agree, suggesting that our simple theoretical model well represents the real heat exchanges, with convection and thermal radiation dominating over

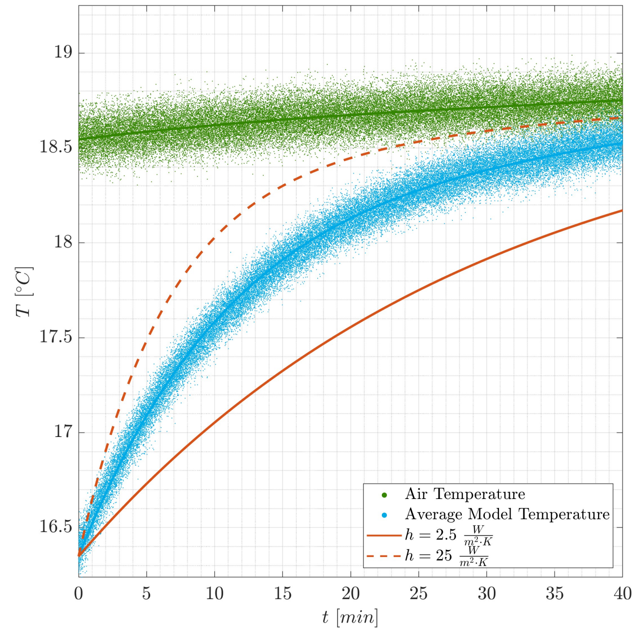

Figure B.3: Observed and simulated temperature evolution of the model inside the sealed, non-evacuated vacuum chamber in order to estimate h_{conv} for natural convection. The theoretical model assumes only heat transfer through natural convection and thermal radiation. The theoretical temperatures (orange lines) have been propagated from the initial observed model temperature (cyan line at t=0 minutes). The air temperature in Equation B.2 has been set equal to the measured air temperature (green). Image created in *MATLAB*.

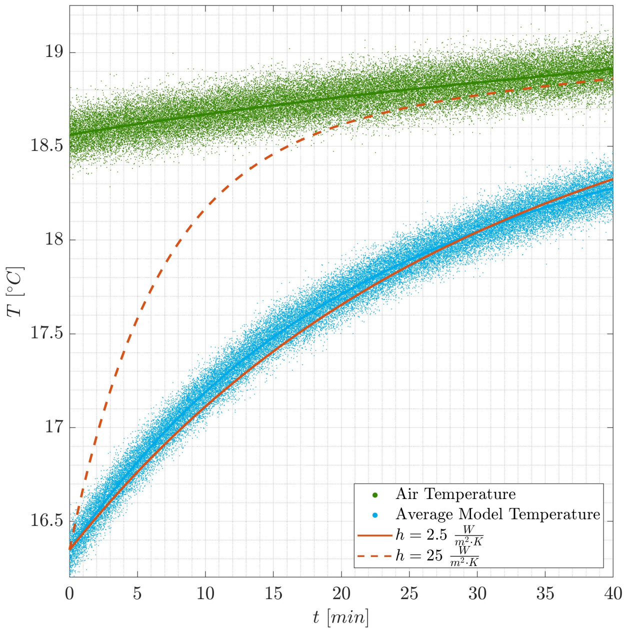

Figure B.4: Observed and simulated temperature evolution of the model inside the sealed, *evacuated* vacuum chamber in order to estimate h_{conv} for natural convection. The data (cyan and green) have been acquired after the environment inside the chamber has reached thermal equilibrium with the vacuum chamber walls (see section A.2). This prevents air flows (forced convection) generated during evacuation to interfere with the estimation of the coefficient. The pressure inside the chamber was around 1-1.8 *mbar* throughout the duration of the experiment. Image created in *MATLAB*.

other heat transfer processes. The simulation suggests that h_{conv} assumes a value between 2.5 and 25 W/m^2K inside the sealed, non-evacuated vacuum chamber, in agreement with Kosky et al. (2013). A better estimate of h_{conv} is computed using Equation B.2, obtaining values between 5.95 and 10.27 W/m^2K throughout the measurement period.

$$h_{conv} A \left(T_{air} - T_{model}\right) + \varepsilon \sigma A \left(T_{air}^4 - T_{model}^4\right) = m c_p \frac{dT_{model}}{dt} \tag{B.1}$$

$$h_{conv} = \frac{m c_p \frac{dT_{model}}{dt} - \varepsilon \sigma A \left(T_{air}^4 - T_{model}^4\right)}{A \left(T_{air} - T_{model}\right)} \tag{B.2}$$

B.2.2 Estimate of h_{conv} in Vacuum

Thermal radiation emitted or absorbed by an object depends on its surface, emissivity, temperature and the temperature of the surroundings (see Equation 3.8). None of these variables directly depends on the pressure (Saidi et al., 2010). Convection, on the other side, is highly dependent on the fluid properties and, therefore, on its density/pressure. The heat transfer coefficient of natural convection for air (h_{air}) is seen to decrease considerably with pressure in laboratory experiments conducted by Saidi et al. (2010).

We repeat the experiment performed in subsection B.2.1, but in vacuum conditions. The model is cooled and the chamber is evacuated. Thermocouples have been placed in the same configuration pre-

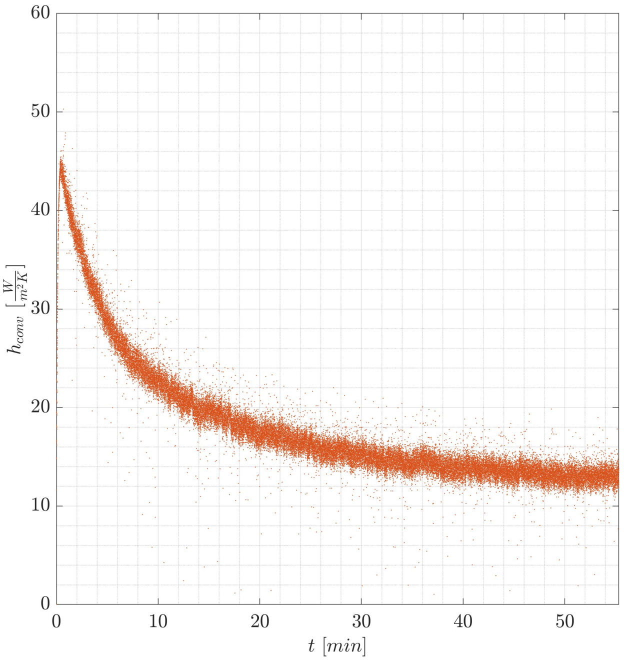

Figure B.5: Heat transfer coefficient h_{conv} of the water vapour flow inside a constant cross-section area channel with diameter 5.7 mm at room temperature (*warm model*). Image created in *MATLAB*.

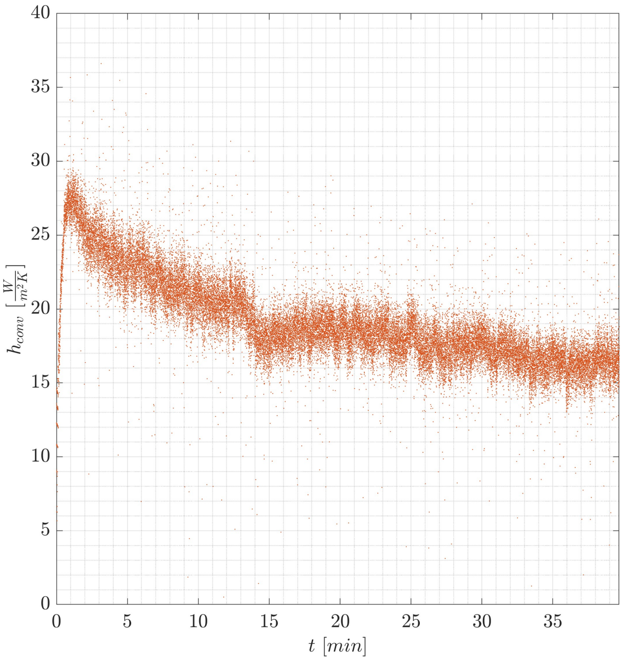

Figure B.6: Heat transfer coefficient h_{conv} of the water vapour flow inside a constant cross-section area channel with diameter 5.7 mm at a temperature between -5 and 0°C (*frozen model*). Image created in *MATLAB*.

sented in the previous section and the temperature readings are averaged with the same methodology. To prevent transitional temperature disturbances caused by the evacuation process, the temperature measurements started 10 minutes after the activation of the pumps. The pressure could not be measured due to the malfunctioning of the sensor gauging the pressure in the chamber. However, from previous experiments, we can safely state that the pressure ranged between 1 and 1.8 $mbar$ after 10 minutes of evacuation.

The results are plotted in Figure B.4. Compared to the previous case, the temperature increases more slowly, meaning that h_{conv} is lower for lower pressures. The temperature curve almost coincides with the theoretical lower limit (h_{conv}=2.5 W/m^2K), with Equation B.2 returning an average value of 2.14 W/m^2K.

B.2.3 Estimate of h_{conv} in a Water Vapour Flow

Figure B.5 and Figure B.6 show the typical h_{conv} for a warm model and a frozen model experiment, calculated with the procedure detailed in Journal Article: Appendix B. The average convective heat transfer at stable conditions is approximately 15±8 W/m^2K

B.3 Thermocouple Reliability

The pressure-temperature conditions outlined in Journal Article: Section 3.1 indicate that the frozen model consistently generates a saturated flow throughout the experiment duration. Since this is the expected condition in an Enceladus plume, we can infer that the temperature measurements reasonably represent the actual flow temperature. In this section, we provide a detailed analysis to assess the reliability of the thermocouples when measuring the temperature of a flow at relatively high velocities.

To evaluate the sensitivity of temperature measurements to the geometric configuration of the thermocouple tips, we positioned three thermocouples at the same location along the channel, each with

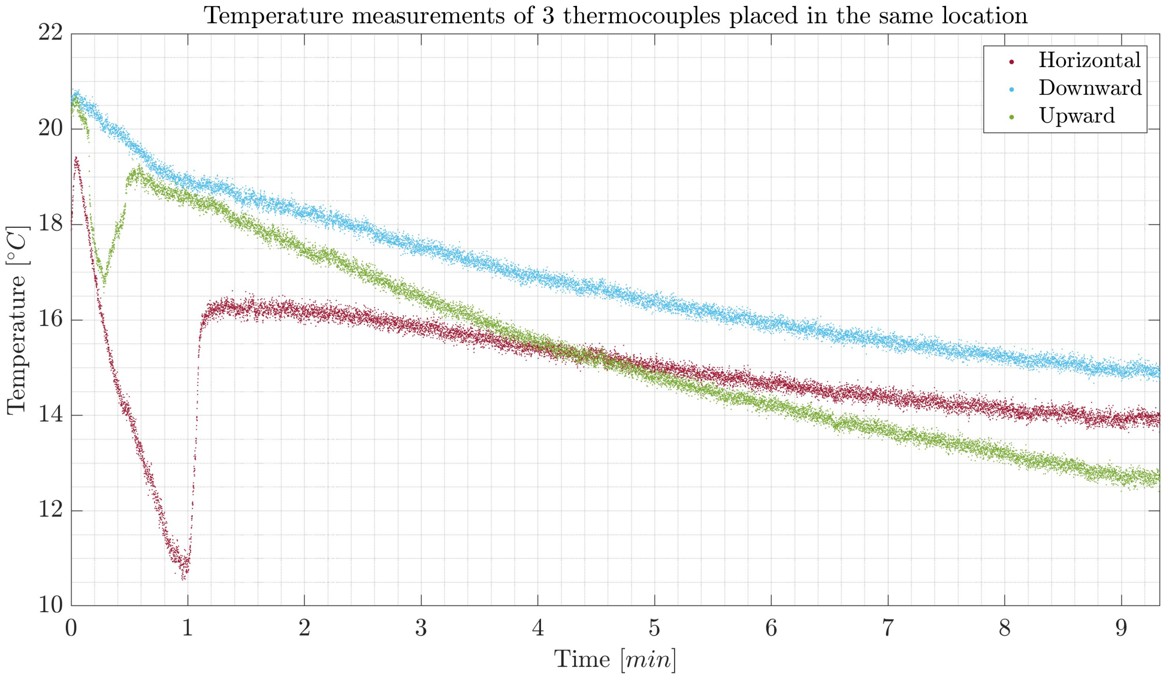

Figure B.7: Temperature of the water vapour flow exiting a 245 mm long channel with constant cross-section area, measured with 3 T-type thermocouples. The tip of the thermocouples has been bent in different directions: horizontal (red), thus perpendicular to the direction of the flow, as normally placed for a regular experiment; upwards (green), in the direction of the flow; downwards (cyan), opposite to the flow.

a slight variation in the direction of the tip. These phenomena remain partially unexplained. Possible contributing factors to these irregularities include condensation on the thermocouple tips and turbulence resulting from abrupt fluctuations in local flow conditions. If we neglect these occasional variations, we observe temperatures within a range of 2°C. This is likely attributable to the different average distances of the thermocouple tips from the 20°C wall. As previously shown in section B.1, a thermocouple situated closer to a surface measures a temperature that closely resembles the surface temperature in comparison to probes situated further away. In this context, the thermocouple tip pointing downward (cyan) was almost entirely enclosed by the channel, while the one pointing upward (green) was partially exposed outside the channel. The horizontally positioned thermocouple (red) represents an intermediate case between the previous two.

To test this hypothesis, we conducted the following analysis. The thermocouple tip exposed to the flow is assumed to be in thermal equilibrium with its surrounding environment. Therefore, the total contribution of convective and radiative heat transfer should be equal to zero. We use Equation B.3 to find the real value of the flow temperature (T_{flow}), knowing the temperature measured by the thermocouples (T_{TC}) and assuming different values for the wall temperature (T_{wall}). The product between view factor and surface area of the channel ($F_{a\to t}\ A_{wall}$) is approximately equal to the surface area of the thermocouple tip (A_{TC}), in the order of $10^{-5}\ m^2$. The emissivity (ε) was assumed equal to 0.95.

$$F_{a\to t}\ A_{wall}\ \varepsilon\sigma(T_{TC}^4 - T_{wall}^4) + A_{TC}\ h_{conv}(T_{TC} - T_{flow}) = 0 \tag{B.3}$$

The outcomes, expressed as $\Delta T_{real} = T_{flow} - T_{TC}$, are reported in Figure B.8 for the warm, with T_{wall} between 15 and 20°C, and in Figure B.9 for the frozen model, with T_{wall} between -5 and 0°C. A thermocouple placed at the vent of the warm model is affected by a wall temperature likely between 17.5 and 20°C. The resulting temperature measurement underestimates the real flow temperature by a maximum of 1°C. In the frozen model, where the vent temperature is likely close to 0°C, the flow temperature is estimated to be 1-1.5°C lower than the measured value.

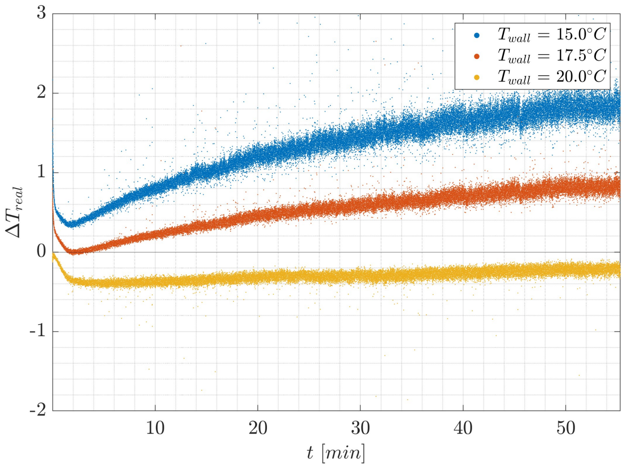

Figure B.8: Flow-measured temperature difference ($\Delta T_{real} = T_{flow} - T_{TC}$) estimated for a thermocouple placed at the vent of the *warm model*. Positive values indicate thermocouple readings underestimating the flow temperature. The most conservative result is given by a vent temperature $T_{wall} = 15°C$. Image created in *MATLAB*.

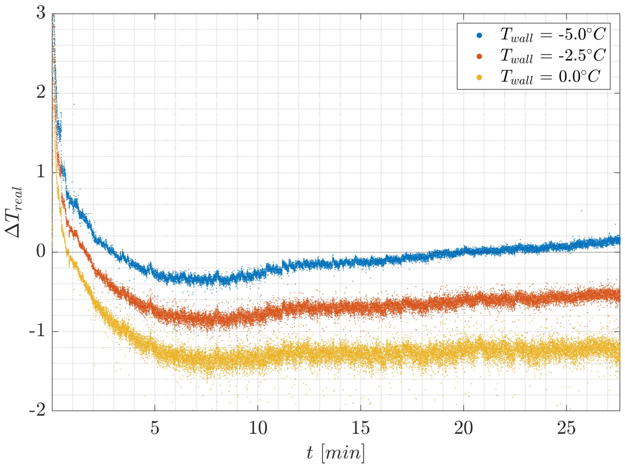

Figure B.9: Flow-measured temperature difference ($\Delta T_{real} = T_{flow} - T_{TC}$) estimated for a thermocouple placed at the vent of the *frozen model*. Negative values indicate thermocouple readings overestimating the flow temperature. The most conservative result is given by a vent temperature $T_{wall} = 0°C$. Image created in *MATLAB*.

In summary, these observations strongly suggest that the thermocouple readings closely approximate the flow temperature, with a deviation from the actual flow temperature within $2°C$. This value is considered as the uncertainty of flow temperature measurements.

B.4 Temperature Profiles

Figure B.10 shows the flow temperature evolution inside the warm model, described in Journal Article: Section 2. Over time, the water temperature decreases due to the cooling effect of the evaporation process, without any external heating power being applied to the reservoir. Interestingly, the flow temperature exhibits an increase towards the vent, aligning with observations made by Sklavenitis (2022) and Verhoeff (2023).

Furthermore, we observe a large temperature range at the end of the experiment, after the end of re-pressurisation and thermal adaptation of thermocouple tips to the ambient temperature. As outlined in section B.1, we consider the temperatures measured within the channel under static conditions (without gas flow) to be roughly equivalent to the model temperature. Consequently, we infer that the model underwent a heat exchange during the experiment. This inference is further supported by empirical observations: when touched, the model feels colder at the base compared to the top.

The frozen model generates different temperature profiles, as shown in Figure B.11. In this instance, the flow temperature decreases towards the vent. This is mainly attributed to convection and thermal radiation processes and, therefore, to the lower wall temperature, as explained in Journal Article: Section 3. Since model temperature measurements before and after the evacuation/re-pressurisation cycle stay almost unchanged, we can conclude that the model temperature stays constant throughout the experiment, given the larger total heat capacity of the model.

B.5 Recovery Factor

In this section, we present estimates of the recovery factor (R_f), showing that heat addition is non-negligible and, therefore, that the flow is not isentropic.

The gas flow temperature in correspondence with a thermally insulated surface, defined as adiabatic

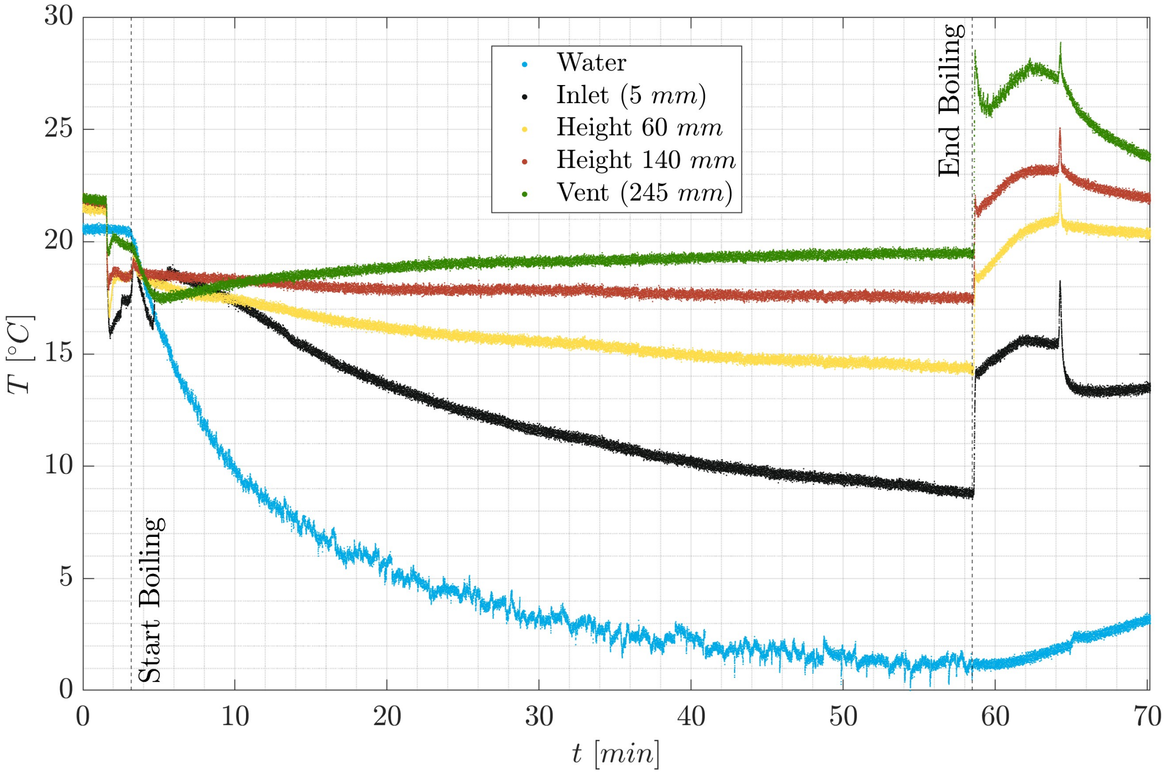

Figure B.10: Temperature readings acquired in the reservoir, at water level, and along the channel at different heights during one *warm model*. The 2 vertical black dashed lines indicate the boiling starting and ending points. Image created in *MATLAB*.

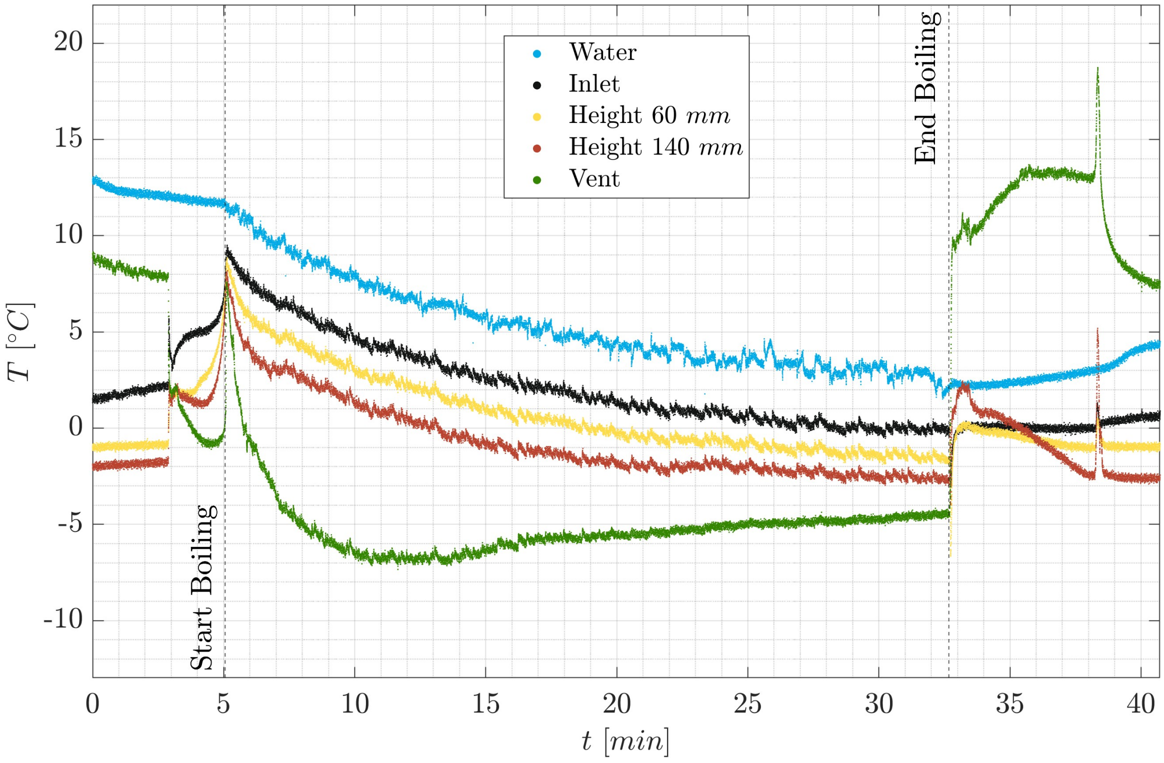

Figure B.11: Temperature readings acquired in the reservoir, at water level, and along the channel at different heights during one *frozen model* experiment. The 2 vertical black dashed lines indicate the boiling starting and ending points. Image created in *MATLAB*.

wall temperature, is observed to be higher than the mean-stream static temperature due to viscous dissipation. This effect is quantified by the temperature recovery factor (R_f), proportional to the percentage of kinetic energy converted into temperature (Welch et al., 1950; Tucker et al., 1951; Hong et al., 2023). We anticipate this effect in our experiment, with interactions between water vapour flow and channel walls decelerating the flow. This results in a higher temperature measurement known as the recovery temperature (T_r), which is related to the expected bulk temperature in the absence of viscous effects (T_b), as defined in Equation B.4 and Equation B.5.

$$T_r = T_b + R_f \frac{V^2}{2c_p} \tag{B.4}$$

$$T_r = T_b \left(1 + R_f \frac{\gamma - 1}{2} M^2\right) \tag{B.5}$$

A first estimate of the recovery factor is derived from a comparison of isentropic Mach number calculated from pressure and temperature measurements using Equation 3.11 and Equation 3.14. Reservoir pressure and temperature are used instead of total pressure and total temperature at the vent, since the latter is difficult to obtain experimentally. Equation B.5 and the Mach number solutions found with Equation 3.14 from pressure measurements are substituted into Equation 3.11:

$$M = \sqrt{\frac{2}{\gamma - 1}\left(\frac{T_{res}\left(1 + R_f \frac{\gamma-1}{2} M^2\right)}{T_r} - 1\right)}$$

$$R_f = \left(1 + \frac{\gamma - 1}{2} M^2 - \frac{T_{res}}{T_r}\right)\left(\frac{T_{res}}{T_r}\frac{\gamma - 1}{2} M^2\right)^{-1}$$

The results are reported in Figure B.12. Given that R_f falls within the range of 0 to 1, recovery factors exceeding 1, as observed in the warm model, suggest that the temperature rise cannot be solely attributed to viscous effects. There must be additional processes contributing to the heating of the flow that need to be taken into consideration. In this research, we accounted for convective, radiative heat transfer and phase change.

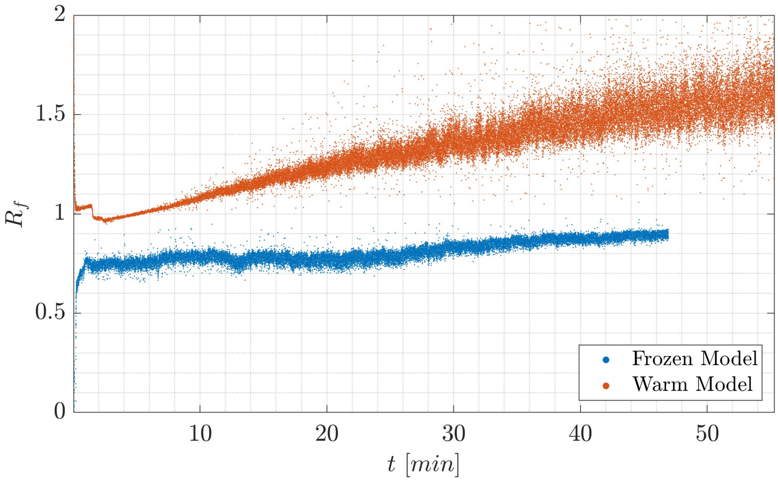

Figure B.12: Recovery factor of the one warm and one frozen model experiment, obtained by comparison of isentropic Mach numbers computed from temperature and pressure measurements. Image created in *MATLAB*.

B.6 Evidence of Wall Accretion

Accretion of water vapour molecules on the surface of the channel walls is observed in the frozen model. Given their low temperature and large heat capacity, the model walls can absorb heat released in the phase change from gas to solid. Ice clusters forming near the vent have been observed during most of the frozen model experiments, as displayed by Figure B.13.

This phenomenon occurred more frequently when the metal tube of the Pitot tube was positioned inside the channel, implying that this 1.8-*mm* diameter tube might have restricted the flow, increasing flow saturation and inducing higher nucleation rates in that channel section. As water vapour started to condense on the surface of the metal tube, the cross-sectional area at the vent further decreased, causing a chain reaction that led to channel blockage within the first 10 minutes of the experiments.

This issue was partially addressed by adjusting the position of the Pitot tube a few millimetres higher, aligning it with the channel's vent. With this modification, the flow was less affected by the presence of the tube, allowing for the successful acquisition of total pressure measurements.

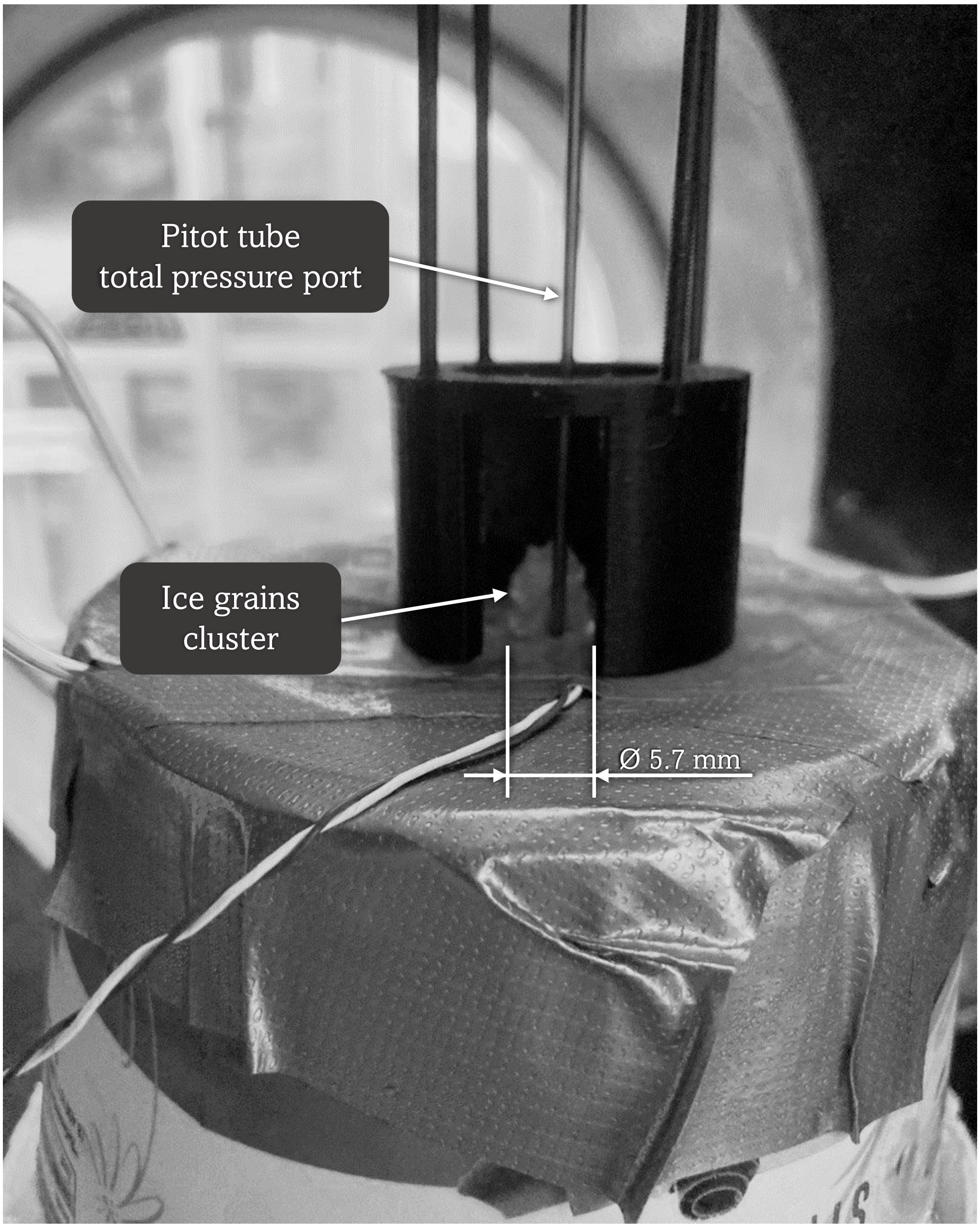

Figure B.13: Picture of the frozen model, showing an ice grain cluster clogging the vent of the channel. The metal tube has a diameter of 1.8-*mm* and probes the total flow pressure. The tube is supported by a structure, depicted in Figure A.7, placed on top of the lead covering the ice around the channel. The lead is taped in order to prevent sublimated water vapour from compromising the measurements.

C

Additional Analysis with Numerical Simulation

The numerical model presented in the work of Hijden (submitted), also involving the author of this study, has yielded valuable insights into the plume characteristics. While the model has been designed for simulating plume dynamics in larger-scale crevasses, with dimensions of 150 m in length and 6-9 m in width, further refinement is essential to adapt it for use in smaller-scale plumes similar to the laboratory model employed in this study. Nonetheless, this model already indicates how the channel geometry evolves and configurations that are likely and, therefore, that are better to test in the laboratory.

The alteration of the channel's geometry is influenced by two primary processes: sublimation of ice from the walls and accretion of gas from the flow onto the crevasse walls. It is observed that accretion onto the walls significantly outweighs sublimation from the walls with crevasse temperatures assumed between 200 and 273 K (see Equation 3.5). This dominance of accretion implies a reduction in the channel's cross-sectional area over time.

The simulation started from a generic crevasse profile used throughout the study of Hijden (submitted). The channel's geometry evolves due to accretion, leading to changes in the flow characteristics. To account for these variations, time steps of one hour were defined to update the channel's geometry based on accretion. The MacCormack method was utilized to determine the flow solutions after each time step (Anderson, 2003). These flow solutions, in turn, were used to calculate accretion and sublimation values, updating the geometry for the subsequent time step. This iterative process continued until negligible alterations in the channel's geometry were observed.

The total mass flux into the walls, denoted as E and expressed in units of kg/m^2s, is directly related to the change in channel radius r with Equation C.1. This equation converts the mass arriving on the walls (kg) into volume of water particles (m^3). The constant values N_A and M_{H_2O} correspond to the Avogadro number and the molar mass of water respectively. The volume of a water molecule (V_{H_2O}) is computed assuming a diameter of approximately 2.75Å.

$$\frac{\partial r}{\partial t} = E\frac{N_A}{M_{H_2O}}V_{H_2O} \tag{C.1}$$

In the work by Hijden (submitted), we simulated the evolution of a non-circular crack, while in this study, a circular crack is considered. The evolution of the geometry is depicted in Figure C.1. After 30 hours, there was a significant reduction in the throat diameter, decreasing to almost half of its original width, while the exit diameter only decreased by a few tens of centimeters. The convergent portion of the channel experienced the most substantial reduction in cross-sectional area, ultimately tending towards a straight channel configuration. In contrast, the divergent section rapidly flared after the throat, and the throat location shifted towards lower x-values. The change in radius decreased with time, as the mass flow rate also decreased given the smaller cross-section area.

It's important to acknowledge that in this numerical model, we assume a steady-state flow where no external forces influence the plume. However, in the real environment of Enceladus, the icy crust experiences continuous tidal stress, resulting in the opening and closing of cracks (Kite et al., 2016). These effects appear to be related to the moon's orbital period, which is approximately 32-33 hours

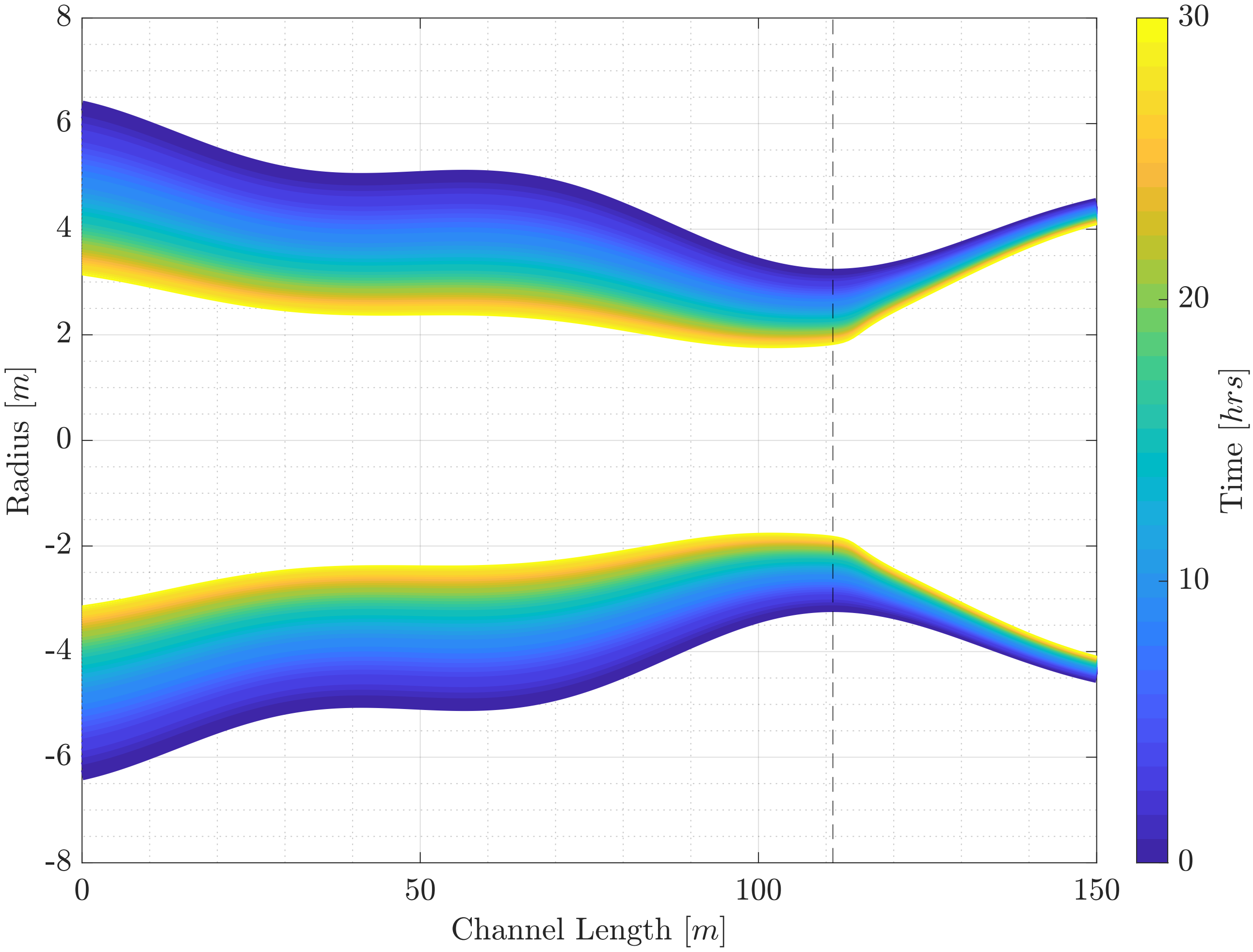

Figure C.1: Geometry evolution of a channel profile with time. The different lines show how the baseline channel geometry evolves due to accretion, with each line's colour indicating the duration since accretion initiation. The channel has a length of 150 m, an initial throat diameter of 6.3 m and initial exit diameter of 9 m. After 30 hours, the throat diameter decreased to 3.65 m, and the exit diameter reduced to 8.2 m. Additionally, the throat location, indicated with a black dashed line, shifted towards lower channel lengths. Image created in *MATLAB*.

(Ingersoll et al., 2020). As a result, longer simulations may lead to inaccurate results due to the influence of these periodic forces.

It should be noted that this numerical model assumes steady-state flow and, therefore, no external forces affecting the plume. In reality, the icy crust of Enceladus constantly undergoes tidal stress, opening and closing the cracks (Kite et al., 2016). These effects are seen to be correlated to the period of Enceladus (Ingersoll et al., 2020), around 32-33 hours. Therefore, longer simulation times could be less insightful.

Based on these observations, our analysis suggests that a configuration similar to a straight channel is a plausible feature in the lower part of the crevasse, specifically before reaching the throat region. On the other hand, near the surface, it becomes more likely to have larger diameters. This discovery aligns with the conclusions presented in Journal Article: Section 5.3, which indicate that achieving flow temperatures below ∼210 K at the vent would necessitate a divergent channel section.

D

Technical Drawings

The technical drawings are reported in the following pages. The first one is the channel realized for this research and 3D printed in polylactic acid (PLA). The second drawing represents the reservoir, made out of plexiglass and realized by Sklavenitis (2022).

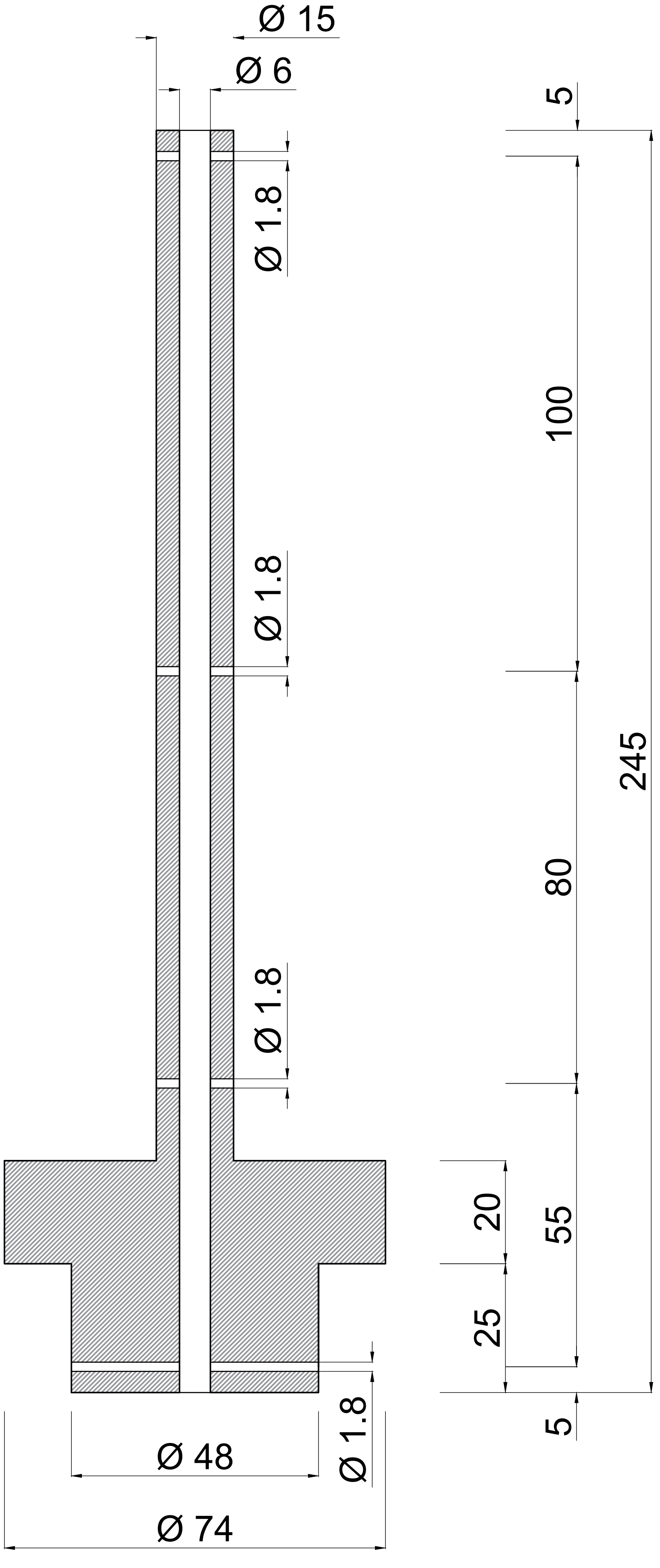
Ø 15
Ø 6
Ø 1.8
Ø 1.8
Ø 1.8
Ø 1.8
Ø 48
Ø 74
5
100
245
80
55
20
25
5

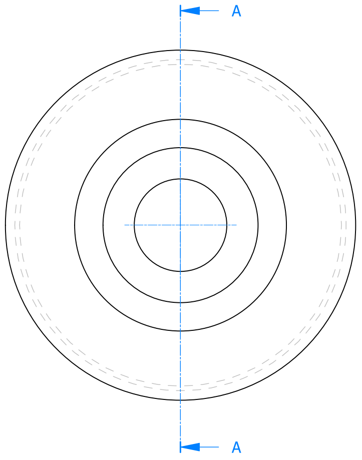

A-A

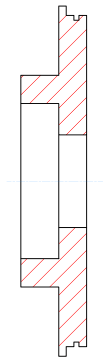

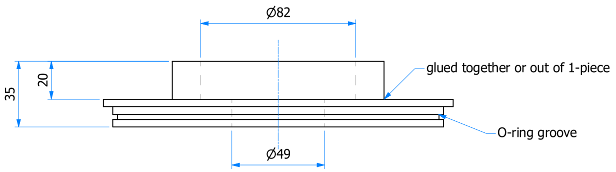

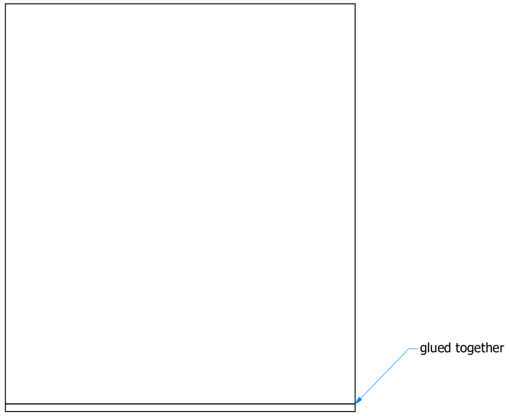

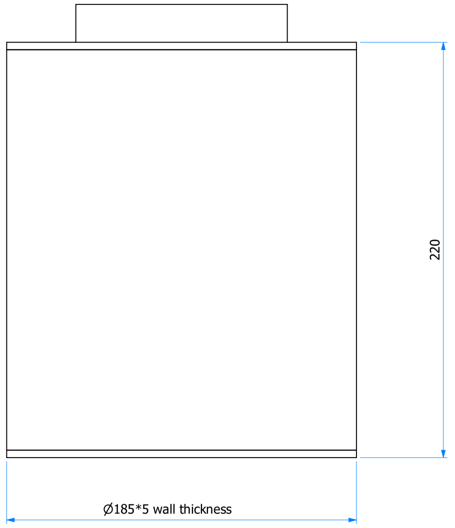

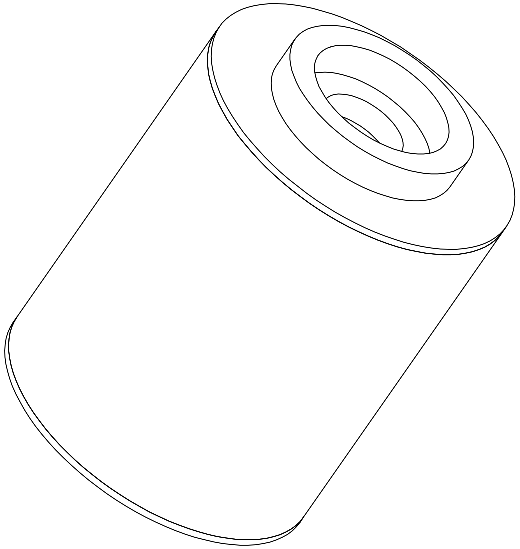

Getekend bbakker
Controle
Datum 12-10-2021
Status Concept
Materiaal
Aantal

Benaming

Project

Eenheid
mm

Schaal

Tekening nummer
complete assy

Blad nr.
1 / 1

TUDelft DEMO
www.demo.tudelft.nl

Ra
Alle vlakken tenzij anders vermeld

Toleranties volgens NEN-EN-ISO 1101:2013 en NEN-ISO 2768-mH
Ruwheden volgens NEN-EN-ISO 1302:2002

Formaat
A2

Bibliography

Anderson, J. D. (2003). *Modern compressible flow.*

Antoine, C. (1888). "Tensions des vapeurs: nouvelle relation entre les tensions et les temperatures". In: *Comptes Rendus des Séances de l'Académie des Sciences.*

Becx, T. (2019). "Icy moon plume simulator chamber: The design of a laboratory recreation of an icy moon plume". In: URL: `http://resolver.tudelft.nl/uuid:f1742769-f281-4de6-acd6-23a3c73694a5`.

Beuthe, M., A. Rivoldini, and A. Trinh (2016). "Enceladus's and Dione's floating ice shells supported by minimum stress isostasy". In: *Geophysical Research Letters* 43.19, pp. 10–088. DOI: `https://doi.org/10.1002/2016GL070650`.

Bridgeman, O. C. and E. W. Aldrich (May 1964). "Vapor Pressure Tables for Water". In: *Journal of Heat Transfer* 86 (2), pp. 279–286. ISSN: 0022-1481. DOI: `https://doi.org/10.1115/1.3687121`.

Choblet, G., G. Tobie, C. Sotin, M. Běhounková, O. Čadek, F. Postberg, and O. Souček (2017). "Powering prolonged hydrothermal activity inside Enceladus". In: *Nature Astronomy* 1.12, pp. 841–847. DOI: `https://doi.org/10.1038/s41550-017-0289-8`.

David, K., J. Gorham, S. Kim, P. Miller, and C. Minkus (2006). "Aeronautical wind tunnels, europe and asia". In: Library of Congress Washington DC Federal Research DIV.

Dong, Y., T. W. Hill, B. D. Teolis, B. A. Magee, and J. H. Waite (2011). "The water vapor plumes of Enceladus". In: *Journal of Geophysical Research: Space Physics* 116.A10. DOI: `https://doi.org/10.1029/2011ja016693`.

Feistel, R. and W. Wagner (Jan. 2007). "Sublimation pressure and sublimation enthalpy of H2O ice Ih between 0 and 273.16K". In: *Geochimica et Cosmochimica Acta* 71.1, pp. 36–45. DOI: `https://doi.org/10.1016/j.gca.2006.08.034`.

Fu, M., H. Gu, J. Cui, Z. Xiao, F. He, Y. Wei, and Z. Ren (2021). "On the structure of the Enceladus plume". In: *Monthly Notices of the Royal Astronomical Society* 504.4, pp. 6216–6222. DOI: `https://doi.org/10.1093/mnras/stab1265`.

Gao, P., P. Kopparla, X. Zhang, and A. P. Ingersoll (Jan. 2016). "Aggregate particles in the plumes of Enceladus". In: *Icarus* 264, pp. 227–238. DOI: `https://doi.org/10.1016/j.icarus.2015.09.030`.

Hansen, C. J., L. Esposito, A. I. F. Stewart, J. Colwell, A. Hendrix, W. Pryor, D. Shemansky, and R. West (2006). "Enceladus' water vapor plume". In: *Science* 311.5766, pp. 1422–1425. DOI: `https://doi.org/10.1126/science.1121254`.

Hansen, C. J., L. W. Esposito, K-M. Aye, J. E. Colwell, A. R. Hendrix, G. Portyankina, and D. Shemansky (2017). "Investigation of diurnal variability of water vapor in Enceladus' plume by the Cassini ultraviolet imaging spectrograph". In: *Geophysical Research Letters* 44.2, pp. 672–677. DOI: `https://doi.org/10.1002/2016gl071853`.

Hansen, C. J., L. W. Esposito, J. E. Colwell, A. R. Hendrix, G. Portyankina, A. I. F. Stewart, and R. A. West (2020). "The composition and structure of Enceladus' plume from the complete set of Cassini UVIS occultation observations". In: *Icarus* 344, p. 113461. DOI: `https://doi.org/10.1016/j.icarus.2019.113461`.

Hansen, C. J., L. W. Esposito, A. I. F. Stewart, B. Meinke, B. Wallis, J. E. Colwell, A. R. Hendrix, K. Larsen, W. Pryor, and F. Tian (2008). "Water vapour jets inside the plume of gas leaving Enceladus". In: *Nature* 456.7221, pp. 477–479. DOI: `https://doi.org/10.1038/nature07542`.

Hansen, C. J., D. E. Shemansky, L. W. Esposito, A. I. F. Stewart, B. R. Lewis, J. E. Colwell, A. R. Hendrix, R. A. West, J. H. Waite Jr, B. Teolis, et al. (2011). "The composition and structure of the Enceladus plume". In: *Geophysical Research Letters* 38.11. DOI: `https://doi.org/10.1029/2011gl047415`.

Hong, C., H. Katanoda, Y. Asako, and M. Faghri (Mar. 2023). "Temperature recovery factor for gaseous nitrogen flow in a microtube". In: *International Journal of Heat and Mass Transfer* 202, p. 123688. ISSN: 00179310. DOI: `https://doi.org/10.1016/j.ijheatmasstransfer.2022.123688`.

Howett, C. J. A., J. R. Spencer, J. Pearl, and M. Segura (2011). "High heat flow from Enceladus' south polar region measured using 10–600 cm- 1 Cassini/CIRS data". In: *Journal of Geophysical Research: Planets* 116.E3. DOI: `https://doi.org/10.1029/2010je003718`.

Ingersoll, A. P. and S. P. Ewald (2011). "Total particulate mass in Enceladus plumes and mass of Saturn's E ring inferred from Cassini ISS images". In: *Icarus* 216.2, pp. 492–506. DOI: `https://doi.org/10.1016/j.icarus.2011.09.018`.

Ingersoll, A. P., S. P. Ewald, and S. K. Trumbo (July 2020). "Time variability of the Enceladus plumes: Orbital periods, decadal periods, and aperiodic change". In: *Icarus* 344, p. 113345. DOI: `https://doi.org/10.1016/j.icarus.2019.06.006`.

Ingersoll, A. P. and M. Nakajima (July 2016b). "Controlled boiling on Enceladus. 2. Model of the liquid-filled cracks". In: *Icarus* 272, pp. 319–326. DOI: `https://doi.org/10.1016/j.icarus.2015.12.040`.

Khawaja, N., F. Postberg, J. Hillier, F. Klenner, S. Kempf, L. N"olle, R. Reviol, Z. Zou, and R. Srama (2019). "Low-mass nitrogen-, oxygen-bearing, and aromatic compounds in Enceladean ice grains". In: *Monthly Notices of the Royal Astronomical Society* 489.4, pp. 5231–5243. DOI: `https://doi.org/10.1093/mnras/stz2280`.

Kieffer, S. W., X. Lu, C. M. Bethke, J. R. Spencer, S. Marshak, and A. Navrotsky (Dec. 2006). "A Clathrate Reservoir Hypothesis for Enceladus' South Polar Plume". In: *Science* 314.5806, pp. 1764–1766. DOI: `https://doi.org/10.1126/science.1133519`.

Kikoin, A. K. and I. K. Kikoin (1978). *Molecular physics*. Mir.

Kite, E. S. and Allan M. Rubin (2016). "Sustained eruptions on Enceladus explained by turbulent dissipation in tiger stripes". In: *Proceedings of the National Academy of Sciences* 113.15, pp. 3972–3975. DOI: `https://doi.org/10.1073/pnas.1520507113`.

Kosky, P., R. Balmer, W. Keat, and G. Wise (2013). "Mechanical Engineering". In: *Exploring Engineering*. Elsevier, pp. 259–281. DOI: `https://doi.org/10.1016/b978-0-12-415891-7.00012-1`.

Krupp, N., E. Roussos, C. Paranicas, D. G. Mitchell, P. Kollmann, S. Ye, W. S. Kurth, K. K. Khurana, R. Perryman, H. Waite, et al. (2018). "Energetic electron measurements near Enceladus by Cassini during 2005–2015". In: *Icarus* 306, pp. 256–274. DOI: `https://doi.org/10.1016/j.icarus.2017.10.022`.

Matveev, A. N. (1985). "Molecular physics". In: *Vysshaya Shkola, Moscow (198k)*.

Minissale, M., Y. Aikawa, E. Bergin, M. Bertin, W. A. Brown, S. Cazaux, S. B. Charnley, A. Coutens, H. M. Cuppen, V. Guzman, et al. (2022). "Thermal desorption of interstellar ices. A review on the controlling parameters and their implications from snowlines to chemical complexity". In: *arXiv preprint arXiv:2201.07512*. DOI: `https://arxiv.org/abs/2201.07512`.

Morgan, R. V., R. S. Reid, A. M. Baker, B. Lucero, and J. D. Bernardin (2017). *Emissivity Measurements of Additively Manufactured Materials*. Tech. rep. DOI: `https://doi.org/10.2172/1341825`.

Nakajima, M. and A. P. Ingersoll (July 2016a). "Controlled boiling on Enceladus. 1. Model of the vapor-driven jets". In: *Icarus* 272, pp. 309–318. DOI: `https://doi.org/10.1016/j.icarus.2016.02.027`.

Newman, S. F., B. J. Buratti, R. H. Brown, R. Jaumann, J. Bauer, and T. Momary (2008). "Photometric and spectral analysis of the distribution of crystalline and amorphous ices on Enceladus as seen by Cassini". In: *Icarus* 193.2, pp. 397–406. DOI: https://doi.org/10.1016/j.icarus.2007.04.019.

Pellicer, J., V. García-Morales, L. Guanter, M. J. Hern'andez, and M. Dolz (July 2002). "On the experimental values of the water surface tension used in some textbooks". In: *American Journal of Physics* 70.7, pp. 705–709. DOI: https://doi.org/10.1119/1.1477431.

Porco, C., D. DiNino, and F. Nimmo (2014). "How the geysers, tidal stresses, and thermal emission across the south polar terrain of Enceladus are related". In: *The Astronomical Journal* 148.3, p. 45. DOI: https://doi.org/10.1088/0004-6256/148/3/45.

Porco, C., P. Helfenstein, P. C. Thomas, A. P. Ingersoll, J. Wisdom, R. West, G. Neukum, T. Denk, R. Wagner, T. Roatsch, et al. (2006). "Cassini observes the active south pole of Enceladus". In: *Science* 311.5766, pp. 1393–1401. DOI: https://doi.org/10.1126/science.1123013.

Portyankina, G., L. W. Esposito, K-M. Aye, C. J. Hansen, and A. Ali (2022). "Modeling the complete set of Cassini's UVIS occultation observations of Enceladus' plume". In: *Icarus* 383, p. 114918. DOI: https://doi.org/10.1016/j.icarus.2022.114918.

Postberg, F., S. Kempf, J. Schmidt, N. Brilliantov, A. Beinsen, B. Abel, U. Buck, and R. Srama (2009). "Sodium salts in E-ring ice grains from an ocean below the surface of Enceladus". In: *Nature* 459.7250, pp. 1098–1101. DOI: https://doi.org/10.1038/nature08046.

Postberg, F., N. Khawaja, B. Abel, G. Choblet, C. R. Glein, M. S. Gudipati, B. L. Henderson, H.-W. Hsu, S. Kempf, F. Klenner, G. Moragas-Klostermeyer, B. Magee, L. N"olle, M. Perry, R. Reviol, J. Schmidt, R. Srama, F. Stolz, G. Tobie, M. Trieloff, and J. H. Waite (2018). "Macromolecular organic compounds from the depths of Enceladus". In: *Nature* 558.7711, pp. 564–568. DOI: https://doi.org/10.1038/s41586-018-0246-4.

Postberg, F., J. Schmidt, J. Hillier, S. Kempf, and R. Srama (2011). "A salt-water reservoir as the source of a compositionally stratified plume on Enceladus". In: *Nature* 474.7353, pp. 620–622. DOI: https://doi.org/10.1038/nature10175.

Roberts, J. H. and F. Nimmo (2008). "Tidal heating and the long-term stability of a subsurface ocean on Enceladus". In: *Icarus* 194.2, pp. 675–689. DOI: https://doi.org/10.1016/j.icarus.2007.11.010.

Robidel, R., S. Le Mouëlic, G. Tobie, M. Massé, B. Seignovert, C. Sotin, and S. Rodriguez (2020). "Photometrically-corrected global infrared mosaics of Enceladus: New implications for its spectral diversity and geological activity". In: *Icarus* 349, p. 113848. DOI: https://doi.org/10.1016/j.icarus.2020.113848.

Rühl, A., S. Kolling, V. Mende, and B. Kiesewetter (2016). "Computational design of a heated PMMA window validated by infrared thermography". In: *Glass Structures & Engineering* 1.2, pp. 375–383. DOI: https://doi.org/10.1007/s40940-016-0004-7.

Saidi, M. and R.H. Abardeh (2010). "Air pressure dependence of natural-convection heat transfer". In: *Proceedings of the world congress on engineering*. Vol. 2. 1. WCE 2010 London, UK, pp. 1–5. URL: https://www.iaeng.org/publication/WCE2010/WCE2010_pp1444-1447.pdf.

Schmidt, J., N. Brilliantov, F. Spahn, and S. Kempf (Feb. 2008). "Slow dust in Enceladus' plume from condensation and wall collisions in tiger stripe fractures". In: *Nature* 451.7179, pp. 685–688. DOI: https://doi.org/10.1038/nature06491.

Sklavenitis, S. (2022). "Experimental simulation and assessment of the geysers of icy moons in the laboratory". In: URL: http://resolver.tudelft.nl/uuid:3af2e6ad-4dc2-4acc-9cbf-a9afc15cebd9.

Smith, H. T., R. E. Johnson, M. E. Perry, D. G. Mitchell, R. L. McNutt, and D. T. Young (2010). "Enceladus plume variability and the neutral gas densities in Saturn's magnetosphere". In: *Journal of Geophysical Research: Space Physics* 115.A10. DOI: https://doi.org/10.1029/2009ja015184.

Spencer, J. R., A. C. Barr, L. W. Esposito, P. Helfenstein, A. P. Ingersoll, R. Jaumann, C. P. McKay, F. Nimmo, and J. H. Waite (2009). "Enceladus: An active cryovolcanic satellite". In: *Saturn from Cassini-Huygens*, pp. 683–724. DOI: https://doi.org/10.1007/978-1-4020-9217-6_21.

Spencer, J. R. and F. Nimmo (2013). “Enceladus: An active ice world in the Saturn system”. In: *Annual Review of Earth and Planetary Sciences* 41, pp. 693–717. DOI: https://doi.org/10.1146/annurev-earth-050212-124025.

Spencer, J. R., J. C. Pearl, M. Segura, F. M. Flasar, A. Mamoutkine, P. Romani, B. J. Buratti, A. R. Hendrix, L. J. Spilker, and R. M. C. Lopes (2006). “Cassini encounters Enceladus: Background and the discovery of a south polar hot spot”. In: *Science* 311.5766, pp. 1401–1405. DOI: https://doi.org/10.1126/science.1121661.

Spitale, J. N., T. A. Hurford, A. R. Rhoden, E. E. Berkson, and S. S. Platts (2015). “Curtain eruptions from Enceladus’ south-polar terrain”. In: *Nature* 521.7550, pp. 57–60. DOI: https://doi.org/10.1038/nature14368.

Tenishev, V., D.C.S. ”Ozt”urk, M.R. Combi, M. Rubin, J.H. Waite, and M. Perry (2014). “Effect of the Tiger Stripes on the water vapor distribution in Enceladus’ exosphere”. In: *Journal of Geophysical Research: Planets* 119.12, pp. 2658–2667. DOI: https://doi.org/10.1002/2014JE004700.

Teolis, B. D., M. E. Perry, C. J. Hansen, J. H. Waite, C. C. Porco, J. R. Spencer, and C. J. A. Howett (Sept. 2017). “Enceladus Plume Structure and Time Variability: Comparison of Cassini Observations”. In: *Astrobiology* 17.9, pp. 926–940. DOI: https://doi.org/10.1089/ast.2017.1647.

Tian, F., A. I. F. Stewart, O. B. Toon, K. W. Larsen, and L. W. Esposito (2007). “Monte Carlo simulations of the water vapor plumes on Enceladus”. In: *Icarus* 188.1, pp. 154–161. DOI: https://doi.org/10.1016/j.icarus.2006.11.010.

Tucker, M. and S. H. Maslen (1951). *Turbulent boundary-layer temperature recovery factors in two-dimensional supersonic flow.* Vol. 2296. National Advisory Committee for Aeronautics.

Verbiscer, A., R. French, M. Showalter, and P. Helfenstein (2007). “Enceladus: Cosmic graffiti artist caught in the act”. In: *Science* 315.5813, pp. 815–815. DOI: https://doi.org/10.1126/science.1134681.

Verhoeff, T. (2023). “Laboratory experiments recreating icy moons’ geysers”. In: URL: http://resolver.tudelft.nl/uuid:e4e45447-46b3-4892-983e-3757d3841769.

Waite, J. H., M. R. Combi, W. Ip, T. E. Cravens, R. L. McNutt Jr, W. Kasprzak, R. Yelle, J. Luhmann, H. Niemann, D. Gell, et al. (2006). “Cassini ion and neutral mass spectrometer: Enceladus plume composition and structure”. In: *Science* 311.5766, pp. 1419–1422. DOI: https://doi.org/10.1126/science.1121290.

Welch, R. V. and J. E. Volonte (1950). “Experimental investigation of recovery factors and friction factors for air flowing in a tube at supersonic velocities”. PhD thesis. Massachusetts Institute of Technology.

Wijnen, B., P. Sanders, and J.M. Pearce (2018). “Improved model and experimental validation of deformation in fused filament fabrication of polylactic acid”. In: *Progress in Additive Manufacturing* 3.4, pp. 193–203. DOI: https://doi.org/10.1007/s40964-018-0052-4.

Wölk, J., R. Strey, C. H. Heath, and B. E. Wyslouzil (Sept. 2002). “Empirical function for homogeneous water nucleation rates”. In: *The Journal of Chemical Physics* 117.10, pp. 4954–4960. DOI: https://doi.org/10.1063/1.1498465.

Yeoh, S. K., T. A. Chapman, D. B. Goldstein, P. L. Varghese, and L. M. Trafton (June 2015). “On understanding the physics of the Enceladus south polar plume via numerical simulation”. In: *Icarus* 253, pp. 205–222. DOI: https://doi.org/10.1016/j.icarus.2015.02.020.

Yeoh, S. K., Z. Li, D. B. Goldstein, P. L. Varghese, D. A. Levin, and L. M. Trafton (2017). “Constraining the Enceladus plume using numerical simulation and Cassini data”. In: *Icarus* 281, pp. 357–378. DOI: https://doi.org/10.1016/j.icarus.2016.08.028.

Yuningsih, N. and Sardjito (2021). “Temperature Dependence on Distance from Heat Source Objects”. In: *2nd International Seminar of Science and Applied Technology (ISSAT 2021)*. Atlantis Press, pp. 238–241. DOI: 10.2991/aer.k.211106.037.